universität wien

DISSERTATION

Titel der Dissertation:

First Principles Investigations of Adsorption on a Transition Metal Surface: Oxygen and Indium on the (110) Surface of Tungsten

angestrebter akademischer Grad
Doktor der Naturwissenschaften (Dr. rer. nat.)

Verfasser:	Markus Stöhr
Matrikel-Nummer:	0548529
Dissertationsgebiet:	A091411
Betreuer:	Ao. Univ.-Prof. Dr. Raimund Podloucky

Wien, am 23. April 2009

Abstract

Adsorption and catalytic properties of metal surfaces are of great scientific and technological interest. For an accurate description of the detailed atomic and electronic structure of surfaces a number of experimental methods exist. On the theoretical side, physical and chemical properties of solid materials, which can be modelled by unit cells of up to a few hundreds of atoms, are accurately described by first-principles density functional theory (DFT) approaches. No empirical parameters are needed for such calculations. Many interesting properties which are observed experimentally, however, require systems with many more atoms, and for that the so-called Cluster Expansion (CE) is ideally suited. In this work, the input for the CE consists of a sufficiently large set of DFT calculations, and by combining CE and DFT the accuracy of DFT calculations can be forwarded to the simulation of large systems. The interaction energies of the CE are exploited for Monte Carlo (MC) simulations, which enable the investigation of the temperature and concentration dependent formation of adsorption structures. The present work makes use of this strategy for studying atomic adsorption on a tungsten surface, with the aim to model and analyse the temperature dependent formation of adsorption structures. The present theoretical study was initiated by the close collaborations with experimental groups within a network project of the Austrian Science Foundation FWF.

Without the need of any empirical parameter, by the combination of DFT, CE and MC techniques the oxygen adsorption on the tungsten *W(110)* surface is studied resulting in a surface phase diagram. Coverages up to 1 monolayer are considered corresponding to the range of oxygen concentrations of $0 \leq x_O \leq 1$. DFT results for single-site adsorption and in particular for full coverage reveal that adsorption at 3-fold hollow H3 sites is by far the most stable one. Therefore, the CE is done for a monoatomic layer with the two geometrically equivalent H3 sublattices of the *W(110)* surface. Based on 60 DFT calculations with lateral unit cells containing up to 12 tungsten atoms for which the atomic geometries are fully relaxed, a determination of the effective interaction energies and a ground state search for 80394 adsorption structures is undertaken. As a result, four ground state structures emerge with the lateral unit cells described as (2×5) for $x_O = 0.20$, (2×2)(a) for $x_O = 0.25$, (2×1) for $x_O = 0.50$, and (2×2)(b) for $x_O = 0.75$. In agreement with experiment, the most stable structures are (2×1) and (2×2)(b), which are formed at larger coverages. At lower coverages, the thermodynamical stability of the corresponding two ground states is rather weak. Detailed analysis of the relaxation of the ground state structures reveals sizeable lateral stresses acting on the surface tungsten atoms. On the basis of the

effective cluster interactions MC simulations are performed in order to derive the critical temperatures for the order-disorder transition by which the phase diagram is finally constructed. Although the agreement to the experimentally derived phase diagram is good, significant differences remain, which might be due to the neglect of vibrational properties in the calculations. Therefore, the influence of vibrations of the adsorbed oxygen atoms on the adsorption energies is studied, namely by calculating selected wagging and stretching vibrations for the ground state structures. The discrepancies, however, could not be fully resolved. The conclusion is, that a much more elaborate scheme for dealing with the vibrational properties might be needed.

Another adsorption system, which is studied in combination with new experiments, is indium on *W(110)*. For this study the atomic structure of various indium adlayers at submonolayer coverages on *W(110)* is investigated by a DFT and molecular dynamics (MD) approach as well as by analysis of low-energy electron diffraction intensities. Single atom studies by DFT reveal that adsorption at the four-fold hollow H4 sites of *W(110)* is most preferable, followed by bonding to H3 and two-fold short bridge sites. At full coverage the preference of the adsorption site changes and the H3 site is now the most stable site followed by H4. Both, theory as well as experiment, reveal that for the (3×1) structure, which corresponds to a coverage of $x_{In} = 0.33$, indium atoms occupy exclusively H4 coordinated sites, while for the (1×4) phase ($x_{In} = 0.75$) and (1×5) phase ($x_{In} = 0.80$) H3 and bridge sites are also occupied. According to the DFT results, the (1×4) structure is the most stable one, closely followed by the (1×5) structure. Additional MD simulations at $x_{In} = 0.33$, 0.75 and 0.80 reveal that the (1×4) structure is indeed the most stable structure of the system. The analysis of DFT studies on free monolayers of indium reveal the significant influence of indium-indium bonding on the formation of these adlayer structures. The low-coverage (3×1) structure is energetically the least favorable one, in agreement with the experimental finding that the (3×1) structure is only metastable and transforms with increasing time or upon annealing into islands of (1×4) patterns. In order to investigate, if the (3×1) structure might be stabilized by contaminants, DFT calculations were also performed for co-adsorbing hydrogen and oxygen with indium on *W(110)*. However, the (3×1) structure always remains metastable only. Furthermore it is found, that phase separated regions of oxygen patches and (1×4) indium islands are stabilized by about 1 eV/atom relative to a mixture of indium and oxygen atoms in the (3×1) structure. This finding is in very good agreement with the experimental observation that the (3×1) to (1×4) transition can be triggered by additional oxygen.

Zusammenfassung

Adsorption und katalytische Eigenschaften von Metalloberflächen sind von großem wissenschaftlichem und technologischem Interesse. Für eine genaue Beschreibung der atomaren und elektronischen Strukturen existiert eine ganze Reihe experimenteller Methoden. Auf der theoretischen Seite werden physikalische und chemische Eigenschaften von Festkörpern, die mit Einheitszellen mit bis zu einigen hundert Atomen modelliert werden können, exakt durch Anwendung von *ab initio*-Methoden wie der Dichtefunktionaltheorie (DFT) beschrieben. Für solche Berechnungen werden keine empirischen Parameter benötigt. Viele interessante Eigenschaften, die experimentell beobachtet werden, erfordern jedoch Systeme mit einer viel größeren Anzahl an Atomen, wofür die sogenannte Cluster Entwicklung (CE) ideal geeignet ist. In der vorliegenden Arbeit besteht der Input für die CE aus einer genügend großen Anzahl an DFT Rechnungen, deren Genauigkeit durch die Kombination mit der CE auf die Simulation von großen Systemen ausgeweitet werden kann. Die Wechselwirkungsenergien der CE werden für Monte Carlo (MC) Simulationen verwendet, die es erlauben die temperatur- und konzentrationsabhängige Bildung von Adsorptionsstrukturen zu untersuchen. Die Arbeit verwendet diesen Ansatz um die atomare Adsorption auf einer Wolframoberfläche zu studieren mit dem Ziel die temperatur- und konzentrationsabhängige Bildung von Adsorptionsstrukturen zu modellieren und im Detail zu analysieren. Die vorliegende Studie wurde durch eine enge Zusammenarbeit mit experimentellen Gruppen innerhalb eines vernetzten Forschungsprojektes des österreichischen Wissenschaftsfonds (FWF) durchgeführt.

Ohne die Verwendung von empirischen Parametern, durch die Kombination von DFT, CE und MC Methoden, wird die Sauerstoffadsorption auf der Wolfram *W(110)* Oberfläche studiert und das zugehörige Phasendiagramm konstruiert. Es werden Bedeckungen bis zu einer Monolage berücksichtigt, was Sauerstoffkonzentrationen von $0 < x_O < 1$ entspricht. DFT Ergebnisse für die Adsorption einzelner Atome, besonders aber auch für eine voll bedeckte Oberfäche zeigen, dass der dreifach koordinierte Muldenadsorptionsplatz (H3) bei weitem der stabilste ist. Daher wird die CE für eine monoatomare Lage der zwei geometrisch äquivalenten H3 Untergitter auf der *W(110)* Oberfläche konstruiert. Basierend auf 60 DFT Rechnungen mit lateralen Einheitszellen, die bis zu 12 Wolframatome enthalten, werden die effektiven Wechselwirkungsenergien bestimmt und eine Grundzustandssuche für 80394 Adsorptionsstrukturen ausgeführt. Als Ergebnis finden sich vier Grundzustände, die mit lateralen Einheitszellen von (2×5) bei $x_O = 0.20$, (2×2)(a) bei $x_O = 0.25$, (2×1) bei $x_O = 0.50$ und (2×2)(b) bei $x_O = 0.75$ beschrieben werden können. In Übereinstimmung mit dem Experiment sind die

(2×1) und die (2×2)(b) Strukturen die stabilsten Strukturen, die bei höheren Bedeckungen gefunden werden können. Bei niedrigen Bedeckungen ist die thermodynamische Stabilität der gefundenen Grundzustände nur sehr schwach. Eine genaue Analyse der Relaxationen der Grundzustandsstrukturen zeigt, dass auf die Oberflächenatome des Wolframsubstrates eine beträchtliche laterale Spannung ausgeübt wird. Unter Verwendung der effektiven Clusterwechselwirkungen werden MC-Simulationen ausgeführt um die kritischen Temperaturen für den Übergang der ungeordneten in die geordneten Phasen zu bestimmen, mit deren Hilfe das Phasendiagramm konstruiert wird. Obwohl die Übereinstimmung mit dem experimentell bestimmten Phasendiagramm gut ist, bleiben signifikante Unterschiede die womöglich auf die Vernachlässigung der Schwingungseigenschaften zurückzuführen sind.
Daher wird in der vorliegenden Arbeit der Einfluss der Schwingungen von adsorbiertem Sauerstoff auf die Adsorptionsenergien studiert, indem ausgewählte Schwingungsmoden normal und lateral zur Oberfläche für die Grundzustandsstrukturen berechnet werden. Die Abweichungen können jedoch nicht vollständig ausgeräumt werden. Als Schlussfolgerung bleibt, dass eine umfangreichere Berücksichtigung der Schwingungseigenschaften notwendig ist.

Ein anderes Adsorbatsystem, das zusammen mit neuen Experimenten untersucht wird, ist Indium auf *W(110)*. Für diese Untersuchung werden die atomaren Strukturen für verschiedene Indiumadsorptionsstrukturen bei submonolagen Bedeckungen auf *W(110)* sowohl durch eine Kombination von DFT und Molekulardynamik (MD) Simulationen als auch durch Analyse von Beugungsintensitäten von niedrig energetischen Elektronen berechnet. Für die Adsorption von einzelnen Atomen zeigen DFT Ergebnisse, dass der 4-fach koordinierte Muldenadsorptionsplatz H4 auf *W(110)* am günstigsten ist, gefolgt von der Bindung an den H3 und dem 2-fach koordinierten Brückenadsorptionsplatz. Bei voller Bedeckung ändert sich die energetische Reihenfolge und der H3 Adsorptionsplatz ist nun der stabilste, gefolgt vom H4. Sowohl Theorie als auch Experiment zeigen, dass für die (3×1) Struktur, die einer Bedeckung von $x_{In} = 0.33$ entspricht, Indiumatome ausschliesslich H4 koordinierte Adsorptionsplätze besetzen, wohingegen für die (1×4) Phase ($x_{In} = 0.75$) und die (1×5) Phase ($x_{In} = 0.80$) H3 und Brückenplätze ebenfalls besetzt werden. In Übereinstimmung mit den DFT Resultaten ist die (1×4) Struktur die stabilste, dicht gefolgt von der (1×5) Struktur. Zusätzliche MD Simulationen mit $x_{In} = 0.33$, 0.75 und 0.80 zeigen, dass die (1×4) Struktur in der Tat die stabilste Struktur des Systems ist. Die Analyse freistehender Monolagen mit Hife von DFT Rechnungen zeigen den wichtigen Einfluss der Indium-Indium Bindungen bei der Bildung dieser Adsorptionsstrukturen. Die (3×1) Adsorptionslage bei niedriger Bedeckung ist die am energetisch

ungünstigsten, in Übereinstimmung mit der experimentellen Beobachtung, dass die (3×1) Struktur nur metastabil ist und mit zunehmender Zeit oder Ausheizen der Probe sich in Inseln mit (1×4) Muster transformiert. Um auch zu untersuchen ob die (3×1) Struktur durch Verunreinigungen stabilisiert werden könnte, wurden DFT Rechnungen durchgeführt, bei denen Wasserstoff oder Sauerstoff zusammen mit Indium auf *W(110)* adsorbiert wurden. Alle Ergebnisse deuten jedoch darauf hin, dass die (3×1) Struktur metastabil bleibt. Weiterhin zeigt sich, dass ein System mit getrennten Phasen von Sauerstoff und (1×4) Indiuminseln mit etwa 1 eV/atom stabilisiert werden, relativ zu einer Mischung aus Indium und Sauerstoff in der (3×1) Struktur. Dieses Ergebnis stimmt überein mit der experimentellen Beobachtung, dass der Übergang von der (3×1) zur (1×4) Struktur durch zusätzlichen Sauerstoff ausgelöst werden kann.

Contents

1 Introduction **1**

2 Theoretical Aspects **3**

2.1 Density Functional Theory 3

2.1.1 Approximation of the Exchange-Correlation Functional . . 7

2.1.2 Implementation of DFT 8

2.1.3 Computational remarks 8

2.2 Formulation of the Cluster Expansion 9

2.2.1 The Principles of the Cluster Expansion 10

2.2.2 Mixed-Space Cluster Expansion 14

2.2.3 Short Range Order Parameters and Correlation Functions 16

2.2.4 Temperature Dependent CE 17

2.3 Cluster Expansion for Surfaces 19

2.3.1 Extension of CE to Surfaces 19

2.3.2 CE for Adsorbates 21

2.4 Ground State Properties of a System 23

2.4.1 Ground State Diagrams 23

2.4.2 Surface Free Energy 26

2.5 Implementation of the CE 29

2.5.1 Determination of the Interaction Energies by Fitting . . . 29

2.5.2 Optimized Figure Selection with Genetic Algorithms . . . 33

2.6 Monte Carlo Simulations 37

3 Pure Elements **39**

3.1 Bulk Properties of Tungsten 39

3.2 Bulk Properties of Indium 41

3.3 Oxygen 43

3.4 Surface Properties of Metals 44

3.4.1 Bond Breaking Model for Surface Energies 44
3.4.2 Structural Details of the Surfaces 47
3.4.3 The Clean *W(110)* Surface 52
3.4.4 Adsorption Sites on *W(110)* 55
4 *W(110)+O* **57**
4.1 Previous Work on the *O/W(110)* System 57
4.2 Adsorption Energies of Oxygen on *W(110)* 58
4.3 Setup of the Cluster Expansion 59
4.4 Cluster Expansion 60
4.5 Figure Analysis 66
4.6 Oxygen-Oxygen Effective Potential 70
4.7 Structural Details of the Ground States 72
4.8 Monte Carlo Simulations and Phase Diagram 79
4.9 Phase Distribution of the Ground State Structures 84
4.10 Surface Phonons 90
5 *W(110)+In* **95**
5.1 Introduction 95
5.2 Experimental Setup & Computational Details 97
5.3 Adsorption Energies of *In* Atoms 98
5.4 Indium Overstructures 99
5.5 Comparison and Stability of Overstructures 108
5.6 Freestanding Monolayers 110
5.7 Molecular Dynamics 111
5.8 Metastability of the (3×1) Structure 113
A Final Figure Set **121**
B List of Calculated Structures **127**
C Real Space Monte Carlo Data **131**
D List of Publications **137**
E Talks and Conference Contributions **139**
F Curriculum Vitae **141**
G Acknowledgments **143**
Bibliography **145**

1

Introduction

The study of adsorption on metal surfaces is of technological as well as scientific interest. Metal surfaces, and in particular transition metal surfaces, are investigated because of their catalytic properties. The most famous example is platinum (Pt). The rumour is that if no catalyst is known for a particular reaction, Pt is a good candidate. The great importance of this field in science was stressed in 2007 when Gerhard Ertl recieved the Nobel Prize in Chemistry for his achievements of understanding molecular mechanisms on surfaces, especially the synthesis of ammonia over iron and the catalysis of carbon monoxide on a Pt surface. The very fascinating scientific aspect of studying surfaces is, that theory and experiment look at the same dimensions, and - provided the system is not too complex - reach the same level of reliability. A very important property of surfaces in particular also in connection with their adsorption abilities is the surface structure, i.e. the spatial distribution of atoms in the surface and near surface layers. Considering only clean surfaces, for a pure metal in general the surface energy for different surfaces of the same metal may vary considerably. It is also possible that a reconstruction of the surface may lower surface energy, resulting in a different lattice arrangement than that in the bulk phase. If more complicated intermetallic compounds are studied in addition to the surface properties of pure metals the composition of the bulk face has great influence on the segregation profile, i.e. the concentration of the different species in the near surface regions. Adding adsorbate atoms on such surfaces complicates the situation even more. The presence of adsorbates can influence the ordering of the substrate significantly and as a second point the ordering can be strongly dependend on the amount of adsorbed atoms.

The most intriguing experimental tool for studying surfaces is the Scanning Tunneling Microscope (STM), which can "see" the atoms (provided, atomic resolution is achieved). Because of this feature STM is able to resolve local structural

properties. A second very important experimental tool for measuring surface structures is the Low-Energy-Electron-Diffraction (LEED), which gives the information about the long range ordering of the surface-layer atoms. In depth analysis of LEED spectra also allows to extract structural properties of a few layers below the actual surface layer.

From the point of view of a theoretically oriented scientist one tries to quantitatively describe the adsorption properties based on first principles only, without the need of any empirical adjusting and fitting. In particular when determining a stable adsorption structure one has to find that structure that has the lowest energy for a given set of enviromental variables. To do so the forces of a certain initial configuration need to be minimized in order to find the relaxed positions of the atoms.

With nowadays standards of computer power and software development such a concept can be pursued for systems and properties, which can be modelled by a few hundreds of atoms at maximum. Such a study is presented in this thesis by focussing on indium atomic adsorption on a tungsten (110) surface. In collaboration with experiments which were done at the University of Innsbruck LEED data is found to be in agreement with DFT data and molecular dynamics simulations.

But there are properties, e.g. the large scale ordering in dependence of the temperature, which cannot be described only by a finite set of DFT calculations alone. Large system sizes and huge configuration spaces are needed to get access to such quantities. The methods that have to be used for this purposes should require much less computational resources than DFT calculations but have its accuracy at the same time. A suitable tool to map the detailed energetics of a system found by a finite set of DFT calculations to large systems is the cluster expansion method (CE). Within this work the CE is adopted to the oxygen adsorption on the tungsten (110) surface to determine the ground state structures of this system and the ordering at finite temperatures. Since for the CE the energies of adsorption structures over the whole concentration range up to a full monolayer is available, a complete surface phase diagram can be constructed by performing Monte Carlo simulations that utilize the effective cluster interaction energies found by the CE.

The thesis is organized as follows: In chapter 2 the theoretical framework of DFT and CE is given. Chapter 3 focusses on the properties of the pure elements that are used as substrate or adsorbates. The application of the CE to the oxygen adsorption on the W(110) surface is investigated in chapter 4. Finally, in chapter 5 the adsorption of indium on the same surface is studied by using DFT in combination with molecular dynamics simulations.

2

Theoretical Aspects

In this chapter the theoretical basis for the methods -as applied in the present thesis- are presented. Starting with density functional theory in section 2.1, its fundamental concepts are discussed, and how it is applied for calculating ground state properties. In the following section 2.2 the concept of the cluster expansion is introduced in terms of a general overview. In addition to the standard formulation of the cluster expansion for bulk systems its extension and generalization to surface and adsorbate systems is elaborated. Section 2.4 introduces the thermodynamical framework which is used for modeling surface systems. Finally, section 2.5 shows how the cluster expansion of a particular system is constructed for practical applications, which is then connected with section 2.6 dealing with Monte Carlo simulations.

2.1 Density Functional Theory

The (non relativistic) stationary Schrödinger equation for a system of nuclei and electrons is

$$\hat{H}\Psi(\{\vec{r}_i\},\{\vec{R}_\alpha\}) = E\ \Psi(\{\vec{r}_i\},\{\vec{R}_\alpha\}) \tag{2.1}$$

with the wave function $\Psi(\{\vec{r}_i\},\{\vec{R}_\alpha\})$ depending on the coordinates $\vec{r}_i, i = 1, N$ (spins included) of all electrons and the coordinates $\vec{R}_\alpha, \alpha = 1, N_\alpha$ of all nuclei in the system. Separating the motion of electrons from the motions of the nuclei (which is done in the Born-Oppenheimer approximation) results in the Schrödinger equation for the electronic states,

$$\hat{H}_{el}(\{\vec{r}_i\},\{\vec{R}_\alpha\})\Psi_{el}(\{\vec{r}_i\}) = E_{el}\ \Psi_{el}(\{\vec{r}_i\}) \tag{2.2}$$

The Hamilton operator (in atomic coordinates)

$$\hat{H}_{el} = \sum_{i=1}^{N}(-\frac{1}{2}\vec{\nabla}_i^2) + \sum_{i=1}^{N} v(\vec{r}_i) + \sum_{i<j}^{N} \frac{1}{r_{ij}} \tag{2.3}$$

consists of the kinetic energy, the Coulomb interaction between electrons i and nuclei α, $v(\vec{r}_i) = -\sum_\alpha \frac{Z_\alpha}{r_{i\alpha}}$ and the electron-electron Coulomb interaction as the last term. Of course, the wave function has to be antisymmetric with respect to exchange of electrons, of which property the Pauli exclusion principle is the consequence.

Because the electronic Hamiltonian contains the Coulomb interaction of the electrons with the nuclei, the eigenvalue E_{el} depends implicitly on the spatial distributions of nuclei. Searching for the state of interest, the ground state of a system, the lowest energy of the electronic spectrum $E_{el,0}$ defines the ground state energy for a given distribution of nuclei (i.e. the crystal structure) at the positions $\{\vec{R}_\alpha\}$. The total energy of the ground state E_0 is the sum of the total electronic energy plus the Coulomb repulsion between the nuclei separated by their respective distances $R_{\alpha\beta}$,

$$E_0(\{\vec{R}_\alpha\}) = E_{el,0}(\{\vec{R}_\alpha\}) + \sum_{\alpha<\beta} \frac{Z_\alpha Z_\beta}{R_{\alpha\beta}} \tag{2.4}$$

In this equation the implicit dependence of the electronic ground state energy $E_{el,0}$ is written explicitly in order to illustrate that the total ground state energy can be understood as a potential energy, with all its terms being dependent on the positions of the nuclei.

Equation 2.2 for the electronic ground state energy $E_{el,0}$ can also be derived within a variational principle minimizing the total energy as a functional of the wave function,

$$E_{el,0} = \min_{\Psi_{el}} E_{el}[\Psi_{el}] \tag{2.5}$$

obeying the constraint of the normalization condition

$$< \Psi_{el}|\Psi_{el} >= 1. \tag{2.6}$$

The one-particle ground state electronic density $\rho(\vec{r})$ is derived from the ground state wave function by integrating over $(3N-3)$ coordinates (suitable sums over spins included)

$$\rho(\vec{r}) = N \int \dots \int d^3r_2 \dots d^3r_N |\Psi_{el}(\vec{r}, \vec{r}_2 \dots \vec{r}_N)|^2, \tag{2.7}$$

obeying the condition of the particle number conservation (i.e. the number of electrons N_{el} is constant),

$$\int \rho(\vec{r}) d^3r = N_{el}. \tag{2.8}$$

In the classical Schrödinger theory the causal sequence is the following: the Hamiltonian determines the wave function, which in addition has to obey the constraints enforced by normalization and boundary conditions. At the end, the density is determined by the equations 2.7 and 2.8. Because for a solid system the many-body wave function depends on many variables and therefore solving the Schrödinger equation directly for such a system is prohibitive. In order to find a practical solution for the ground state physicists tried to utilize the particle density $\rho(\vec{r})$ for solving the quantum physical equations and finding the ground state energy and related properties (for example, in terms of the famous Thomas-Fermi model [93, 32]). The tremendous gain of such a concept would be that $\rho(\vec{r})$ only depends on four variables, if the spin degree of freedom is added to the three spatial coordinates. However, all simple schemes based on the density utterly failed until the development of a rigorous theory, the density functional theory (DFT) [44]. In the first concept of DFT, the density $\rho(\vec{r})$ is the fundamental quantity, by which the Hamilton operator (and in particular, the so-called external potential $v(\vec{r})$ describing the electron-nucleus interaction), hence the ground state wave function and ground state total energy should be determined uniquely. The total energy of the electronic ground state $E_{el,0}[\rho]$ is now a functional of the density and can be decomposed into three contributions,

$$E_{el}[\rho] = T[\rho] + V_{ee}[\rho] + V_{ext}[\rho] \tag{2.9}$$

which are the functionals of the kinetic energy T, of the electron-electron interactions V_{ee}, and of the electron-nuclei interactions V_{ext} (the so-called external potential energy). Constructing a variational scheme for minimizing the ground state total energy under the constraint of particle conservation according to equation 2.8 resulted in the very elegant formulation involving functional derivatives and the chemical potential μ,

$$\mu = \frac{\delta E_{el,0}[\rho]}{\delta \rho} = v(\vec{r}) + \frac{\delta(T[\rho] + V_{ee}[\rho])}{\delta \rho}. \tag{2.10}$$

Unfortunately, this equation is useless for practical applications. Furthermore, a fundamental problem of the original formulation of DFT was that it required the strict uniqueness between density and external potential v. This mathematical problem can, however, be lifted.

For practical reasons the rather abstract original DFT was recast in terms of one-particle equations (in atomic units),

$$\left(-\frac{1}{2}\nabla^2 + v(\vec{r}) + v_{xc}(\vec{r})\right)\phi_i(\vec{r}) = \varepsilon_i\phi_i(\vec{r}) \tag{2.11}$$

which are the celebrated Kohn-Sham equations [49], as utilized in all practical applications (for example, also in the Vienna ab-initio simulation package VASP, which was used in the present work). The individual terms of the Hamiltonian are the *single-particle* kinetic energy, the already known external potential v of the electron-nuclei interactions, and the exchange-correlation potential v_{xc}, which comprises all electron-electron interaction including also the remaining contribution of the kinetic energy of the *interacting* electron system. The role of the Kohn-Sham orbitals ϕ_i consists in building up the true ground state density ρ by

$$\rho(\vec{r}) = \sum_{i=1}^{N} |\phi_i(\vec{r})|^2, \tag{2.12}$$

which provides the connection to the original DFT. The Kohn-Sham equations for the N electronic states have now to be solved self consistently. The total electronic energy of the ground state $E_{el,0}[\{\phi_i\}]$ of the system consists of several parts, involving the sum over all single-particle energies ε_i,

$$\begin{aligned} E_{el,0}[\phi_i] = \; & \sum_{i=1}^{N}\varepsilon_i - \frac{1}{2}\int\int \frac{\rho(\vec{r})\rho(\vec{r}')}{|\vec{r}-\vec{r}'|}d^3r d^3r' \\ & + E_{xc}[\rho] - \int v_{xc}(\vec{r})\rho(\vec{r})d^3r \end{aligned} \tag{2.13}$$

with the definition

$$v_{xc}(\vec{r}) := \frac{\delta E_{xc}[\rho(\vec{r})]}{\delta\rho} \tag{2.14}$$

involving the exchange-correlation energy functional which includes all many-body effects of the electronic states.

In analogy to equation 2.4 the complete total ground state energy E_0 is now the sum of the electronic energy $E_{el,0}$ and the nuclei-nuclei repulsions. The energy E_0 depends on the atomic positions $\vec{R_\alpha}$, the volume and unit cell shape. The crystal structure of the ground state is found by minimizing E_0 as a function of all these variables. Accepting the existence of the mapping of the many-body system onto the Kohn-Sham single-particle framework, the practicability of the Kohn-Sham equations for real applications depends on how well the inevitable approximations for the unknown exchange-correlation functionals of the many-body interactions, $E_{xc}[\rho]$ and $v_{xc}(\vec{r})$, are working.

2.1.1 Approximation of the Exchange-Correlation Functional

Historically, the first approximations were based on the homogenous interacting free electron gas in terms of so-called local approximations. The concept is, that locally at each point $\vec{r}$ the density ρ is known, and the unknown exchange-correlation functional $E_{xc}[\rho\vec{r}]$ is now replaced by the corresponding expression for the electron gas, which is known (it can be derived numerically). This so-called local density approximation (LDA) uses the exchange correlation energy per particle of a homogenous electron gas $\varepsilon_{xc}(\rho)$ for constructing the functional,

$$E_{xc}^{LDA}[\rho] = \int d^3r \ \rho(\vec{r})\varepsilon_{xc}(\rho(\vec{r})). \tag{2.15}$$

The LDA can be straightforwardly extended to a local spin density approximation, allowing for spin-polarization. Many parametrizations were invented for LDA functionals, for example by Vosko et al. [101] and Perdew et al. [77]. Although the replacement of the true ground state density (a rapidly varying function) by the homogenous electron gas (having a constant density) seems to be rather crude, it worked astonishingly well, and its computational costs are negligible. Nevertheless, for up-to-date accuracies, LDA very often is a too poor approximation, in particular in systems, which involve more localized states (for example, 3d-states transition metals, magnetic phases, surfaces, molecules). Further developments tried to compensate for the overbinding effect of LDA by going beyond the simple locality of LDA by including density gradients within the so-called generalized gradient approximations (GGA),

$$E_{xc}^{GGA}[\rho] = \int d^3r \ f(\rho(\vec{r}), \nabla\rho(\vec{r})). \tag{2.16}$$

Such an approximation might be named as semi-local. As for LDA, a variety of parametrizations exists. In the present work the GGA functional parametrized according to Perdew, Burke and Ernzerhof (PBE) is applied [76]. GGA corrects for many shortcomings of LDA. In general, the accuracy of the different exchange-correlation functionals is not known a priori. Comparison to experimental data is needed to find out the quality. As it turns out in section 3.1, LDA is more accurate for describing the lattice constant of tungsten than PBE. But the elastic properties represented by the bulk modulus are better described by the PBE approximation. In any case, GGA (or PBE in the present case) is strongly recommendable for surface and adsorption studies. For such systems, LDA is much too overbinding.

2.1.2 Implementation of DFT

Finally, it remains to discuss how the Kohn-Sham equations 2.11 are solved in practice. Or in other words, which type of basis functions are chosen for the actual numerical implementations. Concerning periodic boundary conditions, as it is customary for modeling solid materials, plane waves would be an ideal choice carrying automatically the Bloch symmetry with them. Furthermore, involving plane waves for building the Hamilton matrix elements, charge density and related quantities requires Fourier transformation, for which very fast numerical schemes are available. On the other hand, in cases in which the wave function varies strongly (for example, 3d-states, states at surfaces, molecules, states close to the nuclei) the convergence of a Fourier series is very bad. Therefore, a physically meaningful compromise has to be made, if one wants to keep the plane waves description. This is done by introducing so-called pseudopotentials, in which the bare nucleus-electron interaction is replaced by a screened ion-electron interaction. A vast experience in handling such techniques exists, and one of the most successful ones is the projected augmented wave (PAW) method [6]. The reader, who is more interested in an actual implementation of PAW, is referred to papers which deal with the Vienna Ab initio Simulation package VASP, which was used in the present study [52, 51, 53].

Knowing the dependency of the ground state total energy $E_0\{\vec{R_\alpha}\}$ on the positions of the nuclei, forces acting on the atoms or ions can be calculated and the atomic structure can be relaxed by changing the positions $\vec{R}_\alpha$ until all forces are (numerically) zero. If only the Hamiltonian depends explicitly on the positions $\vec{R}_\alpha$ the Hellmann-Feynman force [43, 35] acting on atom α is given by

$$\vec{F}_\alpha = -\frac{\partial E_0}{\partial \vec{R}_\alpha} = - < \Psi_{el,0} | \frac{\partial \hat{H}_{el}}{\partial \vec{R}_\alpha} | \Psi_{el,0} > . \tag{2.17}$$

If the basis functions $\tilde{\phi}$ –as used for modeling the true ground state wave function $\Psi_{el,0}$– depend explicitly on the positions (for example, in the full-potential linear augmented plane wave method) correction terms involving derivatives $\frac{\partial \tilde{\phi}}{\partial \vec{R}_\alpha}$ have to be added. This is, however, not necessary when only plane waves are used.

2.1.3 Computational remarks

For the cluster expansion studies –if not noted otherwise– all DFT energies are taken from fully relaxed structure optimizations. All forces typically were relaxed to be smaller than 0.01 eV/Å. If the simulation cell is connected to a heat bath the calculation of forces can be used to investigate finite temperatures by performing molecular dynamics (MD) simulations. An overview of the theoretical framework

for MD simulations can be found in references [2], [42] and [72]. For using MD simulations in adsorption studies in this work an asymmetric substrate slab of four tungsten layers with additional adatoms was used. During the MD simulation the symmetry within the simulation cell is not enforced allowing all atoms to move freely without constraints. For finding the equilibrium configurations usually a MD run is started at high temperatures and equilibrated for some pico seconds to ensure ergodicity of the system. Then the system is cooled down slowly to the temperature of interest.

2.2 Formulation of the Cluster Expansion

By application of DFT it is possible to calculate the total energies and the relative stabilities of arbitrary atomic structures as elaborated in the previous section (One might also refer to the atomic structure of a compound by the common term "phase". In literature related to cluster expansion usually the term "structure" or "configuration" is used). However, applying DFT in the standard manner has some limitations:

- The maximum system size is a few hundreds of atoms per unit cell. Even with very large computational resources this limitation cannot be stretched much further.

- For a variety of materials properties (in particular, thermodynamical properties) many different configurations (i.e. arrangements of atoms) are needed. Such a task is prohibitive if the number of configurations is very large.

- Standard DFT calculates the ground state properties at T=0 K. For temperature dependent phase stabilities of alloys the entropy of mixing is needed, which often cannot be directly derived from a set of DFT calculations.

- The search for the thermodynamical ground state of a solid system is still a very difficult problem. The cluster expansion offers a very elegant tool for that, and the ground state line is anyway needed for deriving phase stabilities. (It should be noted that alternative methods of searching for ground state structures with an unknown crystal structure exist (i.e. atomic positions and unit cell shape are unknown), for example the direct use of genetic algorithms as implemented by Oganov et al. [74].)

The cluster expansion method (CE) is an effective tool to overcome these limitations, and it can reach the accuracy of DFT calculations at the same time,

because it can be based on DFT data. The effective CE Hamiltonian is constructed by calculating a number of input structures with DFT. For all these structures forces are minimized with respect to the boundary conditions: for bulk systems the unit cell shape, unit cell volume and the local atomic positions are fully relaxed; for surface systems parts of the substrate is kept fixed and the surface atoms are allowed to relax. Consequently also the CE Hamiltonian is able to consider structural relaxation effects. (This is a major achievement of modern CE compared to the rigid scheme of the cluster variation.) Since the CE Hamiltonian is very fast to compute, very large configuration spaces become now accessible. The following sections will show the theoretical basis of the CE and the discussion afterwards deals with its practical implementation.

2.2.1 The Principles of the Cluster Expansion

The concept of the CE is based on an Ising Hamiltonian [45] for the lattice occupation. For each lattice site i a "pseudo" spin $\hat{S}_i$ is assigned [86]. The number of possible spins depends on the degrees of freedom which are considered. For binary systems each lattice site can take one of two spins (-1,+1), whereas for ternary systems one from three (-1,0,+1). In principle this concept is extendable to quaternary and even more complicated systems, but one should be aware that the configuration space rapidly grows [104] with the number of degrees of freedom. The present work focuses on the formulation of the binary CE. An extension to ternary systems can be found for example in reference [104]. As mentioned before in a binary system two types of atoms are considered. Type "A" is associated with spin "+1" and "B" with "-1", respectively. Any property $P(\sigma)$ which depends on the lattice occupation σ can be described by a sum of spin products (according to equation 2.18). The mathematical proof of this concept was given by Sanchez, Ducastelle and Gratias [86] about 25 years back. Examples for configuration dependent properties are the energy (enthalpy of formation or total energy) $E(\sigma)$ and the compressibility $\kappa(\sigma)$.

$$P(\sigma) = p_0 + p_1 \cdot \sum_i \hat{S}_i + p_2 \cdot \sum_{i<j} \hat{S}_i \cdot \hat{S}_j + p_3 \cdot \sum_{i<j<k} \hat{S}_i \cdot \hat{S}_j \cdot \hat{S}_k + \ldots \qquad (2.18)$$

The sum in equation 2.18 contains the parameters p_i which are independent of σ, whereas the spin products $\hat{S}_i \cdot \hat{S}_j$, $\hat{S}_i \cdot \hat{S}_j \cdot \hat{S}_k$ depend on the configuration σ (see for example [21, 34, 61]). To gain more information out of equation 2.18 the spin products have to be rearranged. For a particular spatial arrangement of k vertices or a so-called geometrical figure f the spin product Π_f is defined as

$$\Pi_f(\sigma) = \hat{S}_{1_f} \cdot \hat{S}_{2_f} \cdot \ldots \cdot \hat{S}_{k_f}. \qquad (2.19)$$

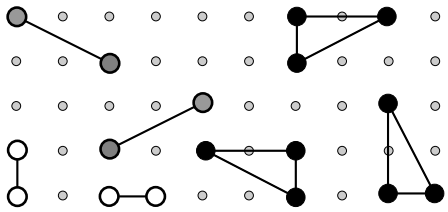

Figure 2.1: Example for different figures in a two dimensional lattice. For the two pair figures of different lengths (Grey and white vertices) and also for one triplet figure (black vertices) different symmetry equivalent analogues are sketched.

Out of all possible figures which appear in equation 2.18 subsets of symmetry equivalent figures are found. These figures can be transformed into each other by a symmetry operation of the lattice. Figure 2.1 shows two different pairs and one triple figure and for each of them different symmetry equivalent arrangements are sketched. The spin products of the symmetry equivalent figures are summed up in the so-called correlation function $\overline{\Pi}_F(\sigma)$ (equation 2.20) and normalized with respect to the number of of lattice sites N of the systems and the number of symmetry operations D_F.

$$\overline{\Pi}_F(\sigma) = \frac{1}{ND_F} \sum_{f \in F} \Pi_f(\sigma) \tag{2.20}$$

Due to its construction a number of useful relations for the correlation function can be found. For example, Lu et al. [61] derived completeness relations for the exact formalism. In the following, some practical guidelines for working with correlation functions are discussed:

- If for a figure the conjugate configuration $\overline{\sigma}$ of configuration σ is formed (see reference [56]) by replacing all A atoms by B atoms and vice versa, then the spins are related accordingly $S_i(\overline{\sigma}) = -S_i(\sigma)$. For pairs and other figures with even number of vertices the spin product within the correlation function remains the same:

  $$\overline{\Pi}_F(\overline{\sigma}) = \overline{\Pi}_F(\sigma) \tag{2.21}$$

  For figures with an odd number of vertices the correlation function changes sign:

  $$\overline{\Pi}_F(\overline{\sigma}) = -\overline{\Pi}_F(\sigma) \tag{2.22}$$

  As a consequence, if only even numbered figures for a CE were used, the values $P(\sigma)$ and $P(\overline{\sigma})$ would be the same, since the coefficients p_i are independent of σ and $\overline{\sigma}$. On the other hand if only odd figures with $k \geq 3$

were used the relation $P(\sigma) = -P(\overline{\sigma})$ would follow (Making use of p_1 would add a shift in energy which is linearly dependent on the concentration x; for comparison see equation 2.24.). Therefore, for a suitable formulation of the CE a mixture of odd and even figures is needed in order to be able to describe $P(\sigma)$ of a system $A_{1-x}B_x$ over the whole concentration range $0 \leq x \leq 1$.

- Two configurations are the same if *all* correlation functions are identical. Considering the whole set of correlation functions this statement is obvious. But when working in practice with the CE using only a finite set of allowed figures, two different structures may appear identical, since for the currently chosen figure set the correlation functions have the same values.

- The correlation function for a perfectly random alloy of a figure F with k vertices is [33, 61]:
$$\langle \overline{\Pi}_F \rangle = (2x-1)^k \tag{2.23}$$

- The first term of equation 2.18 is the constant contribution p_0 since no spins are attached to it.

- The second part of equation 2.18, which includes the sum over the single spins, can be evaluated directly by summing over the spins:
$$p_1 \sum_i \hat{S}_i = p_1(N_A - N_B)/N = p_1(2x-1) = p_1\overline{\Pi}_1(\sigma). \tag{2.24}$$
In this equation, N_A and N_B are the number of A and B atoms, N is the total number of lattice sites N_A+N_B and x the concentration of the atom type "A" ($(1-x)$ that of atom type "B" respectively). Because the correlation function for this so-called onsite term only depends on the concentrations of A and B atoms and not on their particular configurations, a general expression for $\overline{\Pi}_1$ can be derived. Inverting equation 2.24 results in a relation for the concentration of the system in terms of its onsite correlation function:
$$x = \frac{1}{2} + \frac{\overline{\Pi}_1}{2} \tag{2.25}$$

The same results can also be gained when starting from an occupation operator $\Gamma_s(i)$ which counts all atoms of type s at site i, as demonstrated by Mohri (see reference [78], pp 527-534):
$$\Gamma_s(i) = \frac{1}{2}(1 + s \cdot \hat{S}_i) \tag{2.26}$$

For atom type A in a binary alloy, s is equal 1 resulting in $\Gamma_1(i) = 1$ if an atom of type A is located at site i, or 0 if an atom of type B is located at this site. As a consequence, the probability of finding an atom of type s with concentration x_s is then given by

$$x_s = \frac{\sum_{i=1}^{N} \Gamma_s(i)}{N} = \frac{1}{2}\left(1 + s\frac{N_s - (N - N_s)}{N}\right) = \frac{1}{2}\left(1 + s\langle\overline{\Pi}_1\rangle\right), \tag{2.27}$$

which is identical to equation 2.25. In the following, an expression for y_{st}, the probability of finding a pair figure of defined length is derived:

$$y_{st} = \frac{1}{N_{pairs}} \sum_{i=1}^{N} \sum_{j=1}^{N} \Gamma_s(i)\Gamma_t(j) \tag{2.28}$$

Simplifying equation 2.28 leads to:

$$y_{st} = \frac{1}{2^2}\left(1 + (s+t)\langle\overline{\Pi}_1\rangle + s \cdot t\langle\overline{\Pi}_{pair}\rangle\right) \tag{2.29}$$

Equation 2.29 contains both the onsite correlation function and the pair correlation function of the pair distance st under consideration. In general, calculating the probabilities of figures with arbitrary number of vertices k always results in expressions which contain correlation functions of figures with less than k vertices.

After discussing the properties of the correlation function the simple spin products in equation 2.18 finally can be replaced leading to a more compact formulation of equation 2.30:

$$\begin{aligned} P(\sigma) &= p_0 + p_1 \cdot (2x - 1) + ND_{F_1} \cdot \overline{\Pi}_{F_1}(\sigma) \cdot p_{F_1} + \\ &\quad + ND_{F_2}\overline{\Pi}_{F_2}(\sigma) \cdot p_{F_2} + ND_{F_3}\overline{\Pi}_{F_3}(\sigma) \cdot p_{F_3} + ... \end{aligned} \tag{2.30}$$

This equation contains –apart from the configurational independent terms with p_0 and p_1– the configuration dependent terms for each figure F_i. The set of figures F_i consists of all possible pairs, triplets, quadruplets and higher order figures. In some cases (see for example reference [9] and as it will be discussed later on), a formulation of the CE is useful in which an explicit distinction of the pairs and higher order many body figures (MB) is made:

$$\begin{aligned} P(\sigma) &= p_0 + p_1 \cdot (2x - 1) + \\ &\quad + \sum_{pairs} p_{pair} D_{pair} \overline{\Pi}_{pair}(\sigma) + \\ &\quad + \sum_{MBs} p_{MB} D_{MB} \overline{\Pi}_{MB}(\sigma) \end{aligned} \tag{2.31}$$

In the concept as described by equations 2.30 and 2.31 neither any approximations are made nor any parameters are omitted. That the discussed formulation indeed is exact was proven by Sanchez et al. [86] in 1984. The fundamental concept of the CE is that the interaction parameters $\{p_n\}$ can be explicitly extracted. Knowledge of these parameters would allow to calculate the property $P(\sigma)$ for an arbitrary configuration σ. Inspecting the sums of equation 2.31 more closely it is obvious, that the number of terms in the sums is of the order 10^{23} for both sums, which cannot be handled for practical application for real systems. In practice, however, the atomic interactions are more or less short-ranged, and they are predominantly determined by figures consisting of short distances on the scale of ≈ 10 Å. Considering only figure sets up to such distances reduces the number of figures in the CE expansion to the order of a few hundreds. Since this number of figures is still very large, a certain subset of these figures has to be chosen which describes the property under consideration sufficiently accurate. Discussing the choice of such subsets, in section 2.5 a detailed description of how to select the important figures and the determination of their respective interaction energies is given. Since equation 2.30 is very general at this point we introduce the enthalpy of formation $\Delta H_f(\sigma)$ as the physical property we are interested in. For binary systems it is the energy difference of configuration σ with respect to the most stable bulk phases of the (pure) constituents:

$$\Delta H_f(\sigma) = E_{tot}(\sigma) - x \cdot E^A_{tot}(a^A_{eq}) - (1-x)E^B_{tot}(a^B_{eq}). \tag{2.32}$$

The quantity $E_{tot}(\sigma)$ is the total energy per atom of a fully relaxed DFT calculation for configuration σ, the energies $E^A_{tot}(a^A_{eq})$ and $E^B_{tot}(a^B_{eq})$ are the total energies per atom of the pure phases A and B at their equilibrium bulk structures and, finally, x is the concentration of atoms A in the alloy. For the energy difference or formation energy $\Delta H_f(\sigma)$ equation 2.30 is restated and the abstract interactions p_{F_i} are replaced by the effective cluster interactions J_{F_i}:

$$\Delta H_f(\sigma) = ND_{F_1} \cdot \overline{\Pi}_{F_1}(\sigma) \cdot J_{F_1} + ND_{F_2}\overline{\Pi}_{F_2}(\sigma) \cdot J_{F_2} + ND_{F_3}\overline{\Pi}_{F_3}(\sigma) \cdot J_{F_3} + ... \tag{2.33}$$

Because the correlation function is a dimensionless quantity the effective cluster interactions have energy as their physical dimension. Therefore, the product of the correlation function and the interaction energy of a figure represents the energy contribution to the enthalpy of formation of the current configuration.

2.2.2 Mixed-Space Cluster Expansion

Up top this point, the ansatz of the CE is not working properly for all kind of systems, i.e. atomic arrangements or crystal structures. Laks et al. [56] showed

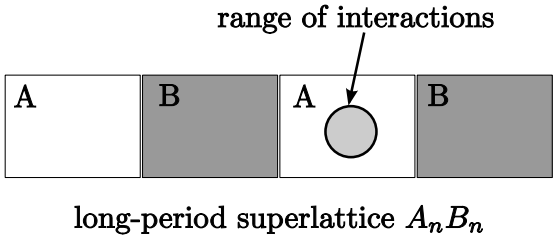

Figure 2.2: Long-period superlattices A_nB_n as studied by a CE. For large n the figures used by the CE (indicated by the grey circle) are by far too small to cover the whole length of the period. Consequently, atoms are surrounded by atoms of the same kind, giving a zero contribution to the enthalpy of formation of the alloy. For a correct treatment of such a system a mixed space CE has to be applied. For details see text.

that for long-period superlattice compounds A_nB_n the formulation of section 2.2.1 leads to wrong results. Even for a period length of only $n = 3$ the energies are not predicted correctly by the CE, when compared to DFT calculations. For $n \to \infty$ the formation energy ΔH_f is predicted to be zero since most of the A and B atoms are enclosed by its own species, giving therefore a contribution of zero to ΔH_f. To overcome these inherent problem of long-period superlattices the mixed space concept was introduced into the cluster expansion. For a correct calculation of the enthalpy of formation of a long-period superlattice structure the constituent strain energy due to the lattice mismatch has to be added, and in a second step a number of interaction energies have to be transformed into a reciprocal lattice representation [69]. Starting with equation 2.33, which is split into sums over pairs and many-body figures, the constituent strain energy $\Delta E_{CS}(\sigma)$ is added:

$$\begin{aligned} P(\sigma) &= J_0 + J_1 \cdot (2x-1) + \\ &\quad + \sum_{pairs} J_{pair} D_{pair} \overline{\Pi}_{pair}(\sigma) + \\ &\quad + \sum_{MBs} J_{MB} D_{MB} \overline{\Pi}_{MB}(\sigma) + \\ &\quad + \Delta E_{CS}(\sigma) \end{aligned} \tag{2.34}$$

A detailed derivation of the coherent-strain energy $\Delta E_{CS}(\sigma)$ is given in a number of papers [56, 105, 69]. In principle, for its calculation according to equation 2.35 the equilibrium constituency strain energy $\Delta E^{eq}_{CS}(x, \hat{k})$ needs to be known. It requires the knowledge of the epitaxial energies of the constituents for an arbitrary direction, which is demonstrated for example in reference [69]. The second part, which enters equation 2.35, is the structure factor $S(\hat{k}, \sigma)$ (equation

2.36) which is the Fourier transform of the distributions of spins S_j at sites R_j spanning the underlying lattice.

$$\Delta E_{CS}(\sigma) = \sum_k \frac{\Delta E_{CS}^{eq}(x,\hat{k})}{4x(1-x)} |S(\hat{k},\sigma)|^2 \tag{2.35}$$

$$S(\hat{k},\sigma) = \sum_j S_j \exp(-i\hat{k}R_j) \tag{2.36}$$

Considering now the Fourier transforms of a group of figures, it is possible to do Fourier transforms for figures also with a larger number of indices than two. In practice, only for the pair figures simple expressions exist, and therefore only for the pairs a Fourier transform is done analytically [56], resulting finally in equation 2.37. Again, as in equation 2.35 the structure factor of equation 2.36 enters with the interaction energies $J_{pair}(k)$ of the pair figures now in k-space. This sum is nonzero only for a finite number of k-points [56], namely for $k = 0$ and k-points that are reciprocal lattice vectors of the unit cell of the configuration σ:

$$\begin{aligned} P(\sigma) = {} & J_0 + J_1 \cdot (2x-1) + \\ & + \sum_k J_{pair}(k) |S(\hat{k},\sigma)|^2 + \\ & + \sum_{MBs} J_{MB} D_{MB} \overline{\Pi}_{MB}(\sigma) + \\ & + \Delta E_{CS}(\sigma) \end{aligned} \tag{2.37}$$

2.2.3 Short Range Order Parameters and Correlation Functions

For comparison with structural experimental data either real space data taken for example from scanning tunneling microscope (STM) experiments or reciprocal space data derived from diffraction experiments can be used. For quantitative comparison, some kind of short range order parameter is very useful. A lucid derivation of the commonly used Warren-Cowley short range order parameter [17] is found in reference [69]. The definition of the short range order parameter α in equation 2.38 is given in terms of the conditional probability $P_{lmn}^{A(B)}$, which is the probability of finding a B atom at distance lmn when an atom A is at the origin, divided by the probability x (i.e. the concentration of the atom type A) of finding an atom A at all in the lattice:

$$\alpha_{lmn} = 1 - \frac{P_{lmn}^{A(B)}}{x} \tag{2.38}$$

For α_{lmn}, three different parameter ranges can be distinguished:

- $\alpha_{lmn} > 0$: phase separation
- $\alpha_{lmn} = 0$: total disorder
- $\alpha_{lmn} < 0$: ordered system

Comparison of the short range order parameter α_{lmn} with data from a CE can be easily done. For the calculation of the Warren-Cowley short range order parameter from the correlation functions in analogy to reference [69] a nearest neighbor correlation parameter Γ_{AB} is defined, being the difference of the probability of finding an A-B pair of a certain bond length and the probability $x_A x_B$ corresponding to a totally disordered system:

$$\Gamma_{AB} = \frac{1}{2} P_{AB} - x_A x_B \tag{2.39}$$

Inserting in equation 2.29 the probability of finding A-B and B-A pairs and the probability of finding an atom A or B according to equation 2.25 results in the expression

$$\Gamma_{AB} = -\frac{1}{4} \left(\langle \overline{\Pi}_{pair} \rangle - \langle \overline{\Pi}_1 \rangle^2 \right). \tag{2.40}$$

α_{lmn} is then given as the fraction of the Γ_{AB} and $-x_A x_B$ [9, 69]:

$$\begin{aligned} \alpha_{lmn} &= \frac{-\frac{1}{4} \left(\langle \overline{\Pi}_{pair} \rangle - \langle \overline{\Pi}_1 \rangle^2 \right)}{-\left(\frac{1}{2} + \frac{\langle \overline{\Pi}_1 \rangle}{2} \right) - \left(\frac{1}{2} - \frac{\langle \overline{\Pi}_1 \rangle}{2} \right)} = \\ &= \frac{\langle \overline{\Pi}_{pair} \rangle - \langle \overline{\Pi}_1 \rangle^2}{1 - \langle \overline{\Pi}_1 \rangle^2} \end{aligned} \tag{2.41}$$

If needed the parameter α_{lmn} can be transformed into reciprocal space [9] according to

$$\alpha_{lmn}(x, \vec{k}) = \sum_{lmn=1}^{n_R} \alpha_{lmn}(x) \exp(ikR_{lmn}), \tag{2.42}$$

in which R_{lmn} is the real space vector connecting the the pair lmn, and the number n_R is the number of neighbor shells that are used in the transformation.

2.2.4 Temperature Dependent CE

So far, for the formulation of the CE temperature dependency is only available via the configurational entropy which can be derived from Monte Carlo utilizing the parameters of the CE. Recently, efforts are on the way to extend the CE for taking into account temperature dependent effective interaction energies

$$J_F \rightarrow J_F(T). \tag{2.43}$$

In particular for investigations in which contributions of the vibrational (or phonon) free energy $F_{ph}(t)$ to the enthalpy of formation are included, the interaction energies will then depend on temperature. The enthalpy of formation of equation 2.32 is extended including now temperature dependent differences of vibrational free energies. In reference [78] (pp. 601-606) the phonon free energy $F_{ph}(T)$ (equation 2.44) is defined and a general introduction to how to calculate phonon spectra and vibrational free energies in the harmonic approximation is given. The vibrational free energy $F_{ph}(T)$ is the sum of the internal energy (equation 2.45) and the vibrational entropy (equation 2.46). For evaluation of these two integrals, the phonon density of states $g(\omega)$ is needed. All the needed quantities are based on force constants, which can be calculated by the same DFT approach as used for the calculation of electronic structure and electronic total energy. The relations for the vibrational free energy terms are:

$$F_{ph}(T) = U_{ph}(T) - TS_{ph}(T) \tag{2.44}$$

$$U_{ph}(T) = \frac{1}{2}\int_0^\infty g(\omega)\hbar\omega \coth\left(\frac{\hbar\omega}{2k_BT}\right) d\omega \tag{2.45}$$

$$S_{ph}(T) = k_B \int_0^\infty g(\omega)\left(\frac{\hbar\omega}{2k_BT}\left[\coth\left(\frac{\hbar\omega}{2k_BT}\right) - 1\right] - \ln\left[1 - \exp\left(-\frac{\hbar\omega}{k_BT}\right)\right]\right) d\omega \tag{2.46}$$

The modified version of equation 2.32 is equation 2.47 in which for each contribution $E_{tot}^{struc}(\sigma)$, $E_{tot}^{A}(a_{eq}^{A})$, $E_{tot}^{B}(a_{eq}^{B})$ the vibrational contribution is added. As a consequence, the energy difference $\Delta H_f^{ph}(\sigma, T)$ also depends on temperature, which is of importance for the CE.

$$\begin{aligned} \Delta H_f^{ph}(\sigma,T) &= E_{tot}^{struc}(\sigma) + F_{ph}^{struc}(\sigma,T) - \\ &- x\cdot[E_{tot}^{A}(a_{eq}^{A}) + F_{ph}^{A}(a_{eq}^{A},T)] - \\ &- (1-x)[E_{tot}^{B}(a_{eq}^{B}) + F_{ph}^{B}(a_{eq}^{B},T)] \end{aligned} \tag{2.47}$$

Since the phonon contributions may strongly differ for different structures, varying the temperature may not only change the ground state line –as introduced in section 2.4.1– because of the change of the numerical values of the ground state energies. More significant, its shape or the even the ground state structures themselves might change. The CE, which includes vibrational free energies, requires now the determination of the interaction energies at different temperatures which naturally leads back to equation 2.43. In order to get strict temperature dependent interaction energies one in principle has to converge a CE for each considered temperature T. Thus the computational effort can be quite

large, because the number of structures that have to be calculated can grow considerably, when structural stabilities (i.e. relative energy differences) change with varying temperature

2.3 Cluster Expansion for Surfaces

In the previous sections the CE method for bulk systems was introduced. In the following sections the CE formalism is extended to special systems, which are of importance for the present work. Two specialized CEs will be discussed in the following: a CE for surfaces and a CE for adsorption simulations. To be more specific, for the present study a CE is elaborated which is valid for an adsorbate system with a clean surface without changes in the surface composition or composition of subsurface layers. By these model conditions, the overall adsorbate system is a binary system, and an ansatz for a binary CE with respect to representative adsorption sites is suitable. In principle, it is possible to make an adsorption study also for the surface of an binary alloy: for example for studying the change in surface (or near surface) composition upon adsorption of another species. This problem then has to be treated by a quaternary CE since for the substrate two species and two species for the adsorbate have to be treated (one species for the adsorbate itself, one for the possible unoccupied adsorption sites).

2.3.1 Extension of CE to Surfaces

For bulk properties the CE is well established. If one considers surfaces, the reduced symmetry and the related relaxation of surface layers has to be taken into account. Breaking of symmetry leads to a much larger amount of figures required for the CE, and furthermore, the degeneracy D_F is lifted partially (see references [23, 25, 30, 70]). The bulk nearest neighbor (NN) pair interactions in figure 2.3 for example is split into different intra- and interlayer interactions in the surface area. A particular bulk interaction J_{NN}^{bulk} now in a (sub)surface layer is split into NN several interactions J_{i-j}^{surf} with all possible combinations of the layer numbers i and j. Because the CE becomes now layer dependent, the relation

$$J_{1-2}^{surf} \neq J_{2-2}^{surf} \neq J_{2-3}^{surf} \neq J_{NN}^{bulk} \tag{2.48}$$

is now obvious.

In general, the modeling of surfaces is much more complicated, since many more interactions have to be taken into account. The interactions $\{J(\vec{R})\}$ are thus not only distinguished by their shape but also by their relative position $\vec{R}$ with respect to the surface plane. The computational effort is increased twofold with

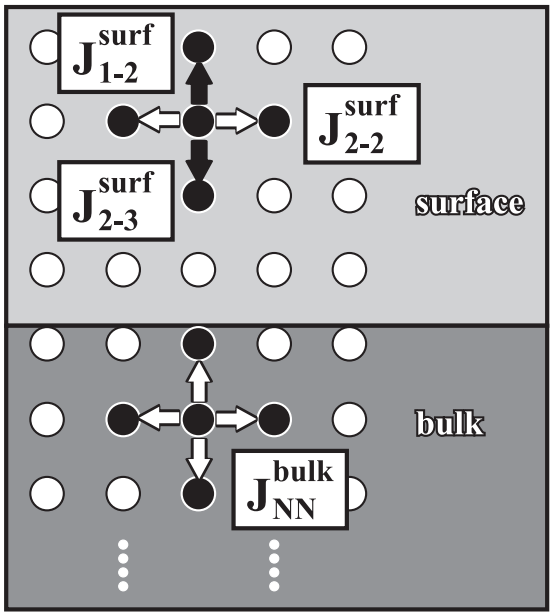

Figure 2.3: Side view of an intermetallic system. For the nearest neighbor pair interaction near the surface the degeneracy is lifted. As a result the bulk interaction J_{NN}^{bulk} is split up into an intra-layer interaction J_{2-2}^{surf} and inter-layer interactions J_{1-2}^{surf} and J_{2-3}^{surf}

respect to the bulk situation: Firstly, the higher complexity requires significantly more input structures for the construction of the CE Hamiltonian, and secondly, surface structures are computationally more costly since also a certain amount of vacuum has to be added to the super cell and, because of that, the number of basis functions increases. In order to keep the effort as low as possible, a surface CE is constructed as follows: For the surface that should be studied, first a CE for the bulk is done. Afterwards the surface CE is constructed as a correction to the bulk CE.

It can be learned form equation (2.33) that the contributions of each figure to the enthalpy of formation have to be summed up. This is the reason, why the surface CE can be considered as a correction of the bulk CE. One starts with effective interactions $\{J_F^{Vol}\}$ for the bulk and determines the deviation $\delta J_F^{OF}(\vec{R})$ depending on the distance $\vec{R}$ to the surface (see equation 2.49).

$$J_F^{OF} = J_F^{Vol} + \delta J_F^{OF}(\vec{R}) \tag{2.49}$$

This construction is designed in such a way that for distances further away from the surface (towards the bulk) the deviation vanishes ($\delta J_F^{OF} \to 0$). According to the definition of the interaction energies for the surface CE the formalism for the

bulk CE (2.33) is extended by an additional term including now $\delta J(\vec{R})$.

$$\Delta H_f^{surf}(\sigma) = N \sum_F D_F^{Vol} \cdot \overline{\Pi}_F^{Vol}(\sigma) \cdot J_F^{Vol} + N \sum_{F'} D_{F'}^{OF} \overline{\Pi}_{F'}^{OF}(\sigma) \cdot \delta J_{F'}^{OF}(\vec{R}) \quad (2.50)$$

For a surface CE the DFT calculations are set up by a repeated supercell approach. The surface of orientation (lmn) of a bulk crystal structure is modelled by a repeated (periodic) slab which consists of a number of bulk-like layers plus a number of surface layers, that are considered for the surface CE. In addition a suitable amount of vacuum is added to the supercell so that no interaction between two neighboring unit cells across the vacuum is possible. Throughout all DFT calculations the atom positions of the bulk part are kept fixed at the bulk lattice spacing without changing the configuration. In the surface layers, which are considered in the CE, different configurations (i.e. lattice occupations) are allowed and for each configuration the forces within the DFT calculations are minimized. For describing the surface energetics the surface formation enthalpy $\Delta H_f^{surf}(\sigma)$ (equation 2.51) is now introduced.

$$\Delta H_f^{surf}(\sigma) = E_{tot}(\sigma) - xE_{tot}^{Surf}(A) - (1-x)E_{tot}^{Surf}(B) \quad (2.51)$$

In comparison to equation 2.32 now the energies $E_{tot}^{Surf}(A)$ and $E_{tot}^{Surf}(B)$ are chosen as reference energies. The calculation of $\Delta H_f^{surf}(\sigma)$ and the corresponding setup of the DFT slabs is shown in a pictorial way in figure 2.4. For all slabs the configuration of the bulk part (enclosed in a grey area) is kept fixed. The first slab represents E_{tot} and shows an arbitrary configuration of A and B atoms, in the second and third slab for the reference energies $E_{tot}^{Surf}(A)$ and $E_{tot}^{Surf}(B)$ the surface area is filled completely with A or B atoms. The definition of equation 2.51 is given for a asymmetric setup of the DFT calculations. If symmetric slabs are used a factor of 1/2 has to be multiplied on $\Delta H_f^{surf}(\sigma)$. As a consequence of this analogous formulation all arguments in section 2.5 which deal only with ΔH_f for bulk systems, are also valid for surface CEs, when ΔH_f is replaced by ΔH_f^{surf}. The only change has to be made when constructing the ground state diagram. The formulation of equation 2.51 is not suitable, since for the fixed bulk configuration only the stability of the surface layers relative to this specific bulk configuration can be given. The construction principle of section 2.4.1 can be transferred, but instead of the term "ground state diagram" one should rather use the term "surface stability diagram".

2.3.2 Cluster Expansion for Adsorbates

Another class of systems which can be tackled by the the CE are adsorbates on surfaces [26, 88, 24, 115, 57]. Compared to the bulk and surface CE as discussed

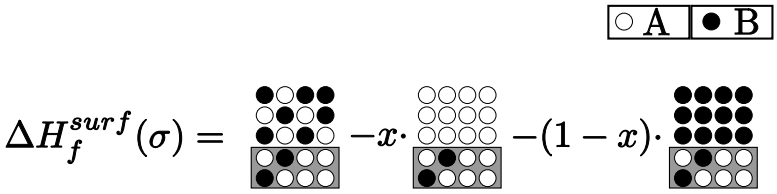

Figure 2.4: Definition of the surface formation energy $\Delta H_f^{surf}(\sigma)$. The reference energies used are shown in a pictorial way as side views of the surface slabs. For all slabs the bulk part (Grey area) is the same and kept fix, whereas the composition of the surface layers changes and the atomic positions are allowed to relax. As reference energies slabs with surface regions filled completely with atoms of sort "A" and "B" are used. For details see text.

so far, a CE for adsorption is a quasi two-dimensional problem. However a complication arises, because on surfaces in general different adsorption sites may have to be considered. If that is the case, then the CE has to be made for a suitable number of sublattices (see for example reference [57]). The CE for adsorbates as defined in equation 2.52 consists solely of interaction energies $J_F^{ad}(\vec{R})$ which are adsorption-site dependent. The bulk reference as implemented in the surface CE of equation 2.50 vanishes since only the contact of a well defined surface structure with atoms or molecules of the gas-phase is studied.

$$E_{surf}(\sigma) = N \sum_F D_F^{ad} \overline{\Pi}_F^{ad}(\sigma) \cdot J_F^{ad}(\vec{R}) \tag{2.52}$$

For the DFT calculations the surface formation energy

$$E_{surf}(\sigma) = \underset{\text{TiO}_2}{E_{tot}(\sigma)} \quad \underset{\text{TiO}_2}{-x_o \cdot E_{full}} \quad \underset{\text{TiO}_2}{-(1-x_o) \cdot E_{clean}} \tag{2.53}$$

is introduced. It expresses the energy gain of the total energy $E_{tot}(\sigma)$ of an adsorbate structure σ with respect to the total energy E_{tot}^{full} of the adsorption phase of the maximum coverage (typically one monolayer) and the total energy E_{tot}^{clean} of the clean surface. The relation of E_{surf} to the Gibbs free energy of a surface system is given by a Legendre transformation and explained in detail in section 2.4.2. For the determination of ground state structures and the implementation of the CE the arguments for the adsorbate CE remain the same. At all places where a ΔH_f in the following sections is occurring it can be replaced by E_{surf}.

2.4 Ground State Properties of a System

In the previous sections the theoretical framework of the CE was introduced. Before its implementation will be discussed, the ground state diagram, which shows the stable phases of a system needs to be introduced. Because in the present work standard DFT calculations provide the basic data (i.e. the cluster interaction energies) the ground state diagram is strictly valid only at T=0 K. In general however, CE and the corresponding ground state diagram of a system can be made temperature dependent (see remarks in section 2.2.4)) For bulk systems the ground state diagram is formulated in terms of the enthalpy of formation ΔH_f as defined in equation 2.32. For a CE of surfaces of a binary system with a fixed composition only a surface stability diagram can be constructed (see for example reference [90]). It should be noticed, that a change in bulk composition can influence the segregation behavior of the system. For such a class of systems the surface enthalpy of formation ΔH_f^{surf} (equation 2.51) is the key quantity. For adsorbate systems the ground state diagram is constructed by calculating the surface formation energy according to equation 2.53. Furthermore, the ground state formalism of section 2.4.1 will be related to the free energy formulation of other authors in section 2.4.2 thus connecting two equally valid ways of describing the same properties of a system.

2.4.1 Ground State Diagrams

A common way of displaying the ground states of a system is the ground state diagram shown in figure 2.5 in which the concentration versus the enthalpy of formation is plotted. Each phase (i.e. compound with a given crystal structure) which is shown in the ground state diagram, is marked by single point. The ground state line forms a convex hull around all other enthalpy of formations (see also figure 2.6). Mathematically the function value of a straight line connecting the two neighboring stable phases of a particular ground state with concentration x_0 is higher or equal in value (i.e. energy) at x_0 (see figure 2.6 and equation 2.54).

$$\Delta H_f(\sigma) < \frac{x(\sigma) - x(\beta)}{x(\alpha) - x(\beta)} \Delta H_f(\alpha) + \frac{x(\sigma) - x(\alpha)}{x(\alpha) - x(\beta)} \Delta H_f(\beta) \tag{2.54}$$

In addition to the existence of the ground states also their stability can be extracted from figure 2.5. Certainly the stability of the ground state at $x = 0.25$ (indicated by the dashed lines) is less than that at 0.75. The thermodynamical stability at T=0 K, $\Delta E_{stab}(x)$ of a ground state with a given concentration x can be defined as the difference of its formation energy with respect to the value of the straight line connecting the energies of its neighbouring phases (see also figure

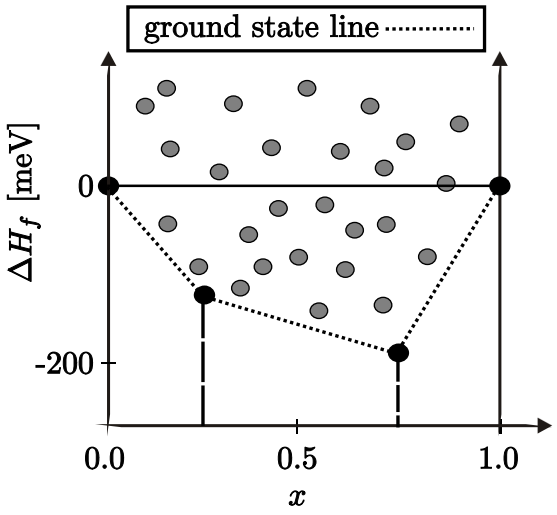

Figure 2.5: Ground state diagram for a bulk system. It shows the concentration of the system versus the enthalpy of formation of the studied phases. Each calculated phase is indicated by a single point. The ground state line is given by a convex hull around all phases according to equation 2.54.

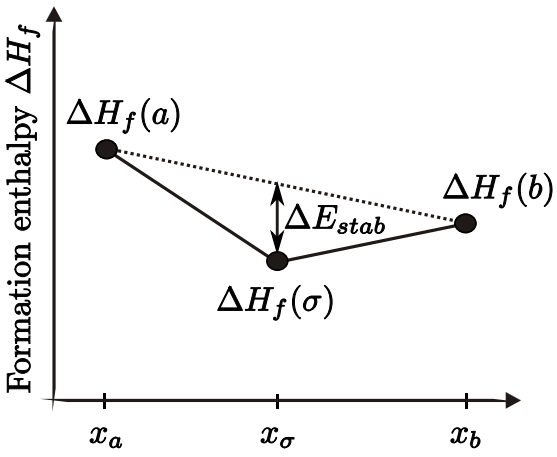

Figure 2.6: Construction of the ground state line: If the enthalpy of formation ΔH_f for a phase σ of concentration x_σ is more negative than the value of the straight line connecting the enthalpy of formations of the neighboring structure "a" and "b" with concentrations x_a and x_b then the phase σ is the ground state of the system. The mathematical formulation of the ground state line can be found in equation 2.54.

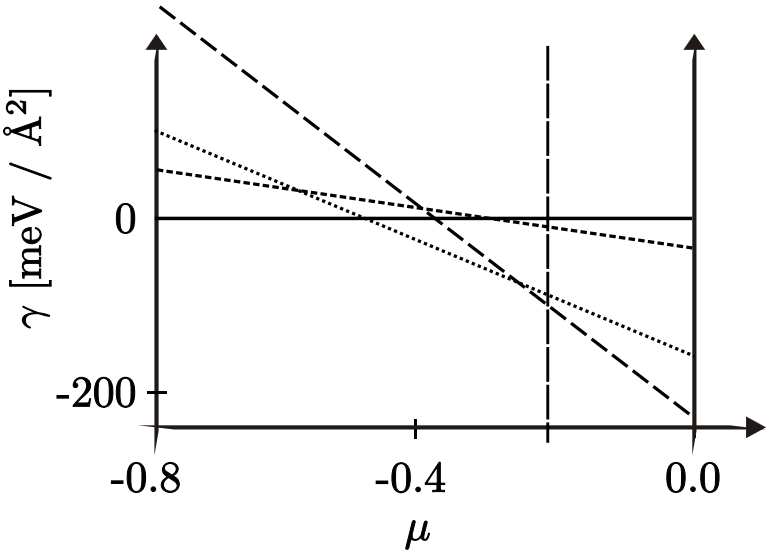

Figure 2.7: A possible ground state diagram for a surface system. In the plot the chemical potential is plotted against the surface free energy of the system. The lowest lying straight line marks the range of stability for its connected structure, being the ground state in this range.

2.6). Examples for the stability $\Delta E_{stab}(x)$ will be given in section 4.8. When converging a cluster expansion, a ground state diagram like that in figure 2.5 is constructed at different steps of the self-consistent CE workflow, see for example references [34, 69]. From the input phases, which were calculated by DFT, a ground state diagram is constructed in order to identify the stable structures of this set. If the effective interaction energies were determined, the energies of a huge number of structures is calculated by using the CE Hamiltonian. For this CE derived set a ground state diagram is constructed, and its ground state line is compared to the DFT result. It is certainly possible, that new ground state phases are predicted by the CE, which were not yet included into the original DFT set.

For surface systems another way of displaying the ground states exists. Figure 2.7 shows the the chemical potential μ_O versus the surface free energy γ of an oxygen adsorption system. For a certain structure the surface free energy depends linearly on μ_O, and therefore for each structure in the diagram a straight line is drawn. The stable structure at a given chemical potential is then that one with the lowest γ. The set of ground states are marked as a connected series of lines giving the lowest fringe of all considered structures in the diagram. In figure 2.7 some further points are noticeable. The horizontal line, which is a constant surface free

energy with respect to chemical potential, marks the clean surface. The vertical line at $\mu \approx -0.2$ eV marks the chemical potential of the corresponding bulk oxide, which is the upper limit at which a bulk phase would form. Furthermore, the ground state diagram of figure 2.7 can be transformed into a ground state diagram of the type shown in figure 2.5, namely by a Legendre transformation as described in section 2.4.2.

2.4.2 Surface Free Energy

Before giving a detailed description of surface processes the thermodynamic basis for such systems has to be defined. For a given set of environmental variables (e.g. pressure, temperature, chemical potential) the system will always equilibrate in the most stable surface structure under these conditions. The thermodynamic potential, which is well suited for describing the thermodynamics of surfaces is the Gibbs free energy $G(T, p, \{N_i\})$, which is a function of pressure, temperature and number of particles. The quantity which is calculated for a surface system is the surface free energy or surface energy γ (see for example Lozovoi et al. [59] and Reuter et al. [79]). The surface free energy γ_s per area A is defined in equation 2.55 where G_{struc} is the Gibbs free energy, and n_i the number of particles of species i with its chemical potential μ_i. The meaning of μ_i in equation 2.55 is just the Gibbs free energy per particle of species i. Therefore, the quantity γ_s is the excess energy of the structure under consideration with respect to its constituents. Of course, the chemical potentials μ_i can vary under different ambient conditions and thus γ_s will change correspondingly. In most cases γ_s is only dependent on the chemical potential of one species and the others are assumed to be constant since the surface is assumed to be in equilibrium with the underlying substrate.

$$\gamma_s\left(\{\mu_i\}\right) = \frac{1}{A}\left(G_{struc} - \sum n_i \mu_i\right) \tag{2.55}$$

The formulation of γ_s allows also a reinterpretation of the ground state diagram in figure 2.7. The simplest case, which can be considered, is the adsorption of a single species on a surface. Then the energy γ_s depends only on one chemical potential, μ_{ad}. For a clean surface, on which no adatoms are present, the energy $\gamma_s(\mu_{ad})$ is then independent of the chemical potential of the adsorbed species resulting in a horizontal line in the ground state diagram.

$$\gamma_s^{clean}(\mu_{ad}) = \frac{1}{A}\left[G_{clean} - n_{bulk}\mu_{bulk}\right] \tag{2.56}$$

If atoms are adsorbed on the surface, then γ_s depends linearly on the chemical potential of the adsorbed species. Following equation 2.55 one obtains for a

certain adsorbate structure the expression

$$\gamma_s^{struc}(\mu_{ad}) = \frac{1}{A}\left[G_{struc} - n_{bulk}\mu_{bulk} - n_{ad}\mu_{ad}\right]. \tag{2.57}$$

When the free surface energies $\gamma_s^{clean}(\mu_{ad})$ and $\gamma_s^{struc}(\mu_{ad})$ intersect, the relation

$$G_{struc} - G_{clean} - n_{ad}\mu_{ad} = 0 \tag{2.58}$$

holds. Approximating the Gibbs energies G_x by the total free energies of DFT calculations and expressing $\mu_{ad} = \mu_{ad}^{ref} + \Delta\mu$ relative to the chemical potential of a reference phase of the adsorbed species, the result is:

$$\frac{1}{n_{ad}}E_{struc} - E_{clean} - n_{ad}\mu_{ad}^{ref} = \Delta\mu \tag{2.59}$$

Comparing the left hand side of equation 2.59 to equation 3.16 one realizes that it is the so-called adsorption energy for the considered surface structure. In other words, the intersection of γ_s of an arbitrary adsorbate structure with γ_s^{clean} is exactly at this energy, which corresponds to the chemical potential $\mu_{ad} = \mu_{ad}^{ref} + E_{ad}$.

If the model under consideration uses asymmetric slabs one has to refine equation 2.55 by adding the contribution $\gamma_{pure}^{unrelaxed}$ of the fixed bottom layers. In equation 2.60 the surface free energy of a clean and bulk-truncated (i.e. unrelaxed) slab is defined, in which G_{unrel} represents the Gibbs free energy, n_{bulk} the number of bulk particles and μ_{bulk} the bulk chemical potential. The prefactor $\frac{1}{2}$ is introduced since the correction is done only for the unrelaxed surface of the considered asymmetric slab. As a reminder, the definition of $\gamma_{pure}^{unrelaxed}$ is in principle the definition of the surface energy given in equation 3.12, but without including the relaxation energies of the surface. Combining these two equations would also allow to calculate the surface free energy for asymmetric slabs.

$$\gamma_{pure}^{unrelaxed} = \frac{1}{2}\frac{1}{A}\left(G_{unrel} - n_{bulk}\mu_{bulk}\right) \tag{2.60}$$

Adding the correction to the free energy γ_s finally results in equation 2.61, as it is demonstrated in reference [59]:

$$\gamma = \gamma_s - \gamma_{pure}^{unrelaxed} \tag{2.61}$$

This procedure allows the derivation of the stable surface terminations and surface structures under different surface conditions, see for example Franchini et al. [36] studying surface structures of MnO(111). These very general considerations can often be simplified when studying systems with few components only. First of all, the Gibbs free energies G_{struc} and G_{unrel} can be approximated

by the total energies of the calculated slabs. The chemical potentials μ_{bulk} and μ_i may be be expressed in terms of the other chemical potentials of the system. For example, if equilibrium of the surface with the underlying bulk is assumed, the total energy of the most stable bulk phase can be set equal to the chemical potential of this phase. For the adsorption studies in section 3.4.3 the equation 2.61 can be reformulated according to equation 2.62 in which E_{tot}^{slab} is the total energy of the calculated surface structure, $E_{unrelaxed}$ the total energy of the unrelaxed surface slab and E_W^{bulk} the total energy of the bulk phase, which is bcc tungsten in the present study. The expression n_{bulk}/A can be simplified to the number of layers n_L in the unrelaxed slab. Since only one species is adsorbed, the sum in equation 2.61 reduces to $\frac{n_{ad}}{A}\mu_{ad}$ in which $\frac{n_{ad}}{A}$ represents the number of adsorbed atoms per area A (i.e. the surface coverage x_{ad}). Finally, γ is a function dependent on the chemical potential of the adsorbed species μ_{ad}. It should be noted –as before– that μ_{ad} depends on $\{N_i\}$, T and p, leaving γ to be a Gibbs energy in the original sense. In most cases the chemical potential μ_{ad} is given relative to a known chemical potential of the adsorbed species, for example for gases relative to the chemical potential of its molecule or for metals relative to their stable bulk phases. Then, the relation $\mu_{ad} = \mu_{ref} + \Delta\mu$ is useful. Choosing a certain combination $(T, p, \{N_i\})$ allows then the determination of γ.

$$\gamma(\mu_{ad}) = \frac{E_{tot}^{slab}}{A} - \frac{n_{ad}}{A}\mu_{ad} - \left(\frac{1}{2A}E_{unrelaxed} + \frac{n_L E_W^{bulk}}{2}\right) \tag{2.62}$$

By closer inspection of $\gamma(\mu_{ad})$ it becomes obvious that the last two terms in brackets are constant, if the number of layers in the slab is kept fixed. Therefore, the remainder of equation 2.62 can be simplified for the needs of the CE in section 4.4. In equation 2.53 a coverage dependent "surface formation energy" E_{surf} was introduced, which shows the energy gain of an ordered structure with respect to the clean and the fully (1×1) covered surface. The energy E_{tot} in equation 2.53 is defined as before, the other energies E_{full} and E_{clean} are the total energies of the energies of a slab covered with a full monolayer and the clean surface respectively. Inserting the relation 2.53 into equation 2.62 results in the expression 2.63,

$$\gamma(\mu_{ad}) = E_{surf} - x_{ad}\left(\mu_{ad} + E_{tot}^{clean} - E_{tot}^{full}\right) + K, \prec \tag{2.63}$$

in which K is a constant term, defined as

$$K = E_{tot}^{clean} - \left(\frac{1}{2A}E_{unrelaxed} + \frac{n_L E_W^{bulk}}{2}\right). \tag{2.64}$$

Since $\gamma(\mu_{ad})$ is a linear function of μ_{ad}, it is allowed to shift μ_{ad} by the difference $E_{tot}^{clean} - E_{tot}^{full}$,

$$\mu' = \mu_{ad} + E_{tot}^{clean} - E_{tot}^{full}, \tag{2.65}$$

which finally results in

$$\gamma(\mu') = E_{surf} - x_{ad}\mu' + K. \tag{2.66}$$

For convenience the Legendre transform of γ with respect to the chemical potential μ' is made. The resulting Gibbs-like energy only depends on the adsorbate coverage x_{ad} (according to equation 2.67). Strictly speaking, the Legendre transformation derives $g(x_{ad})$ depending on (T, P, N_W, μ_{ad}). But since μ' is eliminated, the free energy $g(x_{ad})$ depends only implicitly on μ', namely via x_{ad},

$$g(x_{ad}) = E_{surf}(x_{ad}) + K. \tag{2.67}$$

This result implies that for a given surface structure with coverage x_{ad} only the energy E_{surf} needs to be determined since all other quantities are constant. It is further noted, that in Monte Carlo simulations (e.g. in the canonical ensemble with a Metropolis algorithm) only energy differences of the quantities $g(x_{ad})$ are important, and one therefore arrives at the very useful formulation

$$g^2 - g^1 = E_{surf}^2 - E_{surf}^1, \tag{2.68}$$

since the constant term K cancels out.

2.5 Implementation of the CE

After presenting an overview of the CE formalism, the practical implementation will be discussed. In the present work, the CE as implemented in the UNCLE code [58] is used. At this point, the permission for using UNCLE given by Stefan Müller is gratefully acknowledged. For this work, a CE for enthalpies of formation (according to equation 2.33) or related energies is done. That is why in the following paragraphs only this case is discussed in detail. In section 2.5.1 the determination of the interaction energies for a certain figure set is demonstrated. Section 2.5.2 shows then the optimization of the figure selection by use of a genetic algorithm.

2.5.1 Determination of the Interaction Energies by Fitting

As pointed out in section 2.2.1 the CE formalism is exact, in principle. Knowledge of the complete set of interaction energies $\{J_F\}$ in equation 2.33 would then allow calculation of the enthalpy of formation of an arbitrary configuration σ. The

primary goal, when constructing a CE, is the determination of these interaction energies. If the interaction energies are known once, any other desired quantity, which depends on the energy of formation (or the quantity for which the CE was constructed for) can be calculated. For example, the interaction energies can be used in Monte Carlo simulations in order to get access to the temperature dependent thermodynamical properties such as the specific heat, the configurational entropy, and so on. Therefore, by this combination of CE and Monte Carlo techniques temperature dependent phase stabilities, i.e. a phase diagram, can be derived. Of course, the huge number of possible interactions which appear in equation 2.33 can never be handled in a practical way. That is why the sum has to be truncated, limiting the number of interactions to a reasonably small set, which can be treated computationally. On the one hand, reducing the sum introduces some error, since a large number of the interaction energies are not considered when calculating ΔH_f. On the other hand, the most important interaction energies are in the range of a few Å. For example in a face centered cubic lattice up to the 6th nearest neighbor (corresponding to a distance of $\sqrt{3}$ times the lattice constant ≈ 6 Å) 149 different triplet figures can be found. For figures with a higher number of vertices, the possible number of such figures for such a range distance increases strongly. Assuming that the underlying atomic interactions are not longer-ranged than this distance and adding smaller figures with four, five and six points, figure sets of some hundred can be defined. Under these assumptions the sum in equation 2.33 is reduced to a size that can be used for practical purposes. It can be even further reduced, as learned from experience. A converged CE needs not more than 40 to 50 figures to describe the energetics of a system with a reasonable precision . A detailed discussion on how to select the correct figures by making use of a genetic algorithm from the reduced pool of some hundred figures is given in section 2.5.2. In a next step, the determination of the interaction energies has to be done by fitting the enthalpy of formations of a suitably large number of structures (with chosen structures or unit cells) to the CE Hamiltonian. For each of the structures, a DFT calculation is made in which the crystal structure and atomic positions are fully relaxed. The final total energy is used to calculate the enthalpy of formation according to equation 2.32. The simplest way of fitting the interaction energies is the direct inversion method according to Conolly and Williams [16] given in equation 2.69, in which N_σ input structures are fitted to N_J interaction energies:

$$\sum_{N_\sigma} w_\sigma \left(\Delta H_f^{DFT}(\sigma) - N \sum_{F=1}^{N_J} \overline{\Pi}_F(\sigma) D_F J_F \right)^2 = min \tag{2.69}$$

For a mathematically proper fitting, the relation

$$N_J \leq N_\sigma \tag{2.70}$$

must hold. This is another restriction to the number of terms in equation 2.33. In fact, the computational costs for getting accurate enthalpies of formation can be quite large. Compared to the effort of running a CE, which requires some hours of a single processor computing, DFT calculations can take up to some days (or even longer for more complex cases). In other words, the bottleneck for using the CE consists in the DFT calculations which provide the input energies. Extending equation 2.69 by a damping term $\sum_F f_F J_F$ according to Garbulsky and Ceder [39], describes the procedure as used in the present work,

$$\sum_{N_\sigma} w_\sigma \left(\Delta H_f^{DFT}(\sigma) - \sum_F \overline{\Pi}_F(\sigma) D_F J_F \right)^2 + \sum_F f_F J_F = min. \tag{2.71}$$

For each structure a weight w_σ can be defined to denote its importance in the fit. For the present purpose equally weighted structures were used i.e. $w_\sigma = 1 \quad \forall \quad \sigma$. Also the importance of the geometrically different figures can be changed by the damping term f_F. If needed, one can ensure that greater figures are of less importance and that their respective interaction energies are therefore damped (.e.g. similar to a $1/r$ decay of an interaction potential). The damping term may be chosen differently for pairs and higher many body figures,

$$f_F = \begin{cases} c_1 r_F^{\lambda_1} & \text{Pairs} \\ c_2 r_F^{\lambda_2} & \text{Many-body.} \end{cases} \tag{2.72}$$

In equation 2.72 the parameters $c_1, c_2, \lambda_1, \lambda_2$ are adjusted for defining the wanted damping; the distance r_F denotes the mean size of the figure. Additionally, three linear inequalities are given as constraints (equations 2.73 to 2.75). The enthalpy of formation from the CE is constrained to a defined deviation δ_1 from the DFT calculated energies (equation 2.73 and figure 2.8 (a)). Also the energetical distance to the ground state line ΔE_2^{CE} is constrained to ΔE_2^{DFT} by an error in energy, δ_2 (equation 2.74 and figure 2.8 (a)). In analogy to that at concentrations without a ground state the deviation of the enthalpy of formation ΔE_3^{CE} to the energetically lowest structure is constrained to ΔE_3^{DFT} by the deviation δ_3 (equation 2.75 and figure 2.8 (b)).

$$\Delta H_f^{DFT}(\sigma) - \delta_1 < \quad \Delta H_f^{CE}(\sigma) \quad < \Delta H_f^{DFT}(\sigma) + \delta_1 \tag{2.73}$$

$$\Delta E_2^{DFT}(\sigma) - \delta_2 < \quad \Delta E_2^{CE}(\sigma) \quad < \Delta E_2^{DFT}(\sigma) + \delta_2 \tag{2.74}$$

$$\Delta E_3^{DFT}(\sigma) - \delta_3 < \quad \Delta E_3^{CE}(\sigma) \quad < \Delta E_3^{DFT}(\sigma) + \delta_3 \tag{2.75}$$

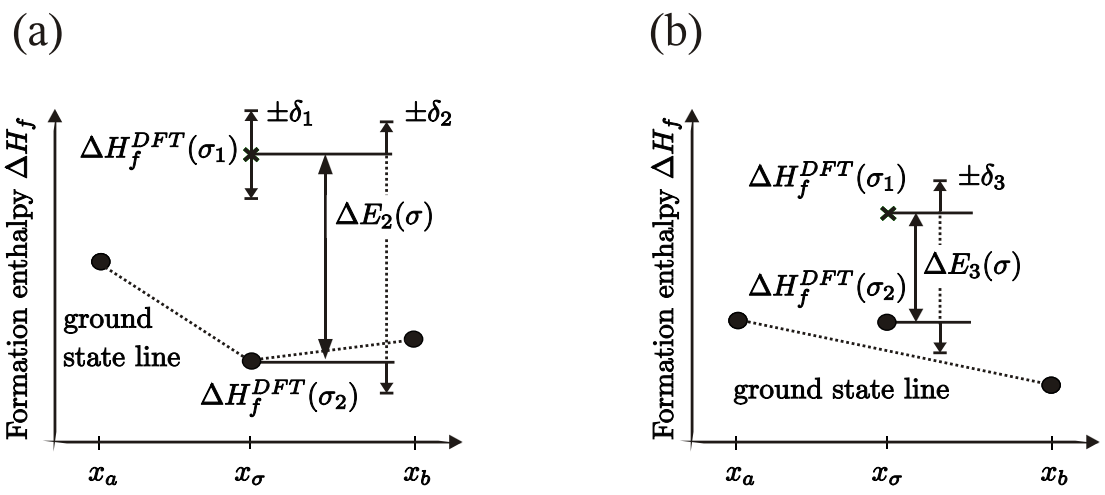

Figure 2.8: Sketch of the linear constraints from equation 2.73 to 2.75 for fitting the interaction energies. The deviation δ_1 constrains the absolute error for the fit of the enthalpy of formation. The deviations δ_2 and δ_3 constrain the distance of the enthalpies derived by the CE to the ground state line or the energetically lowest structure at the same concentration, respectively.

The three errors δ_i are chosen in such a way that the energetically lowest structures are fitted as accurate as possible, whereas the energetically less favourable structures are allowed to have larger errors. In the UNCLE code the errors δ_i are chosen according to equation 2.76. There, an exponential energy dependence is given that can be adjusted by the factor kT. The principle accuracy is given by δ_i^0:

$$\delta_i = \delta_i^0 \exp\left(-\frac{\Delta E_3^{DFT}}{kT}\right) \tag{2.76}$$

Overall, the fitting procedure results in a quadratic minimization problem with linear inequalities with constraints which has to be solved numerically e.g. according to Goldfarb and Idnani [40]. First the quadratic equation 2.71 is solved approximately without constraints. By and by adding the constraints of equations 2.73 to 2.75 adjusts the solution until the final solution of the whole system is found.

For starting a CE in a bulk system, one starts with DFT calculations of a set of structures with high symmetry which consist of layered structures along low index crystal directions, such as [100],[111] and [110] (see figure 2.9). An overview for body and face centered cubic lattices is given for example in reference [61]. The DFT total energies of such structures are then used for a fit to derive the interactions $\{J_F\}$ according to equations 2.71 to 2.75, as described above. The

configurational independent interactions are then used to calculate the enthalpy of formations for a huge configuration space according to equation 2.33, and the ground state line (see discussion in section 2.4.1) is constructed. For example, for the configuration space at the beginning of the CE procedure, all structures with unit cells up to eight atoms are considered and extended to a final set with up to 16 atoms (or more, if necessary). If the CE finds ground state structures in the considered configuration space which were not calculated by DFT, then DFT calculations are made for these missing structures. With the additional set of structures again a determination of the interaction energies $\{J_F\}$ is done. The CE-DFT cycle is repeated until the ground state line is stable, i.e. CE only predicts structures to be stable, which were also predicted to be stable by DFT. This self-consistent procedure ensures a high probability that no important structures are missed for the CE. It is also a tool for finding the true ground states, which for solid phases could be a rather challenging task. For surfaces, the workflow is in principle as sketched in figure 2.9 with the difference that at first the bulk CE has to be done, which is then used as basis for determining the differences of interaction energies $\delta J_F(\vec{R})$. Since only N_J figures can be chosen from the fit procedures (see equation 2.70) the interaction energies are always associated with approximations[1]. When choosing the figures it is very difficult to select the energetically important ones, since they are unknown a priori. For optimizing the figure selection a genetic algorithm is used which is explained in more detail in section 2.5.2.

2.5.2 Optimized Figure Selection with Genetic Algorithms

As mentioned in section 2.5.1, the selection of figures is an important step for the determination of the interaction energies. To judge the quality of a certain figure selection it is necessary to understand which figure sets give a good description of the energetics of a system. Most important is the accuracy of the fit when predicting structures that were not included in the fit. A quantitative measure of this predictive power is the so-called "cross validation score" (S_{CV}) as defined in equation 2.77.

$$S_{CV} = \sqrt{\frac{1}{nN_{pred}} \sum_{n} \sum_{N_{pred}} \left(\Delta H_f^{CE}(\sigma) - \Delta H_f^{DFT}(\sigma)\right)^2} \tag{2.77}$$

From all N_σ calculated enthalpy of formations $\{\Delta H_f^{DFT}\}$ a set of N_{pred} structures is left out and the fit for determining the interaction energies $\{J_F\}$ is done

[1]Since with the fitting procedures the DFT energies are reproduced, the missing interaction energies of the left out figures are included in the actually used ones

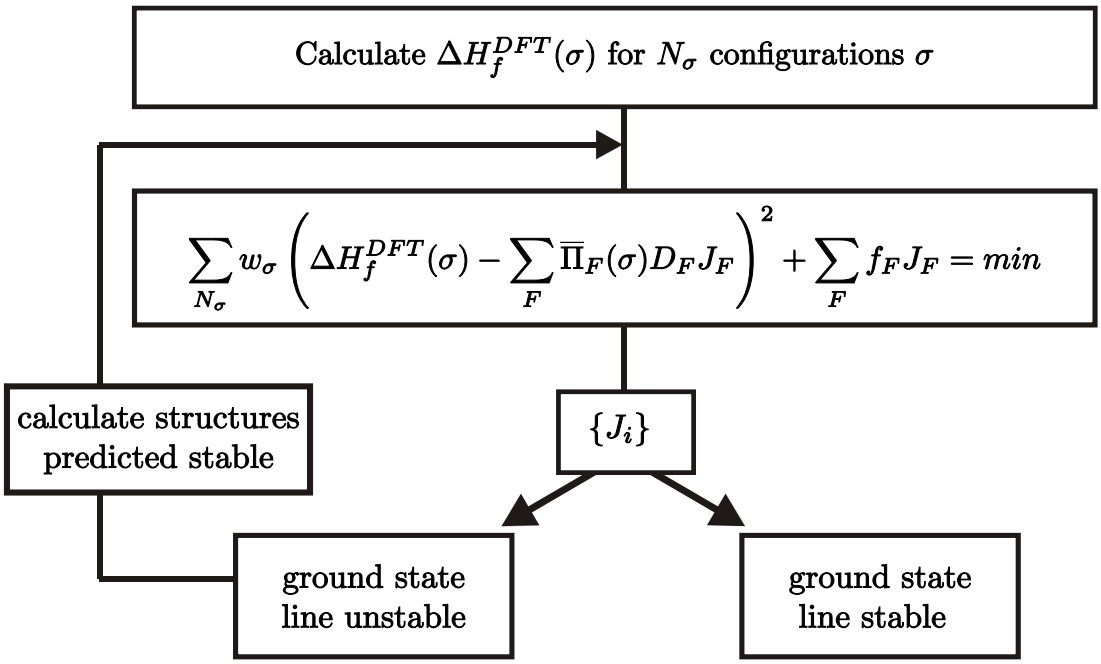

Figure 2.9: Sketch of the workflow of a standard CE. Starting with N_σ DFT-calculated enthalpy of formations, the N_J interaction energies $\{J_F\}$ are determined by fitting to the DFT results. These are then used for the ground state search. In case of an unstable ground state line, the new structures, which are predicted by CE to be stable, are calculated by DFT, and a fit is done again with the now larger set of data. This CE-DFT cycle is repeated until the ground state line is stable.

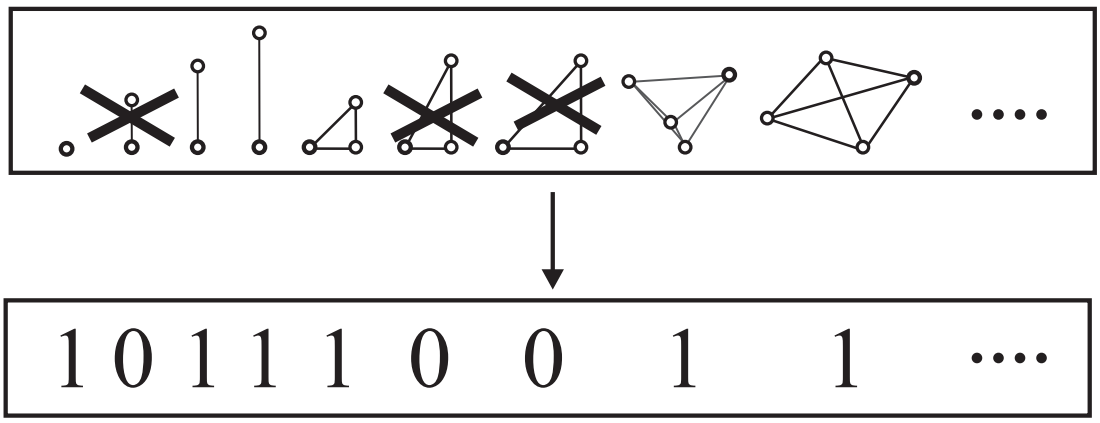

Figure 2.10: Binary representation of an "individual" for the genetic algorithm. Used figures are associated with "1", unused ones with "0".

with the remaining $N_\sigma - N_{pred}$. The enthalpies of formation $\Delta H_f^{CE}(\sigma_j)$ of the left structures are then predicted with the fitted interactions $\{J_F\}$ and finally compared to the DFT value $\Delta H_f^{DFT}(\sigma_j)$. This procedure is repeated for n randomly created subsets of size N_{pred}. For these subsets choices from all structures except the pure phases corresponding $x = 0$ and $x = 1$ are made. The effective interactions finally are averaged over all the n fits by

$$J_F = \frac{1}{n} \sum_{i=1}^{n} J_F(i). \tag{2.78}$$

Thus, the cross validation score is not a measure for the accuracy of the fit itself, but a measure for the accuracy in *predicting* properties for unknown structures. As a second quality criterion –besides a sufficiently small score S_{CV}– a proper figure selection has to reproduce the ground state line. To find a suitable figure selection out of the huge possible selection space genetic algorithms are used. The prototype for this algorithm can be found in nature, since it utilizes procedures connected to the genetic reproduction of a specific species for solving problems. Genetic algorithms are particularly useful for optimizing solutions of non-continuous parameter spaces [19]. In practice, a figure set is represented by a binary coding (see figure 2.10). In the formulation of genetic algorithms such a set is denoted as "individual" [19]. Figures which are actually used are associated with the number "1", unused ones with the number "0". An implementation of a genetic algorithm for a CE was first done by Blum et al. [7].

At the beginning a set of some ten individuals is created randomly and checked about their "fitness" by calculating the score S_{CV} (figure 2.11). Those individuals with the best cross validation score are then used to generate new individuals,

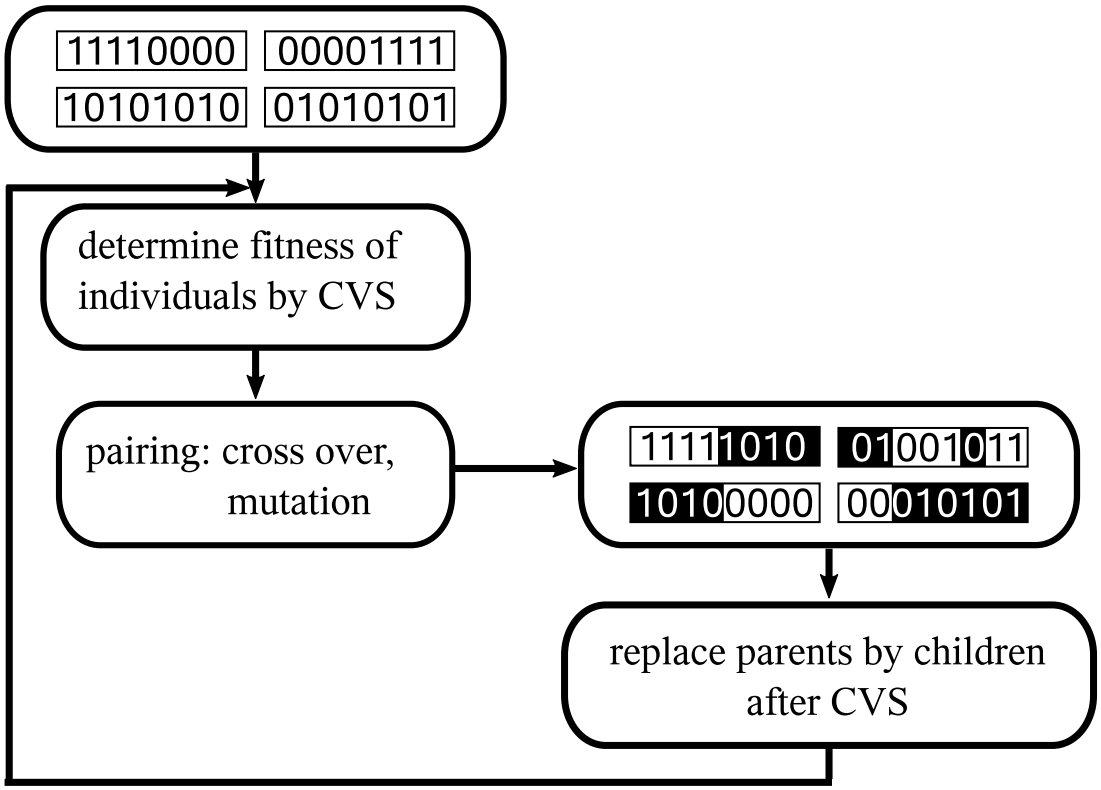

Figure 2.11: Workflow diagram of the genetic algorithm. Initially a population of some tens of individuals is created. The fitness in terms of S_{CV} of these individuals is calculated according to equation 2.77. Then, new "children" by pairing and mutation operations are created. Again, the score S_{CV} for the children is calculated. Replacing some less fit parents by fitter children (i.e. the score of the children is lower S_{CV} than the parents) the next generation is produced. For more details, see text.

which are called children. In doing so, figures between two individuals are exchanged ("cross over") and figures are added or removed randomly from the figure sets. This is a so-called "mutation". For each of the children the score S_{CV} is calculated and then some of the older individuals ("parents") with a worse fitness are replaced by fitter children. This is one generation step. Proceeding to the next generation gives a changed parent population which again produces children and so on.

The described procedure gradually improves the score S_{CV}. Finally all individuals are very similar (i.e. consisting of very similar or even equal figure selections and having similar S_{CV}) indicating convergence for the current optimization run. However, it is possible that the individual with the smallest score S_{CV} is only a local minimum. In order to find the global minimum (i.e. best figure set with

the lowest S_{CV}), after a finished run another one (or several others) is started. Again, the individuals are created randomly at the beginning and optimization is done as described before. If an individual has the same figure selection given by a previously finished genetic algorithm run, this particular individual is expelled and replaced by another one (This is called a "lock out" situation). By doing so, each run leads to different local minima of figure sets. After a series of runs one can select the figure set with the lowest score S_{CV} of all runs.

2.6 Monte Carlo Simulations

The cluster expansion as described in 2.5 aims at a properly chosen set of interaction energies. If these are known, they can be used in Monte Carlo (MC) simulations to get access to temperature dependent thermodynamical properties, such as the specific heat and the configurational entropy. A comprehensive introduction to this simulation technique can be found for example in references [37] and [5]. In general, a Markov Chain of consecutive configurations is constructed. It obeys the detailed balance criterion of equation 2.79 meaning that the flow $K(o \rightarrow n)$ of configurations going from the old state ("o") to a new state ("n") equals the reversed flow from n to o, according to

$$K(o \rightarrow n) = K(n \rightarrow o), \tag{2.79}$$

in which $K(o \rightarrow n)$ is defined in equation 2.80,

$$K(o \rightarrow n) = N(o) \cdot \alpha(o \rightarrow n) \cdot acc(o \rightarrow n). \tag{2.80}$$

In equation 2.80 $N(o)$ denotes the probability of being in configuration o, whereas $\alpha(o \rightarrow n)$ is the probability of generating configuration n, and finally $acc(o \rightarrow n)$ is the probability of accepting configuration n. Restricting equation 2.79 to a canonical ensemble means $\alpha(o \rightarrow n) = \alpha(n \rightarrow o)$, since n/o is generated by site exchange of two atoms. The probability of finding a certain structure is given by the Boltzmann term $N(i) = \exp\{-\beta U(i)\}$, for which $U(i)$ is the energy of state i, $\beta = 1/kT$ and $i = \{o, n\}$, reducing equation 2.79 to

$$N(o) \cdot acc(o \rightarrow n) = N(n) \cdot acc(n \rightarrow o). \tag{2.81}$$

The acceptance probability of keeping the change of configuration is then given by,

$$\frac{acc(o \rightarrow n)}{acc(n \rightarrow o)} = \exp\{-\beta\,[U(n) - U(o)]\}\,. \tag{2.82}$$

Any implementation of a MC simulation must fulfill equation 2.82 which in principle can be realized by different computational conditions. The most common

scheme –as also for this work– is the algorithm according to Metropolis et al. [65] defined by equation 2.83, in which $W(o \rightarrow n)$ is the probability of accepting the move from o to n and the energy gain is denoted by $\Delta U = U(n) - U(o)$,

$$W(o \rightarrow n) = \begin{cases} 1 & \Delta U \leq 0 \\ exp(-\beta \Delta U) & \Delta U > 0. \end{cases} \tag{2.83}$$

3

Physical Properties of Pure Elements Used in This Study

Before starting calculations of surface properties, it is mandatory to investigate the basic equilibrium bulk properties of the considered solid material, such as the lattice parameters, volumes, atomic structure and elastic properties (e.g. the bulk modulus). By such a procedure, one can critically check the quality of the chosen potential, correlation functionals, basis sizes and other numerical parameters. In this section, the elemental bulk phases of tungsten (W) and indium (In) are discussed. For the surface studies (see following sections) tungsten is of importance, because the *W(110)* surface is the substrate on which the adsorption studies are made. Surface properties of metallic indium are of interest to analyze the adsorption properties of indium on *W(110)*.

3.1 Bulk Properties of Tungsten

For a precise calculation of the lattice constant the total energy as a function of volume and other geometrical parameters has to be minimized. For tungsten, this has to be done for the body centered cubic ground state structure. Minimization of the unit cell volume as sketched in figure 3.1 was made by using a basis size corresponding to an energy cutoff of 400 eV, and a 15x15x15 k-point set chosen according to the construction of Monkhorst and Pack [68]. For the GGA-PBE exchange correlation functional according to reference [76] the minimized configuration with $V_{min} = 16.23$ Å^3 and a lattice constant of $a_W = 3.189$ Å at an energy minimum of the total energy $E_{min}^{PBE} = -12.96$ eV is found. The so-called total energy is rather a pseudo-cohesive energy, because it refers to the configuration of atomic states, which were used for the construction of the pseudopotential.

Compared to the experimental value of 3.165 Å of reference [80], the present

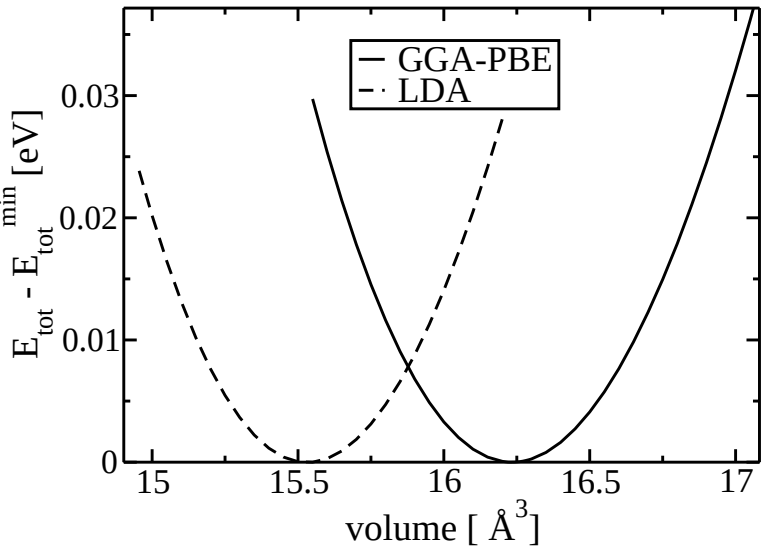

Figure 3.1: Normalized total energy $E_{tot} - E_{tot}^{min}$ versus unit cell volume of bcc tungsten. The exchange correlation functional is either GGA-PBE or LDA. In case of LDA, the volume per atom is smaller than found in experiment, for GGA-PBE it is larger that in experiment. For details see text.

GGA-PBE calculation is ≈ 0.8 % larger. Choosing an LDA exchange correlation functional instead, the overbinding of LDA shrinks the equilibrium volume to $V_{min} = 15.55$ Å^3 corresponding to a lattice constant of $a_W = 3.145$ for a minimum energy of $E_{min}^{LDA} = -14.05$ eV. Now, the lattice constant is ≈ 0.6 % smaller than the experimental value. Summarizing, GGA as well as LDA are of the same quality, at least concerning the equilibrium volume. This is typical for 5d elements. However, if elastic properties are calculated or surface energetics, than GGA is superior, and therefore the GGA approach of PBE was chosen for studying adsorption on the *W(110)* surface.

A very sensitive quantity directly related to change of the total energy with respect to the volume is the equilibrium bulk modulus,

$$B_0 = \frac{1}{V}\frac{\partial^2 E_{tot}^{min}}{\partial V^2}. \tag{3.1}$$

In its most simple derivation assuming, that the total energy is a quadratic function of volume, it is given as the curvature of the energy-volume curve at the equilibrium volume V_{min}, shown in equation 3.1. Using the data of figure 3.1 for fitting to a higher order polynom and calculating B_0 according to equation 3.2, $B_0^{PBE} = 307$ GPa and $B_0^{LDA} = 333$ GPa for the different exchange correlation functionals are obtained. The experimental value as reported by Featherstone

and Neighours [31] of $B_0^{exp} = 314$ GPa is rather close to the GGA-PBE result, whereas LDA due to its overbinding failure yields a value for B_0, which is larger by ≈ 9 %.

$$E(V) = E_0(V_0) + \frac{1}{2} B_0 \frac{(V - V_{min})^2}{V_{min}} \tag{3.2}$$

A more accurate calculation of the bulk modulus is available by the Murnaghan equation of state (reference [71] and equation 3.3). Such more sophisticated calculations for tungsten hardly change the results when compared to equation 3.2: $B_{Murn}^{PBE} = 306$ GPa and $B_{Murn}^{LDA} = 336$ GPa. Table 3.1 summarizes the discussed data.

$$E(V) = E_0(V_0) + \frac{B_{Murn} V}{B'_{Murn}(B'_{Murn} - 1)} \left[B'_{Murn} \left(1 - \frac{V_0}{V} \right) + \left(\frac{V_0}{V} \right)^{B'_{Murn}} \right] \tag{3.3}$$

The most detailed information about elastic properties is given by the elastic constants. An introduction to this topic can be found in the book of Nye [73]. For cubic tungsten the three elastic constants c_{11}, c_{12} and c_{44} –due to the symmetry of the lattice– need to be calculated. The bulk modulus is then the linear combination $B = (c_{11} - 2c_{12})/3$ (For the calculation of B hydrostatic pressure is assumed. But since c_{44} represents a distortion, it does not enter the calculation of B).

3.2 Bulk Properties of Indium

For metallic indium the bulk ground state is of some interest in this work, since indium will be used as an adsorbate in chapter 5. Indium crystallizes in a face centered tetragonal (fct) structure. The measured lattice parameters are $a_{In} = 4.60$ Å with a ratio of $c/a = 1.08$ [80]. It is noticeable, that the fct structure can also be referred to as an body centered tetragonal one (bct). The lattice parameters are then derived as $a_{bct} = 1/2\sqrt{2} a_{fct} = 3.25$ Å with $(c/a)_{bct} = \sqrt{2}(c/a)_{fct} = 1.53$. For calculating the minimum total energy for fct indium optimization with respect to two parameters has to be done. Figure 3.2 presents the DFT calculations at different fixed volumes. For each volume the shape of the unit cell was allowed to relax. As for tungsten, the LDA functional overestimates the binding and gives a significant smaller volume than the PBE functional, namely $V_{min}^{LDA} = 24.60$ Å^3 with a total (or pseudo-cohesive) energy of $E_{tot}^{min} = -3.20$ eV. For the PBE calculation the volume amounts to $V_{min}^{PBE} = 27.50$ Å^3 and the equilibrium total

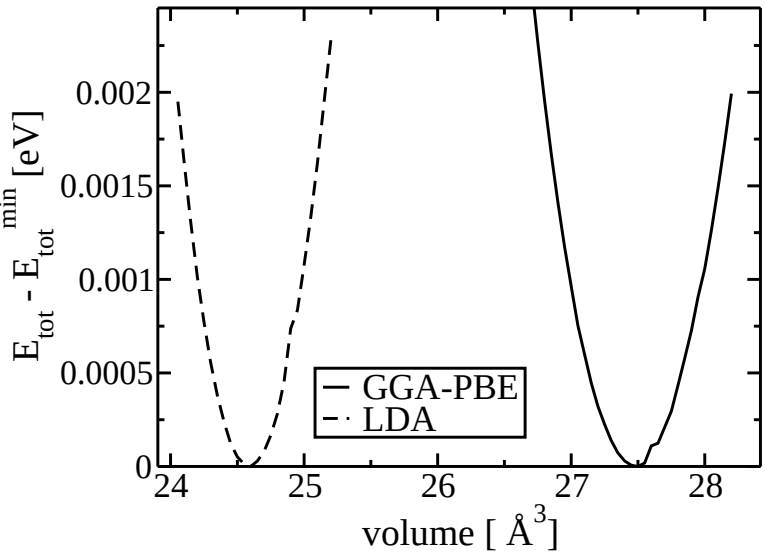

Figure 3.2: Normalized total energy $E_{tot} - E_{tot}^{min}$ versus unit cell volume of fct indium. The exchange correlation functional is either GGA-PBE or LDA. In case of LDA, the unit cell volume is smaller than found by experiment, for GGA-PBE it is larger than experiment. For details see text.

energy to $E_{tot}^{min} = -2.73$. Correspondingly, the lattice parameters for the GGA-PBE calculations are $a_{In}^{PBE} = 4.695$ Å and $(c/a)_{fct}^{PBE} = 1.06$, whereas the LDA results $a_{In}^{LDA} = 4.513$ Å and $(c/a)_{fct}^{LDA} = 1.07$. In both cases, the c/a ratio is slightly smaller than the experimental value, and the lattice parameter a is approximately 2 % smaller in the case of the LDA and 2% larger in the case of the PBE calculation.

The elastic properties of indium are quite different to that of tungsten. The bulk modulus can be calculated according to equation 3.4 using the elastic constants of reference [14]. It amounts to the rather small value of 46.4 GPa at 4.2 K, clearly characterizing indium as a rather soft material. Considering the DFT data and calculating again B_0 according to equations 3.2 and 3.3 yields values of 36.0 and 35.3 GPa for GGA-PBE, and 56.1 and 51.2 GPa for LDA. A summary of all the data discussed in this section can be found in table 3.1.

$$B_{fct} = \frac{2}{9}\left(c_{11} + c_{12} + 2c_{13} + \frac{c_{33}}{2}\right) \tag{3.4}$$

Table 3.1: Summary of the ground state properties of tungsten and indium. The bulk modulus B_0 was calculated via equation 3.2, modulus B_{Murn} by using equation 3.3, respectively. Details are discussed in the text.

	W			*In*		
	LDA	PBE	EXP	LDA	PBE	EXP
a [Å]	3.145	3.189	3.165 [a]	4.513	4.695	4.60[a]
c/a	-	-	-	1.07	1.06	1.08[a]
V_{min} [Å^3]	15.6	16.2	15.9	24.6	27.5	26.3
E_{tot}^{min} [eV]	-14.05	-12.96	-	-3.20	-2.73	-
B_0 [GPa]	333	315	314 [b]	56.1	36.0	46.4 [c]
B_{Murn} [GPa]	336	304		51.2	35.3	

[a] reference [80]
[b] reference [31]
[c] reference [14]

3.3 Oxygen

The second adsorbate which will be studied in chapter 4 is oxygen. Therefore, this section deals with a characterization of molecular oxygen, since it will be used as reference for adsorption energies and vibrational properties. For the DFT calculations only the GGA-PBE functional was applied, since it is well known that LDA fails rather badly for molecules (and even worse, for atoms). Figure 3.3 presents the normalized DFT total energy and the corresponding forces versus the interatomic spacing of the O_2 molecule. Spin polarization was allowed which resulted in a ferromagnetic coupling of both O atoms with a magnetic moment of 0.8 μ_B per atom, yielding a total energy of $E_{tot}^{min} = -9.86$ eV with an interatomic equilibrium spacing of $d_{min} = 1.23$ Å. Besides the equilibrium parameters also the vibrational properties are of interest. The forces acting upon the molecules as extracted from the DFT calculations are shown in figure 3.3. The force constant D as defined in equation 3.5 is the slope of the shown curve. Calculating the vibrational frequency ν according to equation 3.6 and using μ_{red} for the reduced mass of the oxygen molecule results in a frequency of 46.6 THz or a wavenumber of 1554 cm^{-1}. This in good agreement with experimental data of 1549 cm^{-1} reported in reference [18]. Using the derived value for ν to calculate the zero point energy of the harmonic oscillator according to ZPE $= h\nu\frac{1}{2}$ gives a value of ZPE=96 meV which is in excellent agreement to the calculated value of 95 meV from Zhang et al. [115].

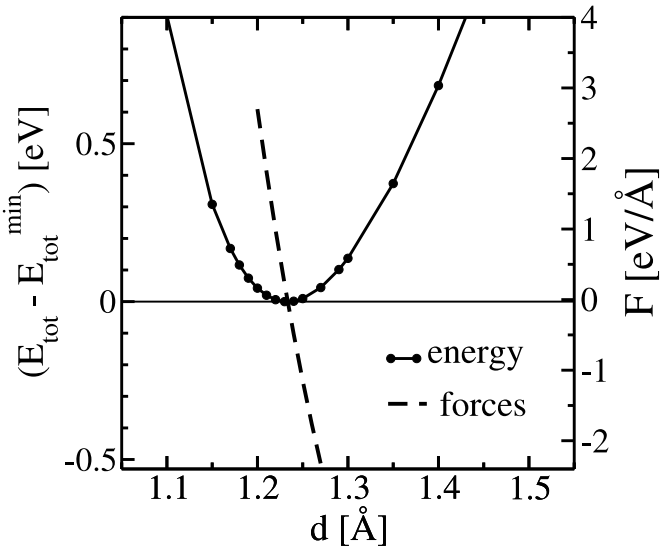

Figure 3.3: Normalized total energy and the corresponding forces for an oxygen molecule depending on the interatomic spacing of the molecule. The minimum *O-O* distance is $d_{min} = 1.23$ Å at which the total energy is $E_{tot}^{min} = -9.86$ eV. For details see text.

$$D = \frac{\Delta F}{\Delta x} = \frac{-0.7107 \mathrm{eV/\AA}}{0.01 \mathrm{\AA}} = -11.38 \frac{\mathrm{N}}{\mathrm{cm}} \tag{3.5}$$

$$\nu = \frac{1}{2\pi}\sqrt{\frac{D}{\mu_{red}}} = \frac{1}{2\pi}\sqrt{\frac{2D}{m_O}} = 46.6 \mathrm{THz} \tag{3.6}$$

3.4 Surface Properties of Metals

In this section surface properties of pure metals are discussed. At the beginning, the simple bond breaking model is applied for the estimation of the surface energies of tungsten and indium in section 3.4.1. In a next step, the structural details of the low indexed tungsten surfaces are studied in section 3.4.2 and finally in the sections 3.4.3 and 3.4.4 the details of the clean *W(110)* surface are discussed.

3.4.1 Bond Breaking Model for Surface Energies

A simple model for the description of surface energies was given by Methfessel et al. [63]. A bulk material with coordination number C_B consisting of N atoms

has $NC_B/2$ bonds. Assuming that the bulk crystal is only built up by nearest neighbor bonds of bond energy b the cohesive energy per atom is then given by $E_{coh} = C_B b/2$. In a first step for the estimation of the surface energy σ a linear dependence of the bond strength with respect to coordination number is suggested:

$$\sigma = \frac{1}{2}(C_B - C_S)b = \frac{C_B - C_S}{C_B} E_{coh} \tag{3.7}$$

In order to learn if equation 3.7 is valid for different metals the total energy $E(C)$ with respect to the coordination number C has to be studied. Using DFT, different atomic configurations with specific coordination numbers were calculated. Within each configuration each atom has the same number of bonds with each bond length kept fixed at the bulk nearest neighbor distance of the considered metal. Table 3.2 shows a list of the calculated configurations and their coordination numbers. Reference [63] provides this relation for the 4d transition metals from ytterbium to silver. The authors report that instead of using the simple model of equation 3.7 rather a square root dependence (equation 3.8) should be used, since using the energy dependence according to equation 3.9 gives better agreement to the DFT calculated data than a simple linear model.

$$\sigma' = \frac{\sqrt{C_B} - \sqrt{C_S}}{\sqrt{C_B}} E_{coh} \tag{3.8}$$

$$E(C) = E_0 - A\sqrt{C} + BC \tag{3.9}$$

In figure 3.4 the total energy versus the coordination number for tungsten and indium is plotted. Both studied elements show also a square root dependence according to equation 3.9, and therefore it is concluded, that equation 3.8 can also be applied for estimating the surface energies for these elements.

Following the discussion from above, equation 3.8 was applied to tungsten and indium. The values were derived from cohesive energies $E^W_{coh} = 8.33$ eV/atom and $E^{In}_{coh} = 2.36$ eV/atom, for tungsten and indium respectively. Table 3.3 lists the surface energies σ and σ' according to equations 3.7 and 3.8. These values are compared to DFT surface energies σ_{DFT} calculated within a symmetric repeated slab model consisting of 13 layers. For both metals, the estimation σ is always larger than the value of σ_{DFT}. The agreement between σ' and σ_{DFT} for tungsten is rather good. This can also be seen in figure 3.5 which analyzes the dependency of the surface energy on the coordination number. In case of indium, however, only for the *(111)* surface good agreement is found. For the *(110)* and *(100)* surfaces the values of σ' are also larger than the DFT values. This is due to

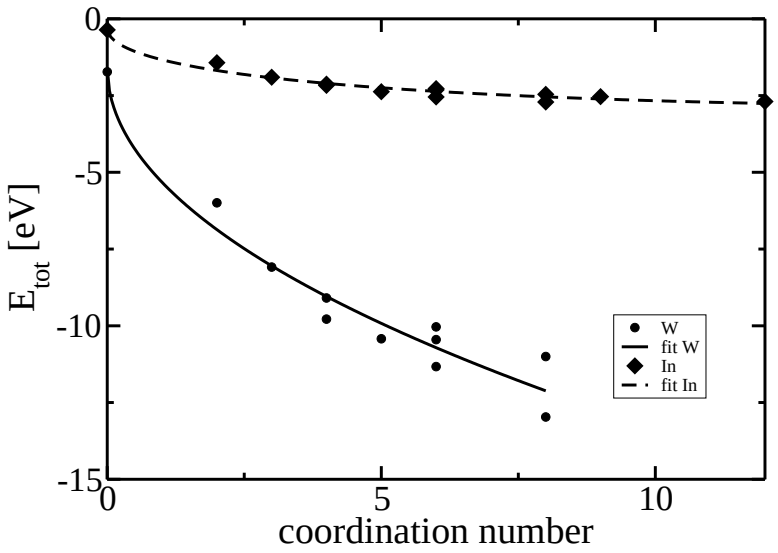

Figure 3.4: Dependency of the total energy of indium and tungsten on the coordination number. The dependency is not linear but shows rather a square root dependence.

Table 3.2: Calculated configurations for the determination of the bond strength of simple metals. For each structure the nearest neighbor distance was chosen to be that of the most stable bulk configuration.

	C		C
atom	0	simple cubic	6
line	2	fcc(110) bilayer	6
graphite layer	3	fcc(100) bilayer	8
diamond bulk	4	bcc bulk	8
square monolayer	4	fcc(111) bilayer	9
square bilayer	5	fcc bulk	12
hexagonal monol.	6		

Table 3.3: Surface energies σ, σ' and σ_{DFT} for tungsten and indium in eV/atom. The values of σ and σ' were calculated according to equations 3.7 and 3.8 using $E_{coh}^{W} = 8.33$ eV/atom and $E_{coh}^{In} = 2.36$ eV/atom.

	C_B	C_S	σ	σ'	σ_{DFT}
W(100)	8	4	4.16	2.44	2.61
W(110)	8	6	2.08	1.12	1.50
W(111)	8	2	6.24	4.16	3.94
In(100)	12	8	0.79	0.43	0.36
In(110)	12	6	1.18	0.69	0.37
In(111)	12	9	0.59	0.32	0.32

the softness of indium, for which the simple bond-breaking model is rather ill-designed. In general, the surface energies of tungsten are larger by a factor of ≈ 10. This is also reflected by the large difference of the cohesive energies and melting points.

3.4.2 Structural Details of the Surfaces

After the simple considerations of surface energies in section 3.4.1 now the computational setups for different surfaces of tungsten are discussed. A correct surface model should of course reproduce the known experimental results of surface layer relaxations and surface energies. Not available from experiment are the relaxation energies, since this quantity cannot be measured. For the construction of surfaces two possible setups are possible. Depending on the needs and goals of the study symmetric or asymmetric slabs can be constructed. Figure 3.6 (a) shows the setup for a symmetric surface slab. The bulk W atoms (in black color) are arranged in the bcc bulk structure of W. The surface W atoms (drawn in white) are arranged symmetrically with respect to the bulk bcc atoms. In the DFT calculations both surface regions are then relaxed, whereas the positions of the bulk atoms are kept fixed. For an asymmetric slab as sketched in figure 3.6 (b) only at one side of the bulk W atoms surface atoms are added. Consequently only one surface that is in contact with vacuum is relaxed and the bulk part is kept fixed.

In order to find the optimal size of the super cell for the surface calculations the slab's thickness, i.e. number of layers, and the size of the vacuum needs to be varied. Since a periodic slab approach for the DFT calculations is used, the minimum size of vacuum has to be chosen in such a way that no interaction of

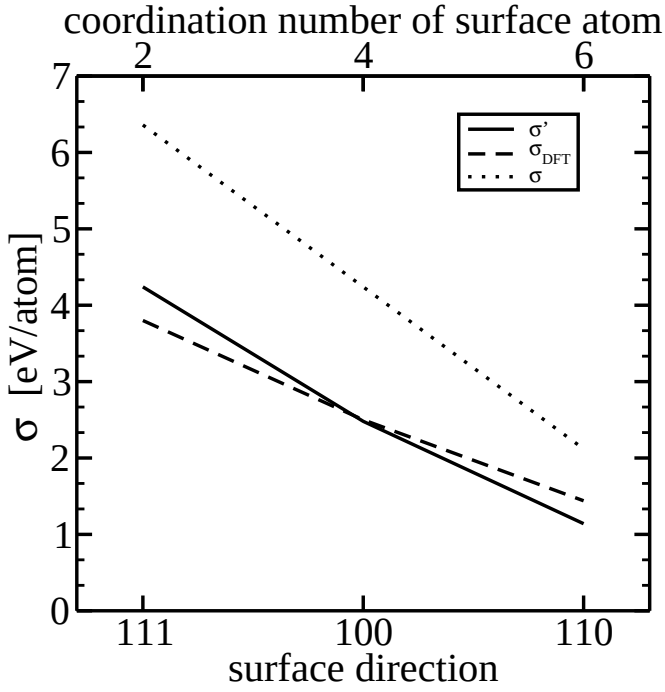

Figure 3.5: Surface energies for several tungsten surfaces. The estimation σ' is calculated according to equation 3.8, the estimation σ according to equation 3.7 and σ_{DFT} by DFT utilizing the GGA-PBE..

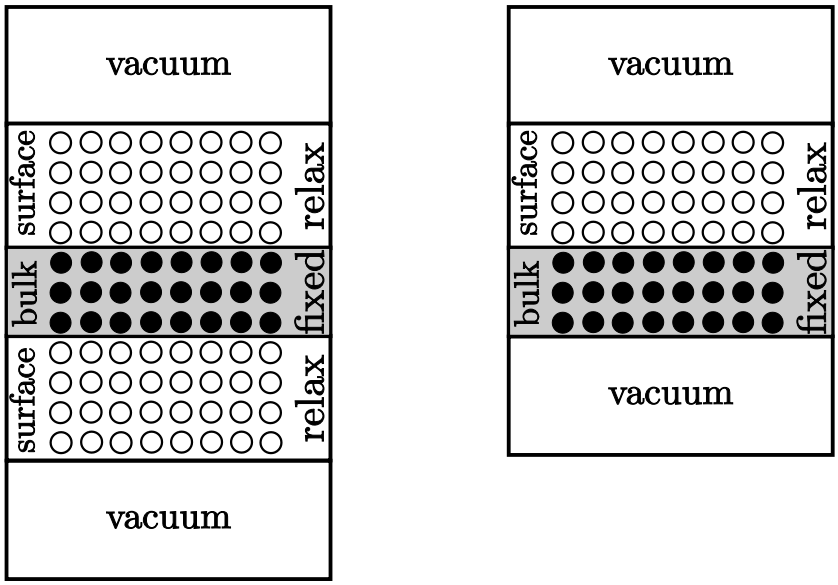

Figure 3.6: DFT setups for calculating surface properties. (a) shows a symmetric slab, (b) shows an asymmetric slab. The bulk regions are indicated by black atoms, surface regions by white atoms respectively. For details see text.

one surface of the slab across the vacuum to the neighboring unit cell is possible. Concerning the slab thickness a minimum number of layers is needed to reproduce the correct layer relaxations and surface energies. Depending on the crystallographic direction of the surface the number of layers needed may vary considerably. The adsorption studies in chapters 4 and 5 are done for the *W(110)* surface. Nevertheless for a fundamental understanding of the underlying physics also the other low index surfaces of tungsten are discussed. For the *W(110)*, *W(100)* and *W(111)* surfaces the calculated data are shown in tables 3.4, 3.6 and 3.7. The relative layer relaxation Δd_{ij} is defined in equation 3.10 being the relative deviation of the interlayer spacing d_{ij} between layer i and j with respect to the ideal bulk layer distance d_{bulk}.

$$\Delta d_{ij} = (d_{ij} - d_{bulk})/d_{bulk} \tag{3.10}$$

For the *W(110)* surface the relaxations were calculated using both symmetric and asymmetric slabs (see table 3.4). The symmetric slabs consisted of 5, 7, 11 and 13 layers and the asymmetric slabs of 5 up to 10 layers. The ideal bulk layer distance is $d_{110} = 1/2\sqrt{2}a_W = 2.25$ Å. For the first interlayer spacing Δd_{12} all models find an interlayer contraction of ≈ 3.6 % (or $d_{12} = 2.17$ Å). For Δd_{23} the interlayer distance expands by ≈ 0.4 % yielding $d_{23} = 2.26$ Å. For the deeper inter layer

Table 3.4: Layer Relaxations of the *W(110)* surface. The bulk layer distance in [110] direction is 2.25 Å and the relaxations $\Delta d_{ij} = (d_{ij} - d_{bulk})/d_{bulk}$ are given as relative deviations from this value. The relaxation energy E_{relax} is given in meV/surface atom (s.a.) and the surface energy E_{surf} is given in two different units, namely [eV/s.a.] and [J/m^2].

	symmetric				asymmetric					
# layers	5	7	11	13	5	6	7	8	9	10
E_{relax} [meV/s.a.]	26	29	29	31	26	34	30	27	27	27
E_{surf} [eV/s.a.]	1.48	1.48	1.50	1.50						
E'_{surf} [J/m^2]	3.31	3.30	3.33	3.34						
	[%]				[%]					
Δd_{12}	-3.6	-3.6	-3.6	-3.8	-3.5	-3.9	-3.7	-3.5	-3.6	-3.6
Δd_{23}	0.4	0.4	0.5	0.6	0.3	0.6	0.4	0.6	0.3	0.4
Δd_{34}		-0.0	0.0	0.0	0.2	-0.1	0.1	0.0	0.0	0.0
Δd_{45}			0.2	0.3			0.1	0.4	0.0	0.2
Δd_{56}				0.0				0.0	0.0	-0.2
Δd_{67}									0.0	0.2
Δd_{78}										-0.1

distances the deviations from the bulk value are smaller than 0.4 %, except for the 8 layer asymmetric slab. From this survey it becomes clear that already slabs of 5 layers give a reasonably good description of the *W(110)* surface. To be on the save side for most of the calculations concerning indium adsorption, a seven layer symmetric slab was used. For the study of the oxygen adsorption inspecting the adsorption energies reveals that for the *O/W(110)* system an asymmetric 9 layer slab provides well converged adsorption energies with respect to the number of layers (for details see section 4.4).

After studying the dependency of the layer relaxations with respect to the slab thickness, comparison to different experimental data and other theoretical studies of the *W(110)* surface is made. An overview is given in table 3.5. Older theoretical studies –one low energy electron diffraction study (LEED), one high energy ion scattering and one photoelectron diffraction study– with low accuracy do not recognize any significant layer relaxation for the first W layer [55, 89, 48]. In more recent LEED studies a layer relaxation of -3.0 % [3, 92] is found. In a LEED study connected to this work (reference [91]) a layer relaxation of -1.8 % is reported which is somewhat smaller than the data, but the agreement is still

Table 3.5: Comparison of first layer relaxation for *W(110)* as obtained by various experimental and theoretical methods

	Method	$\Delta d_{12}/d_{bulk}[\%]$	Ref.
Experiment			
Lagally et al.	LEED	0.0 ± 3.0	[55]
Smith et al.	High energy ion scatt.	< 2	[89]
Kim et al.	Photoelectron Diffrac.	0.0 ± 1.0	[48]
Arnold et al.	LEED	-3.0 ± 0.6	[3]
Teeter et al.	LEED	-3.0 ± 1.3	[92]
Stöhr et al.	LEED	-1.8 ± 1.3	[91]
Theory			
Luo et al.	tight-binding	-1.4	[62]
Rodriguez et al.	equivalent crystal theory	-2.1	[82]
Xu et al.	tight-binding	-5.0	[108]
Arnold et al.	LDA (7-layers)	-3.3	[3]
Dennler et al.	PBE (6-layers)	-4.6	[22]
this work	PBE (7-layers)	-3.7	

within the error ranges. All theoretical studies all find a first layer relaxation of some percent. A tight-binding [62] and an equivalent crystal theory study [82] report values of -1.4 % and -2.1%, respectively which is somewhat less than the value found in this work. Another tight-binding [108] and a DFT study [22] find values of -5.0 % and -4.6 %, which are slightly larger than the present value. The only study in close agreement is the DFT-LDA work of Arnold et al. [3] with a first layer relaxation of -3.3 %.

A quantity that is not accessible to experiments is the relaxation energy E_{relax}. It is defined as the energy difference of the total energy of the unrelaxed bulk truncated surface slab E_{trunc} to the final relaxed surface slab E_{slab} as given by

$$E_{relax} = E_{trunc} - E_{slab}. \tag{3.11}$$

The given definition holds for asymmetric slabs, in case of symmetric slabs E_{relax} is multiplied by a factor of $\frac{1}{2}$ in order account to for the two relaxed surfaces. The relaxation energies for the *W(110)* surface are shown in table 3.4 and given in unit meV/surface atom (meV/s.a.). For symmetric slabs a relaxation energy of 29 meV/s.a. for 11 and 31 meV/s.a. for 13 layers is found which indicates that these slabs are sufficiently thick already. For asymmetric slabs the relaxation energy E_{relax} converges to 27 meV/s.a. for larger slab thicknesses. Dennler et al.

[22] find a somewhat larger value of 39 meV/s.a. using an asymmetric slab of six layers.

The surface energy

$$E_{surf} = \frac{1}{2A}\left(E_{tot}^{slab} - NE_{bulk}\right) \tag{3.12}$$

is only calculated for symmetric slabs. In equation 3.12 E_{tot}^{slab} is the total energy of the calculated surface slab of N layers, E_{bulk} is the total energy of the bulk phase and $2A$ is the considered surface area. Since a symmetric slab is used, twice the area A of the surface unit cell has to be taken into account. In contrast to the simple estimations according to equations 3.7 and 3.8 of the bond breaking model the DFT derived E_{surf} also includes electronic and ionic relaxations.

For the *W(100)* and the *W(111)* surfaces the same properties as for the *W(110)* are calculated and shown in tables 3.6 and 3.7. Since both surfaces have a lower density of atoms in the surface layer than *W(110)*, relaxation effects for these two surfaces are more expressed than for *W(110)*. In case of the *W(100)* surface (see table 3.6) relaxation energies of 160 - 170 meV/s.a. are found. Compared to the *W(110)* surface it is also found, that the relaxation of the top most layer is much stronger with a value of $\Delta d_{12} \approx 12\%$. The deeper layers relax fast to the bulk layer distance of 1.59 Å. It should be noted here, that in addition to layer relaxations the in-layer reconstruction of the *W(100)* has to be taken into account. However, reconstructions energies for metallic surfaces are rather small, in general [22]. For the *W(111)* surface the largest relaxation energies of all the studied surfaces with more than 470 meV/s.a. is found. The interlayer relaxations are even larger than for *W(100)*, namely ≈ 21 % for the first layer spacing and ≈ 23 % for the second layer spacing. On this surface the third layer spacing shows a notable expansion of about 17 %. The surface energies of the *W(100)* and *W(111)* surfaces are larger than that of *W(110)*, indicating that *W(110)* is the most stable surface.

3.4.3 The Clean *W(110)* Surface

The structure of the bcc *(110)* surface is sketched in figure 3.7. The main crystal directions in the surface plane are the $[1\bar{1}0]$ and the [001], as indicated in figure 3.7. For constructing two-dimensional super cells unit cell vectors a_1 and a_2 are used. Before studying more complex phenomena on the *W(100)* surface, first the stability of the surface is investigated. As listed in table 3.3, *W(100)* is the surface with the lowest surface energy. On the other hand the atom density in the *(110)* surface is high since the atom arrangement nearly is that of an hexagonal close packed layer (It is called pseudo-hexagonal). Different to W(100)

Table 3.6: Layer Relaxations of the *W(100)* surface. The bulk layer distance is 1.59 Å and the relaxations $\Delta d_{ij} = (d_{ij} - d_{bulk})/d_{bulk}$ are given as relative deviations from this value. The relaxation energy E_{relax} is given in meV/surface atom (s.a.) and the surface energy E_{surf} is given in two different units, namely [eV/s.a.] and [J/m^2].

# layers	7	11	13
E_{relax} [meV/s.a.]	175	173	161
E_{surf} [eV/s.a.]	2.55	2.59	2.61
E'_{surf} [J/m^2]	4.03	4.07	4.11
		[%]	
Δd_{12}	-11.3	-11.9	-11.7
Δd_{23}	2.2	3.0	2.9
Δd_{34}	-0.8	-1.5	-1.5
Δd_{45}		0.6	0.5
Δd_{56}			-0.4

Table 3.7: Layer Relaxations of the *W(111)* surface. The bulk layer distance is 0.92 Å and the relaxations $\Delta d_{ij} = (d_{ij} - d_{bulk})/d_{bulk}$ are given as relative deviations from this value. The relaxation energy E_{relax} is given in meV/surface atom (s.a.) and the surface energy E_{surf} is given in two different units, namely [eV/s.a.] and [J/m^2].

# layers	13	19
E_{relax} [meV/s.a.]	474	501
E_{surf} [eV/s.a.]	3.94	3.94
E'_{surf} [J/m^2]	3.59	3.58
	[%]	
Δd_{12}	-20.6	-21.1
Δd_{23}	-22.7	-23.7
Δd_{34}	15.7	17.3
Δd_{45}	-4.0	-4.9
Δd_{56}	2.3	2.0
Δd_{67}		1.2
Δd_{78}		1.3
Δd_{89}		-1.8

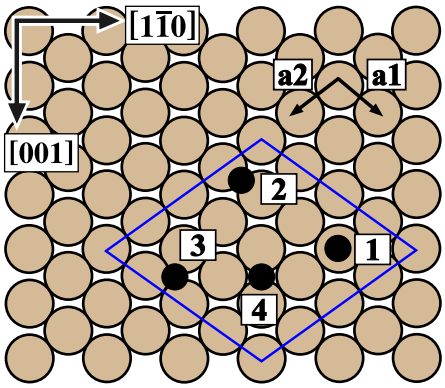

Figure 3.7: High symmetry adsorption sites on a bcc *(110)* surface. The labeling of the sites is given in the text and table 3.8. For single-site adsorption of adatoms on *W(110)* the unit cell used in the calculation is indicated in the sketch.

(see reference [22]) for the *W(100)* surface no reconstruction is known in literature. That is why for all further studies the structure shown in picture 3.7 is assumed for the clean *W(110)* surface. When studying adsorbates on it later, it is also important to rule out possible vacancy or exchange processes of adsorbate atoms with substrate atoms, or vacancies within the surface. Equation 3.13 defines the vacancy formation energy E_{vac},

$$E_{vac} = \frac{1}{n}\left(E_{slab}^{vac} - E_{slab}^{clean} - nE_{free}\right), \tag{3.13}$$

in which n is the number of vacancies, E_{slab}^{vac} is the total energy of the surface slab with a vacancy present, E_{slab}^{clean} is the total energy of the perfect surface slab and, finally, E_{free} represents the energy of the free atom. E_{vac} for the *W(110)* surface is calculated with an asymmetric slab of four W layers and a (4×4) lateral unit cell as sketched in figure 3.7. The DFT calculation gives a value of $E_{vac} = 10.2$ eV/atom, which is very costly and thus very improbable. In other words, surface vacancies on *W(110)* are not expected to be present and can safely be ignored for all further considerations. A test calculation was done for a (4×4×4) *W* bulk unit cell containing 47 atoms and 1 vacant site, for which the vacancy formation energy amounts to 11.3 eV/atom, being even larger by 10% than the value for the *W(110)* surface.

A more detailed view at this point can be taken when adatoms are considered. Equations 3.14 and 3.15 formulates the impurity formation energies relative to a vacancy present in the *W(110)* surface (equation 3.14) and the process of atom exchange from a perfect surface to filling up the vacancy with an adatom (equation 3.15). In these equations, E_{slab}^{imp} is the total energy of the slab with the vacancy

filled up with one impurity atom. The energies E_W^{free} and E_{imp}^{free} are defined as the total energy of the free atoms as in equation 3.13. By definition, these two quantities are related to the vacancy formation energy E_{vac} by $E'_{imp} - E_{imp} = E_{vac}$.

$$E_{imp} = \frac{1}{n}\left(E_{slab}^{imp} - E_{slab}^{vac} - nE_{imp}^{free}\right) \tag{3.14}$$

$$E'_{imp} = \frac{1}{n}\left(E_{slab}^{imp} + nE_{W}^{free} - E_{slab}^{clean} - nE_{imp}^{free}\right) \tag{3.15}$$

For oxygen atoms the result is $E_{imp} = -1.42$ eV and $E'_{imp} = +8.76$ eV. As discussed later on in sections 4.2 and 5.3 the energy E_{imp} is in this case less than the adsorption energies on a perfect surface. Also considering the total process, still an energy of 8.76 eV per impurity oxygen is needed to exchange one surface tungsten with one oxygen atom. For indium atoms a much more negative energy of $E_{imp} = -5.06$ eV, which is energetically more favorable than adsorbing on the perfect surface (see section 5.3), and a value of $E'_{imp} = +5.13$ eV. This implies that indium atoms embedded in the surface would be favored with respect to adsorption on top the perfect surface. Nevertheless, the energy of 5.13 eV for exchanging one *In* atom with one *W* atom is still rather large and therefore this process is rather improbable. It is further noted, that this view as given before is only a very simple one. For a more detailed study of this processes nudged elastic band method calculations for the removal and adding process of adatoms can be done to study possible energy barriers between the initial and the final states. More complex scenarios of the exchange process are possible, since *W* atoms, which are missing in the first surface layer, may not necessarily leave the surface, but will rather be present as adatoms on the *W(110)* surface itself. However, since the energies for E'_{imp} in both cases of indium and oxygen are largely positive, for these other scenarios still large positive energies to the disadvantage of the placement of an impurity atom in the *W(110)* surface layer are expected.

3.4.4 Adsorption Sites on *W(110)*

On the bcc *(110)* surface - as shown in figure 3.7 - four high symmetry adsorption sites can be found. The sites are characterized by their coordination numbers: The ontop adsorption site (label "1" in figure 3.7) is coordinated onefold, the bridge site ("2") two fold, the hollow-3 site ("3") threefold and the hollow-4 site ("4") fourfold. Since in case of the hollow-4 site the distances to the neighboring atoms are not equal, this site is sometimes also referred to as long bridge or pseudo-4-fold adsorption site. Nevertheless, within this study the term hollow-4 site will be used for this site. In table 3.8 also the exact positions of the adsorption

Table 3.8: Definitions and coordinates of the high symmetry adsorption sites on a bcc *(110)* surface. The coordinates are given relative to a 4-fold hollow position, since it coincides with the position of the substrate atom when bulk layer stacking is continued. For a sketch of the adsorption sites see figure 3.7.

#		$\lvert\vec{d}\rvert$	$[1\bar{1}0]$	[001]
1	ontop	$a_W/2$	0	$a_W/2$
2	bridge	$\sqrt{3}/4a_W$	$\sqrt{2}/4a_W$	$a_W/4$
3	3-site hollow (H3)	$\sqrt{2}/8a_W$	$\sqrt{2}/8a_W$	0
4	4-site hollow (H4)	0	0	0

sites are printed. They are given as distance $|\vec{d}|$ of the adsorption site relative to the four fold coordinated adsorption site which coincidences with a regular substrate site assuming layer stacking as in the bulk material. The coordinates of $\vec{d}$ are given in units of the bulk bcc tungsten lattice constant a_w with respect to the coordinate axes printed in figure 3.7 namely the $[1\bar{1}0]$ and the [001] direction.

The strength of binding of adatoms to these sites is given in terms of the adsorption energy E_{ad},

$$E_{ad} = \frac{1}{n}(E_{tot}^{slab} - E_{tot}^{clean} - nE_{free}). \tag{3.16}$$

in which E_{tot}^{slab} is the total energy of the surface slab including the adsorbed atom, E_{tot}^{clean} is the total energy of the clean slab, and nE_{free} is the total energy of the n free atoms under consideration. The calculation of the adsorption energy E_{ad} was made for two different coverages: for the case of a well isolated atom on the *W(110)* surface the adsorption energy for a single atom within a (4×4) unit cell was calculated as indicated in figure 3.7. A (1×1) unit cell was used for the adsorption energy at one monolayer coverage, which was needed as reference system for calculating phase stabilities. The DFT total energy of a single free indium atom is $E_{free} = -0.36$, whereas for oxygen half of the total energy of a free oxygen molecule $E_{free} = 1/2 \cdot (-9.84)$ eV has been taken (see section 3.3). Details about the adsorption energies of oxygen on tungsten surfaces will be given in section 4.2, whereas the adsorption of indium is treated in section 5.3.

4

Oxygen Adsorption on *W(110)*

In this section the oxygen adsorption on *W(110)* is studied by combining density functional theory (DFT) calculations and the cluster expansion (CE) method. Section 4.1 gives an overview of the work that has been done on the system so far. Section 4.2 evaluates the adsorption energies of oxygen at the different adsorption sites on the *W(110)* surface. In conclusion, from section 4.2 the cluster expansion for the two symmetry equivalent H3 sublattices is constructed and discussed in sections 4.3 to 4.6. Section 4.7 discusses the structural details of the four identified ground state structures. The adsorption and ordering behavior at finite temperatures is discussed in sections 4.8 and 4.9. Finally, the influence of surface vibrations is discussed in section 4.10.

4.1 Previous Work on the *O / W(110)* System

Adsorption of oxygen on the *W(110)* surface has been studied in the past to some extent. Low energy electron diffraction (LEED) has been used to characterize the detailed structure of the (2×1) phase [97], and the critical behavior and phase transitions at coverages of $x_O = 0.50$ [11, 4] and various other coverages [102]. (It should be noted, that a coverage of $x_O = 1$ refers to the *W(110)* surface completely covered with one monolayer of atomic oxygen in a (1×1) structure). The saturated (1×1) structures have been studied by Daimon et al. [20] using full solid-angle X-ray photoelectron diffraction (XPD) and by Ynzunza et al. [110] by solid-angle photoelectron diffraction. Ordering phenomena have been investigated by Wu et al. [107] at coverages of $x_O = 0.25, 0.50$ and 0.65. Growth kinetics has been studied at the high coverage of $x_O = 0.68$ by Tringides [94]. Scanning tunneling microscopy measurements (STM) confirmed structural details [46] indicating stress effects within the adsorption structures. A number of theoretical studies are presented, which are mostly based on empirically derived parameters.

To our knowledge, up to now only one DFT study concerning the adsorption of single O atoms exists [112], in which a finite cluster geometry was applied for modeling the surface. In this reference, interaction parameters are derived which entered a three-state lattice gas model for deriving the phase diagram. Other authors studied phase stabilities and related properties by application of a lattice gas model [60, 29, 103, 95, 99, 100, 112, 113, 114, 111], in which the interaction energies are determined by fitting to experimental data: for example, Williams et al. [103] fitted to the LEED data of Lu et al. [60].

In the present work, for the first time *ab initio* DFT techniques for studying the adsorption of atomic oxygen on *W(110)* are applied for the complete coverage range $0 \leq x_O \leq 1$, and the corresponding phase diagram is constructed without any empirical parameters and ad-hoc assumptions. For this purpose, the cluster expansion (CE) [86, 7] for the oxygen adsorbate layer is applied. For this purpose the interaction parameters are derived from a large set of DFT calculations. Finally, for determining the temperature dependent phase stabilities Monte Carlo (MC) calculations utilizing the CE effective interaction energies are made. As a byproduct, the ground state phases with their relaxed structural details having the precision of up-to-date DFT methods are available.

4.2 Adsorption Energies of Oxygen on *W(110)*

In this section the adsorption energies E_{ad} for O atoms according to equation 3.16 are derived. The exact location of the adsorption sites has already been given in section 3.4.4 (see table 3.8 and figure 3.7). As pointed out there, the adsorption energies are calculated for a (4×4) unit cell containing one O atom (representing the single atom limit) and a (1×1) lateral unit cell for the fully covered surface. For single atom coverage, as well as for the full (1×1) coverage the most stable adsorption site is H3 with adsorption energies of $E_{ad} = -4.16$ eV/atom and $E_{ad} = -3.88$ eV/atom, respectively. Adsorption at H4 sites is less stable than at H3, namely for an isolated O atom by 0.26 eV/atom and for the full coverage case by 0.81 eV/atom. For single atom adsorption the difference to the H3 site is not large, but it should be noticed that allowing for lateral relaxation will drive the O atom towards a neighboring H3 site. Therefore, according to the DFT results adsorption at H4 sites is impossible. At both extreme coverages the bridge and on top site are even less stable than the H4 sites, as shown in table 4.1. As for the H4 site, lateral relaxation will move the O atoms towards energetically more favorable H3 sites. As an additional confirmation of the statically relaxed DFT calculations, molecular dynamics DFT simulations at $x_O = 1$ were carried out. Within a (4×4) unit cell with 16 adatoms the system was annealed at 2200 K

Table 4.1: Adsorption energies of indium and oxygen in eV/atom. For each species the adsorption energy is calculated for a single atom in a (4×4) unit cell as indicated in figure 3.7 and for a fully covered *W(110)* surface with a (1×1) structure. For oxygen the most favorable adsorption site is H3 in both cases. For indium H4 is the most favorable site at low surface coverage and H3 is the most favorable site at full coverage. For details see text.

	Indium		Oxygen	
	(4×4)	(1×1)	(4×4)	(1×1)
ontop	-2.62	-2.36	-3.08	3.71
bridge	-2.75	-2.65	-3.68	-3.02
H3	-2.91	-2.69	-4.16	-3.88
H4	-2.99	-2.64	-3.90	-3.07

and cooled down to 0 K afterwards. The final stable configuration of this simulation indeed is a regular (1×1) pattern with all adatoms residing on the same H3 sublattice sites. Therefore, for ground state properties and adsorption structures only H3 sites are expected to be occupied. More details concerning the different *O* adsorption structures will be discussed in the following sections.

The only other DFT study on oxygen adsorption on *W(110)* of Załuska-Kotur et al. [112], which applied a finite cluster geometry for modeling the surface, is in reasonable agreement with the present work. The reported energy differences for single atom adsorption in reference [112] are ≈ 0.2 eV between the H3 and H4 site, ≈ 1.2 eV between the H3 and the ontop site, and ≈ 0.8 eV between the bridge and ontop sites.

4.3 Setup of the Cluster Expansion

As discussed in section 4.2 for *O* the three fold coordinated adsorption sites are found to be the most stable ones at low coverages as well as at a full monolayer. Based on these findings, that only the H3 adsorption sites are important for the adsorption structures, it can now be safely concluded that the cluster expansion in 4.4 for the two equivalent H3 sublattices will give a physically meaningful description of the adsorption energetics for all coverages up to $x_O = 1$. Figure 4.1 (a) sketches the setup chosen for the CE. The two H3 sublattices are sketched as black and white circles. *W* atoms appear in brown color. Also shown in the figure are the shortest nearest neighbor distances as blue lines. Taking the

coordinates of table 3.8 the shortest distance of the two sublattices is calculated as $\frac{1}{4}\sqrt{2}a_W = 1.13$ Å. This is shorter than 1.23 Å, which is the bond length of the oxygen molecule O_2 (compare section 3.3). For this reason special care has to be taken later on when constructing the CE, since also repulsive configurations with two O atoms at this extremely short distance are allowed by the chosen setup. Details concerning this issue will be discussed in the following sections.

Figure 4.1 (b) reveals the distance resolution of the chosen setup in more detail. The respective distances (given in units of the underlying lattice constant a_W) are plotted against the increase of the distance relative to the last occurring lattice distance. In case of two sublattices the distances are ranging from $\frac{1}{4}\sqrt{2}a_W$ –as pointed out before– up to $\parallel a_1 + 4a_2 \parallel = 0.5\sqrt{43}a_W$ which corresponds to the 32nd nearest neighbor distance found in the lattice. Analyzing the increase in the distances for the chosen setup one finds that there are three increases of $\approx 0.25\text{Å}/a_W$, all others are smaller than $\approx 0.15\text{Å}/a_W$. Since there are two equivalent sublattices considered, also increases in distance by 0 can be found. These occurrences are due to distances, which connect lattice points within the same sublattice and can be found as well in the other one. For comparison, in figure 4.1 (b) also the distances for a lattice setup with only one sublattice is given. The smallest possible distance is $\frac{1}{2}\sqrt{3}a_W$, which is more than twice as large than for the two sublattice case. For the maximum distance considered the same as for the two sublattice case is chosen. It is obvious that the occurring distances are a subset of the two sublattices case. Thus an increase for one sublattice is always equal or larger than for two or even more sublattices, since the density of available distances becomes larger. That is why for the one sublattice case most steps are $\approx 0.25a_W$ or larger, some are found to be around $\approx 0.2a_W$ and only two are below $0.15a$. Therefore, the chosen setup with two sublattices is able to model the lateral interactions starting from lower distances, and it improves the resolution in distances by a factor of ≈ 2.

4.4 Cluster Expansion

Before starting with the cluster expansion itself a suitable setup for the DFT calculations has to be found. From the considerations of section 3.4.2 it is already clear, that slab thicknesses of five layers or more give qualitatively good agreement for the surface energies and layer relaxations, no matter if symmetric or asymmetric slabs are chosen. In order to simplify the processing of the DFT data for the CE, it is more convenient to use asymmetric slabs for the DFT calculations. Since the CE aims at the most accurate description of the adsorption energetics as possible, the number of W layers in the slab has to be chosen that

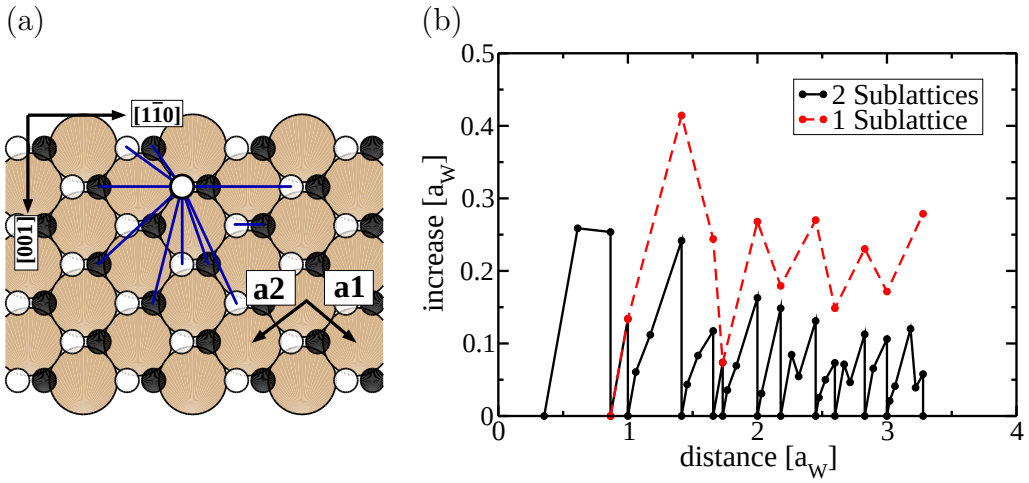

Figure 4.1: bcc *(110)* surface: (a) Lattice definition used for the cluster expansion of the two equivalent 3-fold coordinated sublattices H3A (black circles) and H3B (white circles). Also shown are the shortest nearest neighbor distances by blue lines. (b): comparison of the different occurring distances when choosing one or two equivalent sublattices on a bcc *(110)* surface. For details see text.

way, so that inaccuracies in the adsorption and surface energies, which might be due to the finite size of the system, are minimized. To find a suitable slab thickness the total energy difference

$$\Delta E = E_{tot}^{(1\times1)} - E_{tot}^{clean} \tag{4.1}$$

for (1×1) unit cells with a full monolayer of O and the clean surface is calculated. For this calculations –as pointed out before– asymmetric slabs with layer numbers ranging from 4 to 10 are used. An energy cutoff of 500 eV and a k-point set of 15×15×1 after Monkhorst and Pack [68] are applied. The results are plotted in figure 4.2. Although the energy difference ΔE is not changing by more than 0.02 eV, convergence is only achieved when using nine or more layers. The choice for the final model is an asymmetric slab of nine W layers plus a vacuum region of ≈ 27 Å equivalent to 12 *W(110)* bulk layers, which is included in the unit cell. During relaxation of the atomic positions the bottom three W-layers are kept fixed. In order to keep the computational effort as low as possible the energy cutoff is reduced to 400 eV. For the (1×1) surface slab a 15×15×1 k-points mesh is used as for the calculation of ΔE, and the mesh is scaled down accordingly for larger unit cells. The integration over the Brillouin zone is done by the smearing method of reference [64] applying a width of 0.1 eV. The 5p semicore states of W are treated as valence states. For the geometrical relaxation the Hellman-

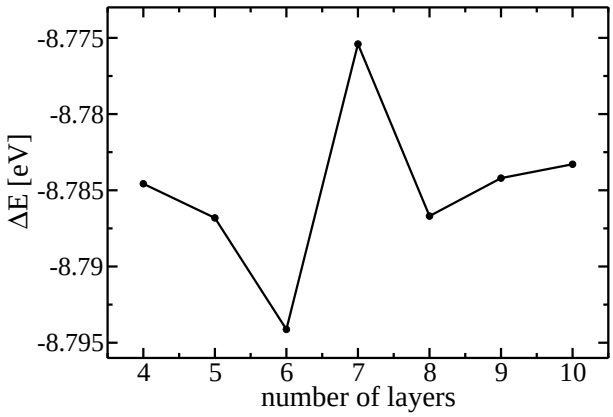

Figure 4.2: Total energy difference ΔE according to equation 4.1 for a varying number of W layers in the slab model. Convergence is found at 9 Layers. For details see text.

Feynman forces were minimized with a quasi-Newton algorithm to absolute values less than 0.01 eV/Å.

After defining the lattice for the CE in more detail in the previous section and choosing the proper slab model for extended unit cells, the CE itself can be converged. For a suitable thermodynamic representation the arguments of section 2.4.2 are used. Reconsidering equation 2.67 it is obvious that up to a constant only the surface energy E_{surf} of equation 2.53 has to be determined. For the special case of O adsorption on *W(110)* it turns into

$$E_{surf} = \frac{1}{A}\left[E_{tot}^{slab} - x_O E_{tot}^{(1\times1)} - (1-x_O)E_{tot}^{clean}\right] \tag{4.2}$$

with the total energy of a (1×1) covered slab $E_{tot}^{(1\times1)}$, and the surface coverage of oxygen x_O ($x_O = 1$ corresponding to the coverage by one monolayer or the (1×1) surface structure). For converging the CE two different configuration spaces are used. First, configurations that are built up by all unit cells containing up to eight W atoms are used. Within this set of structures, which consisted of 4203 configurations, also repulsive configurations with short O-O distances are allowed. Including the repulsive configurations is needed, because the complete surface energetics should be represented by the CE. Nevertheless, it is clear that structures like the two shown in figure 4.3 cannot be ground state structures. The structure in figure 4.3 (a) has a (2×4) unit cell and a surface formation energy of 923 meV/(1×1). Similarly the structure sketched in figure 4.3 (b) has a (3×4) unit cell containing and a surface formation energy of 569 meV/(1×1). Choosing the same coverage but all O atoms in repulsive arrangement (i.e. very

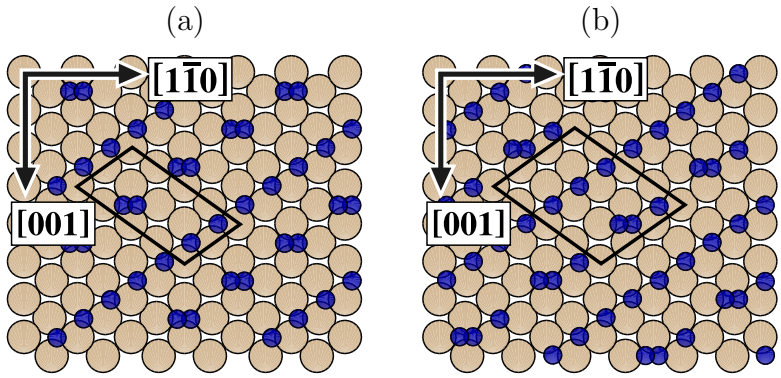

Figure 4.3: Two repulsive O adsorbate structures which are used as input structures for the CE. The relaxation is only possible if the coordinates in the surface plane are kept fixed. The surface formation energies are 923 meV/(1×1) for (a) and 568 meV/(1×1) for structure (b). For details see text.

short O-O distances) the surface formation energy is increased even further to 1984 meV/(1×1). For the DFT calculations with fixed coordinates the total energy has some error, since the lateral position always has to be set externally. In case of the two structures used for the CE this error is also introduced. But since for the fit of the interaction energies the allowed ranges δ_i for the fitted surface formation energies are given by equation 2.76 which allows for larger deviation for structures further away from the ground state line, the error made by DFT can be handled by the CE and thus does not effect a correct determination of the interaction energies. After considering the strong repulsive interactions the number of W atoms in the unit cell is increased up to 12 atoms. But in order to keep the number of possible configurations as low as possible the structures with very short O-O distances are now forbidden. In total 80394 configurations for $0 < x_O < 1$ can be found under these conditions.

Besides the two structures of figure 4.3 60 ordered structures were calculated by DFT for constructing the final fit of the CE. For all these structures the forces have been relaxed and the final positions of the adsorbed O atoms are always on H3 sites. The resulting ground state diagram is shown in figure 4.4. It shows the surface energy E_{surf} versus the O concentration x_O of the different structures. The DFT calculated energies are indicated as circles and the CE energies as crosses. Since the range of DFT energies is from -144 meV/(1×1) up to 923 meV/(1×1), and only few energies for allowed structures with the short O-O distance are in the far positive energy range, the energy scale of the diagram is restricted to 100 meV/(1×1). The maximum fitting error for the final figure set

is 6.1 meV/(1×1) and the root mean square error (RMS) amounts to 2.1 meV. The value of the cross validation score $S_{CV} = 3.7$ meV is slightly larger than the RMS value, but still within the typical accuracy of DFT calculations. One might therefore safely conclude that the CE yields an accurate description of the input DFT energies as well as accurate energies for unknown structures (i.e. structures, which were not calculated by DFT). The most important structures of the system are the ground state structures at $x_O = 0.20$, 0.25, 0.50 and 0.75 indicated by vertical dashed lines in figure 4.4. The ground states are connected by the ground state line (blue line) line forming a convex hull around all calculated structures. A detailed discussion of the ground states will be given in section 4.7. The ground state line for the CE calculated structures is not shown in figure 4.4 since it is identical with that of the DFT values. The *O* content of the calculated structures is not distributed uniformly over the whole concentration range. For coverages larger than $x_O = 0.50$ only ten DFT calculations had to be performed. For the low coverage regime the remaining 50 calculations had to be done. This is also reflected by the distribution of the ground states of the system. At $x_O = 0.50$ and $x_O = 0.75$ two very stable ground states are found with a thermodynamic stability $\Delta E_{stab}(x_O)$ of -51.1 meV/(1×1) and -38.1 meV/(1×1), respectively (see the definition of $\Delta E_{stab}(x_O)$ in section 2.4.1 for details.). For the ground states at $x_O = 0.20$ and $x_O = 0.25$ $\Delta E_{stab}(x_O)$ is only -1.4 meV/(1×1) and -0.2 meV/(1×1) indicating only low thermal stability. Furthermore, a number of other calculated structures with $0 < x_O < 0.50$ lies very close to the ground state line giving a very dense hierarchy of energies. This phenomenon reflects the low ordering behavior at these coverages which is also known for weakly ordering bulk binary alloys [90]. A selection of structures with surface formation energies close to the ground state line and their corresponding adsorption structures are listed in appendix B.

The ground state diagram in figure 4.4 is connected to the ground state search as shown in figure 4.5. There, the predictions of all 80394 configurations of the second configuration space mentioned above are presented. Since the repulsive configurations with very short *O*-*O* distances are omitted, only surface formation energies up to 400 meV/(1×1) are found. Again, as for the DFT calculated structures, for coverages up to $x_O = 0.50$ E_{surf} a number of structures is very close to the ground state line, resulting in the same arguments as before. According to the fitting procedure of the CE, which should reproduce the energetics of the DFT input structures and also the DFT ground state line, for the predicted structures in figure 4.5 the ground state line is identical with that of figure 4.4. Since evaluation of the surface energy E_{surf} for the predicted structures gives no new ground state structures the CE is considered to be converged. The final set

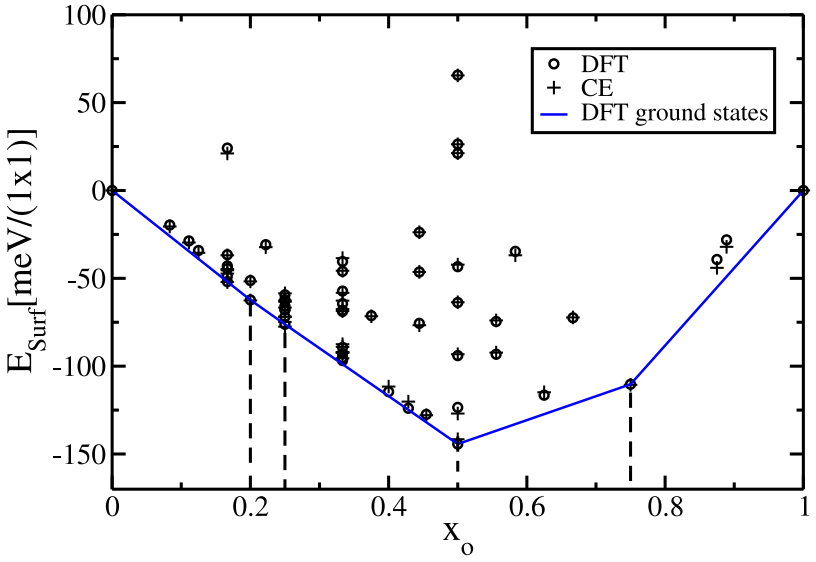

Figure 4.4: Comparison of density functional theory (DFT) surface formation energies and fitted cluster expansion energies (CE) for 60 ordered structures. Four ground states are detected at x_O = 0.20, 0.25, 0.50 and 0.75, and their energies are connected by the ground state line.

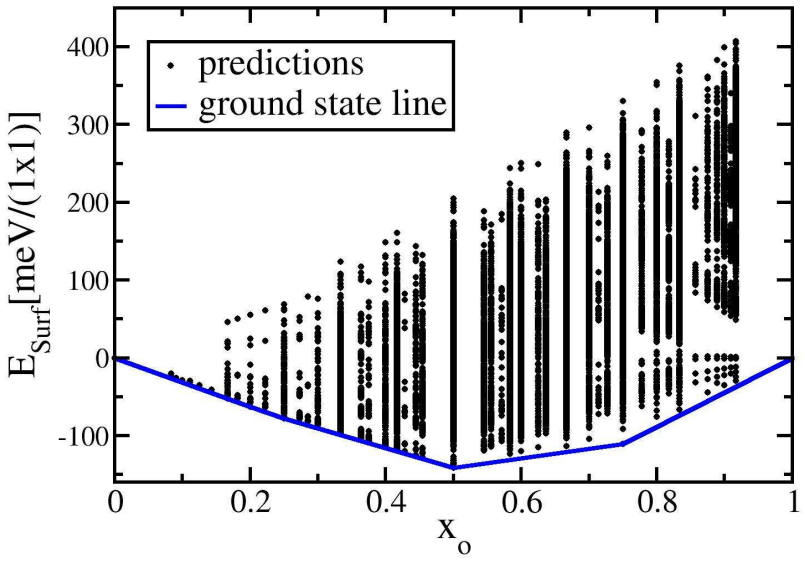

Figure 4.5: Concentration dependent surface formation energy for *O* on *W(110)*. Results of cluster expansion predictions for 80394 structures as used for searching for the ground states. The ground state line (i.e. connection of structures with lowest energy) is indicated. All unit cells with up to 12 atoms are included but structures with the very short *O*-*O* distances of 1.13 Å (nearest-neighbor H3 sites) are not taken into account.

of figures and their respective interaction energies enable a detailed description of the adsorption energetics of this system. Later on in section 4.8 these interactions can be used to perform Monte Carlo simulations.

4.5 Figure Analysis

The final selection of figures consisted of 34 figures comprising the constant and the onsite terms, 10 pairs, 19 triples and 3 quadruples. Figure 4.6 shows their respective interaction energies versus the figure size d. For the pair interactions the parameter d is the vertex-vertex distance of the lattice points, for the many-body figures d is defined as the mean distance of the connections in the figure. For the displayed final figure set all pair interactions up to the 10th nearest neighbor distance ($\sqrt{2}a_W = 4.51$ Å) and different sizes of triples and quadruples are chosen. Although pair figures up to a distance of 10.45 Å were allowed,

they are unimportant, since none of them is chosen by the genetic algorithm. This fact is also reflected in the decrease of the absolute value of the interaction energy with increasing interatomic distance. In analogy to the pair figures, the interaction energies of the triples and quadruples also decrease with increasing mean atomic distance. A more detailed investigation of the interaction energies shows that the main contributions come from five pair interactions and three triple interactions. The main pair interactions correspond to pair distances of 1.13, 2.76, 3.38, 3.74, 5.29 Å. For the smallest pair figure with d = 1.13 Å, a very large positive interaction energy of 1763 meV is obtained representing the very strong repulsion between the closely spaced O atoms in the two nearest neighbor H3 sites. The distance of 2.76 Å corresponds to the atomic spacing of the (2×1) structure along the [1$\overline{1}$1] direction and has a sizeable attractive value of -44 meV. The real space representation of the final figure set and the corresponding interaction energies are explicitly given in appendix A. Figure 4.6 shows also the figures which have been chosen by Vattulainen et al. [99]. Their set consisted of four pair interactions and two triple interactions which differed in geometry, but are given the same interaction energies. Agreement to the figure set in this work is only found for the pair interaction at d=2.76 Å, and the first triple interaction (denoted by tripleA).

Models with similar interaction energies are applied by a number of other authors [29, 103, 60, 112] and are shown in figure 4.7. All these models use a smaller number of interaction energies than the one of reference [99]. A detailed comparison reveals that the models of Vattulainen et al. [99], Williams et al. [103] and Ertl et al. [29] only use one H3 sublattice for the description of their energetics. Furthermore, for example the model of Ertl et al. is not able to treat the symmetry within the sublattice, since for their smallest pair interactions in one of the in-plane directions a positive and in a symmetry equivalent direction the same negative interaction energy is assumed. A similar model also disregarding the symmetry is used by Lu et al. [60], but with different magnitudes of the interaction energies for the smallest pair figures. The model of Vattulainen et al. [99] is indicated again in figure 4.7. (It has already been discussed in the preceding paragraph.) The model of Williams et al. [103] uses four pair interactions on one sublattice, but this should in principle allow to model different orientations of adsorbate structures in the simulation cell. Finally, the model of Kotur et al. [112] makes use only of three parameters for the lateral interactions, but additionally it takes into account the H4 transition state energy for O atoms moving from the H3 to the H4 sublattice. Summing up, all these models have been built on an empirical basis and have only limited accuracy or/and are restricted to certain concentration ranges within the phase diagram. In the present work, the

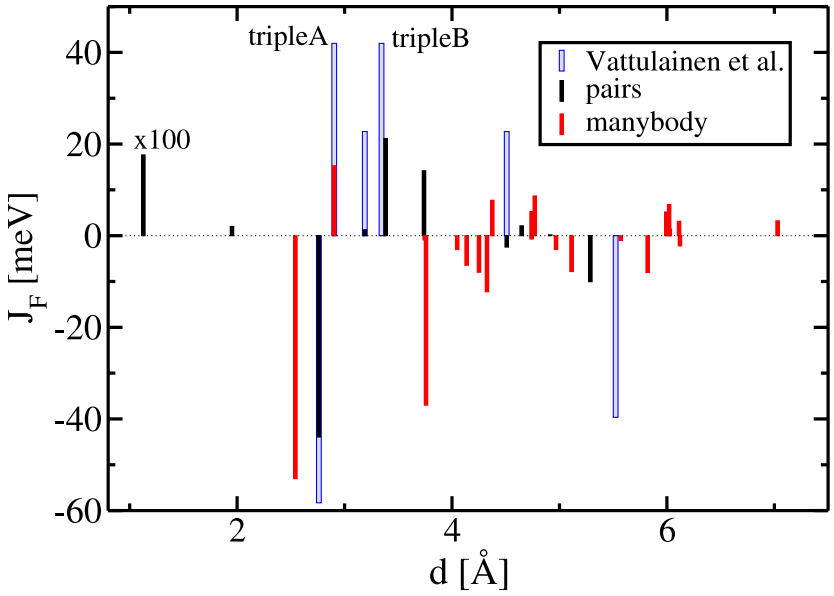

Figure 4.6: *O* adsorption on *W(110)*: Effective cluster interactions energies J_F of the cluster expansion as a function of the figure size d (for pairs: distance between the two *O* atoms; for higher-order figures: mean distance of all connections in the figure). The set of values is divided into pair interactions and higher-order (many-body) interactions. Corresponding values of Vattulainen et al. [99] are indicated, and two particular triple interactions (tripleA, tripleB) are marked: further details, see text.

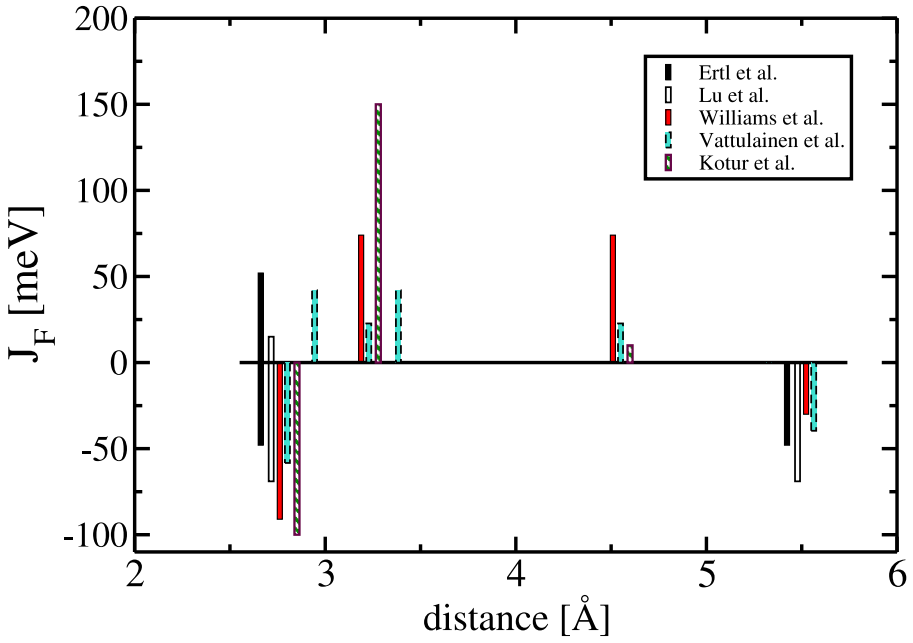

Figure 4.7: Comparison of different lattice gas models for *O* adsorption on *W(110)*. The models are taken from Ertl et al. [29], Lu et al. [60], Williams et al. [103], Vattulainen et al. [99] and Kotur et al. [112]. With the exception of the model of Vattulainen et al., which used also triple interactions, all remaining studies only used pair interactions. For details see text.

phase diagram is constructed in a truly *ab initio* manner by using DFT results in combination with the CE method and, therefore, covers the whole range of the *O* coverage.

Finally, after discussing the figure set which is used in the cluster expansion it may be noted, that other figure sets giving similar cross validation scores S_{CV} can be found. Since the genetic algorithm selects the figure sets from a large pool of figures, which are constructed by a rather fine spacing of the lattice distances (compare figure 4.1), several combinations of figures representing the energetics of a certain arrangement of adatoms may be found. Nevertheless, inspection of different final figure sets leads often to similar selections of the smallest figures, to which also similar interaction energies are attributed. Only some of the larger figures may be changing for the different figure sets.

4.6 Oxygen-Oxygen Effective Potential

Having determined the interaction energies of the CE in section 4.4 they can now be applied for studying different properties of the *O/W(110)* system. In section 4.8 the ordering behavior at finite temperatures will be discussed. This section deals with a simple model which describes the effective *O*-*O* interaction potential within the surface plane. For constructing this potential a (100×100) lateral unit cell containing two *O* atoms is set up. The surface formation energy of the configurations is calculated only by using the effective cluster interactions of section 4.4. The interatomic distance of the two *O* atoms is chosen in such a way that each possible distance according to the considered lattice of the CE is realized (see figure 4.1 (a) for the smallest distances that can be found in the lattice setup of the CE). In figure 4.8 the surface formation energy of the two *O* atoms is plotted against their interatomic distance *d*. Since the surface formation energy E_{surf} is calculated at a coverage $x_O = 2/10000$ only very small values between -0.05 meV/(1×1) and 0.80 meV/(1×1) are found. For the smallest distance of 1.13 Å the surface formation energy is 0.803 meV/(1×1) showing the repulsive character of the interaction energies mentioned already before. Also at distances of 3.74 Å and 5.64 Å a positive energy of 0.056 meV/(1×1) and 0.013 meV/(1×1) is found. Besides the positive maxima also different ranges of distances with negative energies can be realized. For the distances from 1.95 Å up to 3.18 Å the minimum energy is -0.015 meV/(1×1). In the range of distances from 4.64 Å to 5.52 Å negative surface formation energies with a minimum of -0.022 meV/(1×1) occur. For distances larger than 5.86 Å the surface formation energy converges to a constant value of -0.017 meV/(1×1) with exception of the energy of -0.033 meV/(1×1) at a distance of 7.89 Å. Different other sets of final interaction energies are used to re-calculate the *O*-*O* pair formation energies. For these different sets the shape of the curve in figure 4.8 is reproduced. Only the negative value at 7.89 Å is in most cases found to be of smaller magnitude than -0.033 meV/(1×1). As a consequence, the feature at 7.89 Å is attributed to a certain figure selection and can be understood as an artefact of the cluster expansion. For the rest of the curve the distances with positive and negative surface formation energies reproduces the features of the structures as used as input data for the CE. This observation explains, why certain distances correspond to repulsive energies, because this behavior reflects structural details which are not favored by any of the structures, especially of the ground states. These features can obviously not be explained by the ten fitted pair effective interaction energies of the CE, which are also plotted in figure 4.8 (the energy scale on the right hand side should be used, see also tables A.1 and A.2 in appendix A). For the available distances the pair energies

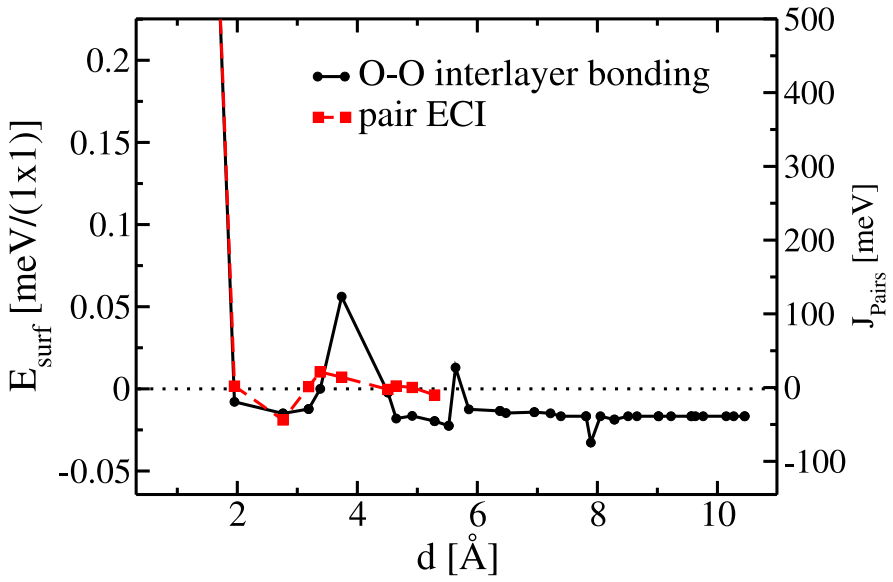

Figure 4.8: Surface formation energy for two adsorbed O atoms within a (100×100) unit cell. For calculating the energies the effective interaction energies of the cluster expansion of section 4.4 are used. The two O atoms are arranged in such a way, that all possible distances as defined by the CE are reproduced. For comparison, also the involved ten effective pair interaction energies are indicated, showing that for the calculation of the surface formation energy, all fitted interaction energies have to be considered. For details see text.

can have both positive and negative values, but the sign is not always equal to that of the energy of the two O atoms. In order to quantify the O-O energy correctly all interaction energies have to be taken into account. In other words quantification of the adsorption energies of certain structures is not possible by using simple arguments of a few figures. Only consideration of all fitted interaction energies results in the correct energy of the structure, and thus includes all structural features of the given configuration. Anyway, the O-O energies found in figure 4.8 could not be totally be correct, since no accurate DFT input for the considered structures exists, which could be included for the determination of the interaction energies. For a comparison of this simple model to DFT data, calculations with lateral unit cells much larger than that used for the present CE are needed. Such very costly or even prohibitive calculations would go beyond the scope of the present work.

4.7 Structural Details of the Ground States

The atomic structures of the four ground states are sketched in figure 4.9. For a coverage corresponding to $x_O = 0.20$ the ground state structure is defined by a (2×5) unit cell, in which the O atoms are placed on sites of both H3 sublattices. The surface energy according to equation 4.2 is -62.3 meV/(1×1) with a minimum O-O distance of 5.52 Å. When the coverage is slightly increased to $x_O = 0.25$ the (2×2)(a) structure occurs with a surface formation energy of -76.2 meV/(1×1). The minimum O-O distance is the same as for the (2×5) structure. Now the O atoms occupy only one type of H3 sublattice, as it is also the case for the two ground states with higher coverages. The lowest surface energy of -144.3 meV/(1×1) is obtained for the (2×1) structure for a coverage of $x_O = 0.50$. There, the minimum O-O distance is reduced by a factor of 2 to 2.76 Å. Finally, at $x_O = 0.75$ the (2×2)(b) structure is found with a surface formation energy of -110.3 meV/(1×1) and also a minimum O-O distance of 2.76 Å.

Since the absolute values for the stabilization energy ΔE_{stab} (see section 4.4) of the (2×5) and (2×2)(a) states are very small, these states were recalculated with higher accuracy by increasing the basis size (i.e. energy cutoff up to 500 eV) and the number of k-points for the Brillouin zone integration. The ground state line in figure 4.9 is reconfirmed, because no significant change is found in comparison to the less accurate calculations. Furthermore, the very good agreement between DFT and CE concerning surface formation energies and for finding the same ground state line gives a strong confidence to the methodology applied in the present work.

Table 4.2 summarizes the results for the mean layer distances $\overline{d}_{i-j}$ and the layer corrugations c_i. The average height of the O overlayer above the first W layer is about 1.2 Å, and it is shortest for the (2×1) phase, namely $\overline{d}_{O-1}$=1.19 Å. The layer distances between the first and second W layer show a direct dependence on O coverage. Increasing the coverage increases also the interlayer spacing $\overline{d}_{1-2}$ from 2.19 Å for the (2×5) structure up to 2.25 Å for the full (1×1) coverage. This distance is only -0.1 % smaller than the ideal bulk layer W-W distance in the [110] direction. Layer corrugation c_i (i.e. deviation from the averaged layer distance) is also listed in table 4.2. Since the (2×2)(a), (2×1) and (1×1) structures have only one O atom per primitive unit cell, there is no top layer corrugation. This restriction is lifted by performing DFT calculations for multiples of these unit cells with reduced symmetry. However, even then no significant corrugation (< 0.0005 Å) could be derived. The corrugation of the first W layer, c_1 has its maximum value of 0.13 Å for the (2×2)(a) structure whereas it is lowest for the (2×1) phase, namely 0.06 Å. The second layer corrugation c_2 is rather

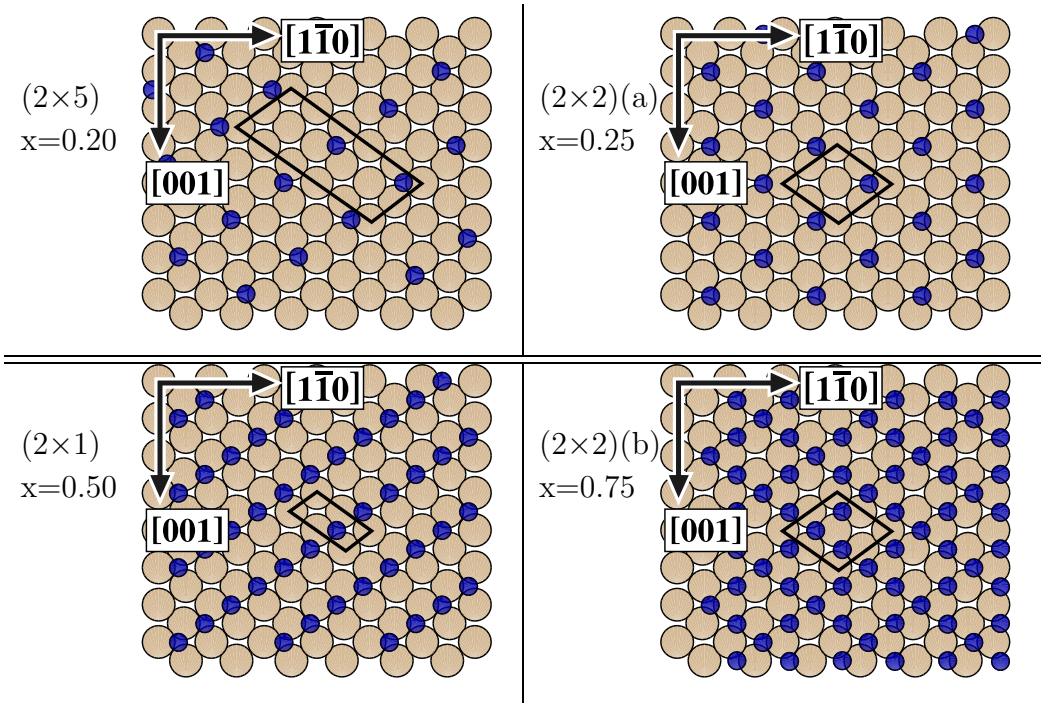

Figure 4.9: Atomic structure of the four ground states of the *O/W(110)* system. The most stable structures are (2×1) for $x_O = 0.50$ (stabilization energy $\Delta E_{stab} = -51.1$ meV/(1×1)) and (2×2)(b) for $x_O = 0.75$ ($\Delta Estab = -38.1$ meV/(1×1)). The low coverage structure, (2×5) and (2×2)(a) are only very weakly stable. More details, see text.

Table 4.2: Average layer distances $\overline{d}$ (in Å) for the adsorption ground states of O on *W(110)*. Distance $\overline{d}_{O-1}$ of the O layer to the surface W layer, distances $\overline{d}_{1-2}$ and $\overline{d}_{2-3}$ of the corresponding distances of W layers. The bulk layer distance is 2.25 Å. Layer corrugations c_i (in Å) are also listed.

	single	(2×5)	(2×2)(a)	(2×1)	(2×2)(b)	(1×1)
$\overline{d}_{O-1}$	1.23	1.22	1.21	1.19	1.20	1.21
$\overline{d}_{1-2}$	2.18	2.19	2.20	2.22	2.24	2.25
$\overline{d}_{2-3}$	2.27	2.26	2.27	2.26	2.27	2.27
c_O	–	0.00	–	–	0.03	–
c_1	0.07	0.12	0.13	0.06	0.07	–
c_2	0.02	0.05	0.05	0.04	0.06	–

constant: it takes values of 0.04 Å up to 0.06 Å. For both, layer relaxation as well as corrugation the values of deeper layers reach rather the bulk values of 2.25 Å and 0, respectively.

Details of the atomic structures from experimental studies are only reported for the (2×1) [97] and (1×1) [20, 110] phases. For the (2×1) structure the reported O-W interlayer distance is 1.25 ± 0.1 Å in agreement with the findings in the present work. For the (1×1) structure direct evaluation of full solid-angle XPD results in an O-W interlayer distance of 1.1 Å [20], but further theoretical analysis of the same data yielded a distance of 0.84 Å. Ynzunza et al. [110] report an interlayer distance of 0.91 Å as derived from full solid angle photoelectron diffraction measurements. These findings are not in agreement to the result of 1.21 Å of the present study.

For the present purpose, lateral displacements are defined by the changes of the center of mass relative to the unrelaxed structure. In general, it is observed, that in the presence of O the first and second atomic layer of W experience a net lateral shift. Table 4.3 lists the lateral shifts for the adsorbate O and the first surface W layer. The displacement along the [001] direction is rather negligible with the exception of the (2×1) structure: the O layer is shifted by -0.054 Å, whereas the W surface layer is slightly shifted into the opposite direction. Along the $[1\overline{1}0]$ direction the O layer experiences positive displacements for the (2×2) and (2×1) structures, and negative ones for the fully covered (1×1) phase. Due to symmetry, for the (2×5) structure no net displacement is found.

For the first W-layer a clear coverage dependence is found. The higher the coverage the greater is the displacement in $[1\overline{1}0]$ direction, and it reaches a sizeable

Table 4.3: Lateral shifts of the center of gravity for the ground state structures. The displacements $\Delta[1\bar{1}0]$ and $\Delta[001]$ (in Å) along the corresponding directions are given relative to the ideal unrelaxed structures. O: oxygen layer, W_1: tungsten surface layer.

	layer	$\Delta[1\bar{1}0]$	$\Delta[001]$
single	O	0.088	0.000
	W_1	-0.001	0.000
(2×5)	O	0.000	0.000
	W_1	0.000	0.000
(2×2)a	O	0.027	0.000
	W_1	-0.003	0.000
(2×1)	O	0.036	-0.054
	W_1	-0.018	0.006
(2×2)b	O	0.009	0.000
	W_1	-0.015	0.000
(1×1)	O	-0.017	0.000
	W_1	-0.095	0.000

value of -0.095 Å for the (1×1) phase. The second W-layer (not shown) is shifted into the same direction as the first one, and the magnitude of the displacement is also increasing with coverage, but the absolute values are smaller by a factor of about ten.

For a more detailed view of the lateral displacements the individual displacements of the single atoms are sketched for the ground state structures in figures 4.10 and 4.11. The absolute values of the displacements are in general larger than the shift in the center of gravity as shown in table 4.3, since the atoms move into different directions laterally. For the (2×5) ground state (see figure 4.10 (a)) the first O atom with label "1" is moved by 0.072 Å along the $[1\bar{1}0]$ and 0.001 Å along the [001] direction (for convenience, from now on the displacements will be given in the usual coordinate notation ($\Delta[1\bar{1}0]/\Delta[001]$) using Å as unit). Due to symmetry of the (2×5) unit cell the second O atom "2" is displaced exactly by the negative vector of "1". This symmetry is also found for the W atoms in the first layer. Atoms "A" to "E" are moved into the opposite direction of "J" to "F". Considering the displacements of the atoms next to "1" it becomes clear, that the relatively small displacement of "D" by (0.004/-0.017) and the somewhat larger displacements of "I" and "J" by (0.085/-0.012) and (0.026/-0.002) increase

their mutual distance and hence increase the space for the *O* atom. Analogous, this is also true for atoms "G","B" and "A". Additionally, in areas where no *O* atoms are present the mutual distance of the *W* atoms is decreased. Atoms "E" and "F" are moved towards each other by (0.110/0.033) and (-0.110/-0.033) decreasing their interatomic distance by 0.23 Å. Atoms with label "H" are moved by (-0.010/-0.019) towards "I" and "C" symmetrically by (0.010/0.019) towards "B". Similar mechanisms are also found in case of the (2×2) (a) structure as shown in figure 4.10 (b). Atoms "A" and "D" are moved by (-0.005/-0.004) and (-0.005/0.004) into the opposite direction of the *O* adatom "1", whereas "C" is moved into the same direction as "1" but more than twice as much by 0.076 Å. The areas with no *O* atoms –along the $[1\overline{1}\overline{1}]$ direction and enclosed by the straight lines which are defined by the rows of "DC" and "AB" atoms– are compressed. This also holds for the *O* free area along the $[1\overline{1}1]$ direction between the "DB" and "CA" lines. It has already been mentioned before that for the (2×1) structure the net displacement of the first *W* layer is in the negative $[1\overline{1}0]$ direction. This becomes clear now since the atom labeled with "C" and "D" are displaced by 0.043 Å and the atoms labeled "A" and "B" by 0.115 Å into the opposite direction (see figure 4.11 (a)). This effect widens the row with adsorbed *O* atoms along $[1\overline{1}\overline{1}]$ and at the same time narrows the distances in the unoccupied row of *W* atoms. In case of the (2×2)(b) structure in figure 4.11 (b) only an area surrounded by the atoms "CDBA" is free of an adsorbate atom. There, the *W* atoms are more closely packed. Since the *O* coverage is already very high, the only possibility for the adlayer to reduce strain is to buckle by 0.03 Å as discussed previously.

Finally, the different bond lengths of the *O* atoms to neighboring *W* atoms is considered. Table 4.4 lists the data according to the following arrangement: for each *O* atom first the bond length to the closest *W* atom along the $[1\overline{1}0]$ or $[\overline{1}10]$ direction is given. Then the distances to the closest *W* atoms along the [001] and $[00\overline{1}]$ directions are given. If no restrictions due to symmetry are made, as for the (2×2)(a) structure, the bond lengths for one specific *O* atom to all three neighboring atoms is never the same. In case of the (2×5) the distance to "J" (respectively "A") is slightly smaller than that to "D" ("G" respectively), but within the accuracy of table 4.4 they appear the same. The distances for the first atom is for lower coverage $\approx$ 2.1 Å and decreases with increasing coverage to 2.026 Å. The bond length to the other two *W* atoms behaves in the other way round: with increasing coverage the bond length is increasing from 2.067 Å for the (2×5) structure up to 2.121 Å, and to 2.083 Å for the (2×2)(b) structure. Only for the (2×1) structure experimental data for the *O*-*W* bond length is available. Van Hove et al. [97] report an *O*-*W* bond length of 2.08 ± 0.07 Å, which is in

(a)

(2×5)

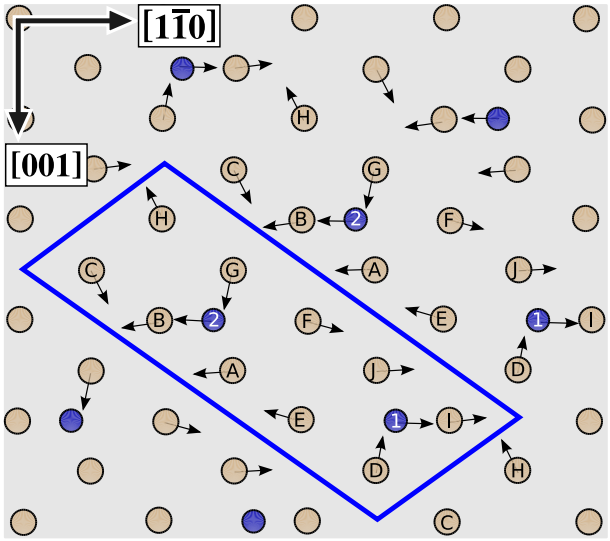

#	Δ[1$\bar{1}$0]	Δ[001]
1	0.072	0.001
2	-0.072	-0.001
A	-0.026	0.002
B	-0.085	0.012
C	0.010	0.019
D	0.004	-0.017
E	-0.110	-0.033
F	0.110	0.033
G	-0.004	0.017
H	-0.010	-0.019
I	0.085	-0.012
J	0.026	-0.002

(b)

(2×2)(a)

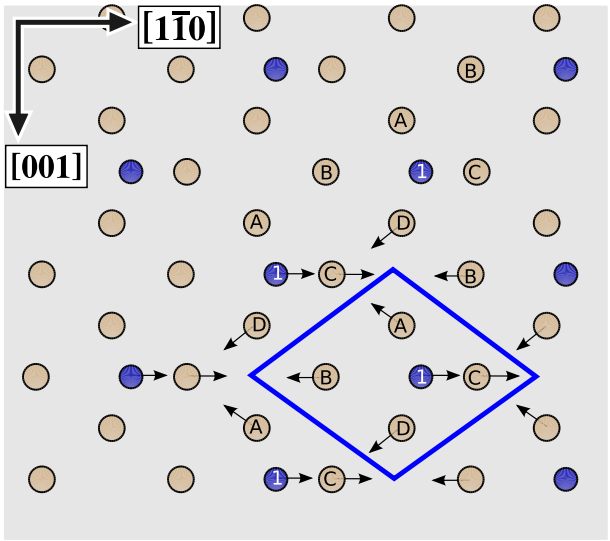

#	Δ[1$\bar{1}$0]	Δ[001]
1	0.027	0.000
A	-0.005	-0.004
B	-0.114	0.000
C	0.076	0.000
D	-0.005	0.004

Figure 4.10: Lateral displacements of individual atoms of the (2×5) and (2×2)(a) ground state structures of *O* on *W(110)* (in Å). A to J: *W* atoms in the surface layer; 1,2: *O* adlayer atoms, according to figure 4.9. Vectors drawn indicate the displacements, the listed values of Δ represent the displacements into [1$\bar{1}$0] and [001] direction separately.

(a)

(2×1)

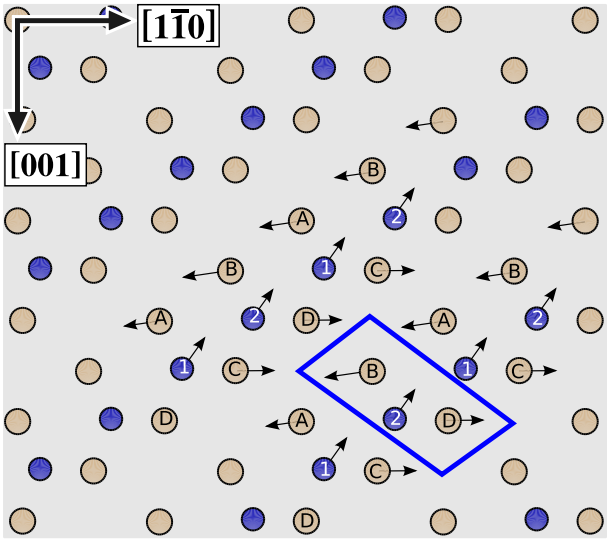

#	Δ[1$\bar{1}$0]	Δ[001]
1,2	0.036	-0.055
A,B	-0.115	0.025
C,D	0.043	-0.001

(b)

(2×2)(b)

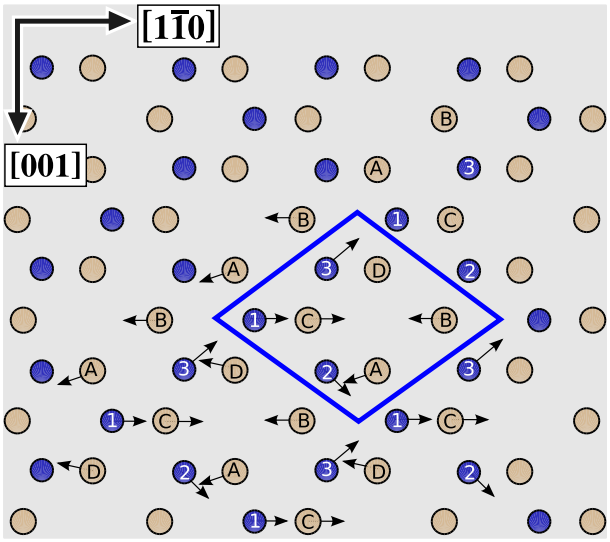

#	Δ[1$\bar{1}$0]	Δ[001]
1	0.012	0.000
2	0.036	0.031
3	0.036	-0.031
A	-0.045	0.011
B	-0.174	0.000
C	0.0175	0.000
D	-0.045	-0.011

Figure 4.11: Lateral displacements of individual atoms of the (2×1) and (2×2)(b) ground state structures of *O* on *W(110)* (in Å). A to D: *W* atoms in the surface layer; 1 to 3: *O* adlayer atoms, according to figure 4.9. Vectors drawn indicate the displacements, the listed values of Δ represent the displacements into [1$\bar{1}$0] and [001] direction separately.

Table 4.4: Bond lengths (in Å) of the *O* atoms (Arabic numbers) to the neighboring *W* atoms (alphabetic characters) in the ground state structures of the *O/W(110)* system. The order of *W* atoms is always starting with the *W* atom sitting closest along the $[1\bar{1}0]$ or $[\bar{1}10]$ direction, then the atoms closest in [001] and $[00\bar{1}]$ are given. In case of the (2×1) structure the distances of the *O* atom "1" are given to *W* atoms "C", "A" and "D", those of "2" to the atoms "D", "B", "C". For details see text.

(2×2)(a)		
1	C	2.120
	A	2.066
	D	2.066

(2×1)		
1,2	C,D	2.056
	A,B	2.070
	D,C	2.091

(2×5)		
1	I	2.100
	J	2.067
	D	2.067
2	B	2.100
	A	2.067
	G	2.067

(2×2)(b)		
1	C	2.038
	A	2.079
	D	2.079
2	A	2.026
	C	2.083
	B	2.121
3	D	2.026
	B	2.121
	C	2.083

very good agreement agreement with the values of the present study, ranging form 2.056 Å up to 2.091 Å.

4.8 Monte Carlo Simulations and Phase Diagram

Using the CE interaction energies Monte Carlo (MC) simulations for canonical ensembles were performed. For doing MC studies a simulated annealing approach was used. Each MC run started at 10000 K, and the system was then subsequently cooled down to lower temperatures. In order to rule out possible hysteresis effects also reversed runs starting from well below critical tempera-

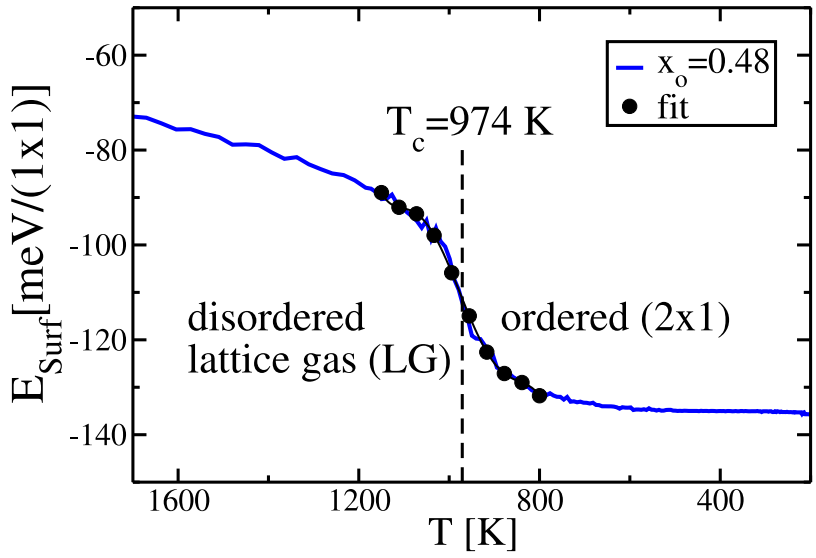

Figure 4.12: Canonical Monte Carlo simulation of the *O/W(110)* surface for an O coverage of $x_O = 0.48$.

tures above 1000 K were undertaken. As a result it was found that the critical temperatures do not change significantly when heating up the system instead of cooling it down. The size of the simulation cell was chosen to be of (100×100) atoms, i.e. 2×100×100 lattice sites with periodic boundary conditions. Figure 4.12 shows the surface formation energy for an O coverage of $x_O = 0.48$ versus simulation temperature. When decreasing the temperature the surface formation energy changes from ≈ -80 meV/(1×1) to ≈ -130 meV/(1×1) with a critical temperature of $T_c = 974$ K: at this temperature the temperature dependent surface energy $E_{surf}(T)$ has an inflection point. (For an accurate determination of the critical temperature $E_{surf}(T)$ is fitted to a polynom). It is noted, that the same critical temperature is obtained when a fit to the temperature dependent order parameter is done. Figure 4.13 shows the energy curves for six further coverages. The qualitative shapes are similar but the curves become very flat for low and high coverages, because then the gain in ordering energy is small.

For constructing the complete phase diagram the MC procedure is repeated for 25 different coverages. The result is plotted in figure 4.15 in terms of a phase diagram. Up to an O coverage of $x_O = 0.28$ the critical temperature T_c is increasing slowly from 257 K to 357 K. Further increase of the coverage by

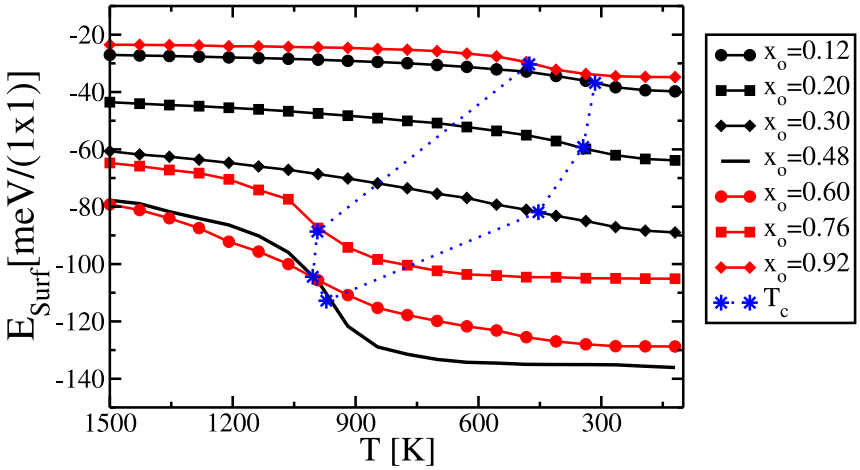

Figure 4.13: Monte Carlo simulation based on cluster expansion interaction energies for *O* on *W(110)*. Surface energy vs. temperature for various *O* coverages for a canonical ensemble of 2×100×100 lattice sites. Critical temperatures T_c (i.e. inflection points of $E_{surf}(T)$) are connected by dashed lines.

$\Delta x_O = 0.02$ results in a steep increase of T_c to 457 K, and a further increase to 971 K at a coverage of $x_O = 0.48$. Up to a coverage of $x_O = 0.75$ the disorder-order transition temperature of $\approx$ 1000 K remains rather constant. For high coverages larger than x_O=0.75 the critical temperature decreases linearly down to 380 K for $x_O = 0.98$.

In the ordering regime below T_c different mixtures of ground states are found. At low coverages up to $x_O = 0.16$ the ordering corresponds to the growth of the (2×5) structure. For higher coverages the (2×5) character is gradually lost and becoming mixed up with (2×2)(a) phases. At coverages of $x_O \approx 0.24$ small areas covered by (2×1) structure can already be observed. Up to a coverage of $x_O = 0.50$ the (2×1) structure coexists with the (2×2)(a) phase at low temperatures, and at higher temperatures (above 500 K) the (2×1) phase coexists with the disordered lattice gas. The transition is found to be gradually and thus the transition region can only be sketched in an approximate way (horizontally striped area). At x_O=0.50 at low temperatures a highly ordered (2×1) structure with large islands forms. Increasing the temperature decreases the island size and, consequently, the order. The by far predominant structure is the (2×1) phase, but also small areas of (2×2)(b) and disordered lattice gas can be found (vertically striped area at $x_O = 0.50$). Adding more *O* to this phase, also the

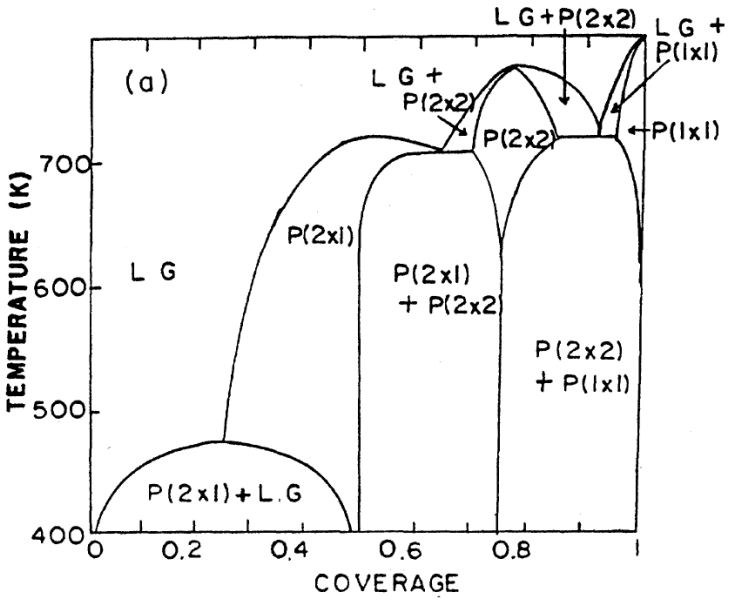

Figure 4.14: Experimental phase diagram of *O* adsorption on *W(110)* after reference [107].

(2×2)(b) appears now. As for the (2×1) case, at low temperatures the (2×1) and (2×2)(b) phases form separated areas on the surface. At a coverage of $x_O = 0.75$ the (2×2)(b) pattern appears at low temperatures. At higher temperatures also (1×1) and (2×1) patches appear (vertically striped area at $x_O = 0.75$). Finally for high coverages $x_O > 0.75$ a mixture of (2×2)(b) and (1×1) phases appear. For high temperatures the continuous areas of (2×2)(b) and (1×1) are small and grow with decreasing temperature.

An experimental phase diagram was first constructed by Wang et al. [102] on the basis of low energy electron diffraction (LEED) measurements for the full coverage range $0 \leq x_O \leq 1$. This study provided the order-disorder transition temperature and the existence regions of the different ordered structures. In a later work the phase diagram has been refined by several authors [54, 106] by adding more complicated coexistence regions at higher temperatures. Figure 4.14 shows the resulting experimental phase diagram of Wu et al. [107]. The theoretical phase diagram, to which the reader is usually referred to, is based on an adsorption study of hydrogen on *W(110)* with a lattice gas Hamiltonian consisting of four pair and two triplet interactions [96]. In this study for *H/W(110)* the ratios of the interaction energies have been found to be similar to those given by Ching et al. [15] for *O/W(110)*. In the original work of Ching the inter-

action energies are constructed by considerations of the grand potential of the known adsorption structures (1×1), (2×1), (2×2) and by a fit to LEED data at $x_O = 0.25$, 0.50, 0.75. Vattulainen et al. [98, 99, 100] used this model by fitting the interaction energies in such a way, that the experimental transition temperature $T_c = 710$ K at $x_O = 0.45$ according to Wang et al. [102] is reproduced. The resulting interaction energies are shown in figure 4.6. Also based on the model of reference [15] is the phase diagram constructed by Rikvold et al. [81]. There again, the interaction energies are chosen to reproduce the known experimental data. Another model that uses four pair interactions up to the fourth nearest neighbor distance but setting equal the interaction for the second and third nearest neighbor (i.e. J_1, $J_2 = J_3$, J_4) is applied by Williams et al. [103]. These authors fitted the interaction parameters to the data of Lu et al. [60] at $x_O = 0.50$ and at $T_c = 730$ K. Since different sets of parameters reproduce these data, the ratio of the final parameters are determined by requiring that the transition temperature of 480 K for $x_O = 0.25$ is also reproduced. Załuska-Kotur et al. [112, 113, 114, 111] again refined the Hamiltonian of Williams at al. [103] by considering both threefold and also fourfold coordinated sublattice sites. The interaction energies are chosen to reproduce the properties of the original model of Williams et al. [103]. Finally, Ertl et al. [29] constructed a model with three pair interactions which are compared to experimental data at $x_O = 0.50$ from various authors.

All those studies, which applied only pair interactions, are not able to construct a phase diagram for the full coverage range, because without higher-order particle interactions the phase diagram will not be asymmetric with respect to $x_O = 0.50$ (see reference [15] and references therein and also reference [56]). As it is mentioned in reference [15] even for a system with only five parameters the choice of the interaction parameters is not unique. It is only possible to optimize the interactions in such a way that experimental data for a number of coverages are reproduced. The application of the CE in the present work is not hampered by such limitations, because input structures for the whole coverage range enter in the expansion and the pool of figures consists of both even and uneven figures. By such a procedure, the phase diagram for the full coverage range can be constructed truly based on an *ab initio* principles.

The present *ab initio* phase diagram agrees qualitatively rather well with the experimental diagram. There are however some significant differences: the *ab initio* critical temperature is about 150 K too low at the lower coverages and about 200 K too high at higher O coverages. According to the discussion about the construction of the experimental phase diagram it seems reasonable to assume that the experimental diagram is of limited accuracy. On the other

hand, the systematic deviations might be due to some missing physical effects not included in the present study, such as surface vibrational properties. Elbe et al. [28] observed distinct phonon modes for the disordered, (2×1) and (2×2)(b) ordered O phases on *W(110)*. The overall behavior of the energy loss spectra [28] changes between a surface coverage of $x_O \approx 0.35$ and $x_O \approx 0.6$ (see section 4.10), which is the coverage range, where the *ab initio* critical temperature rises steeply. Since the previously discussed (semi)empirical studies are derived by fitting to experimental data, these models might implicitly contain the influence of surface phonons. However, as pointed out before, this is probably only valid in the proximity of the coverage where the corresponding models are applied. Another interesting point is, that a different ordering behavior at low coverages is found. All experimental studies report the (2×1) structure as the only ground state up to a coverage of $x_O = 0.50$. This is why only mixtures of the (2×1) phase and a disordered lattice gas is reported at low coverages. However, as pointed out in the discussion of the CE, the two ground states at $x_O = 0.20$ and $x_O = 0.25$ are confirmed by elaborate DFT calculations. Although their thermodynamical stability ΔE_{stab} is small, for coverages up to $x_O = 0.50$ regions which contain mixtures of these two phases are found.

4.9 Phase Distribution of the Ground State Structures

For analyzing the phase stabilities in real space figure 4.16 shows the distribution of adsorbed O atoms for $x_O = 0.48$ above and below the critical temperature T_c. Since the CE also takes into account the repulsive interactions, two O atoms with the shortest nearest neighbor H3-H3 distances are never found. This is obvious, since the large repulsive positive energy contribution of such pairs disfavors such a configuration in a MC simulation. At T=1008 K, which is slightly above $T_c = 974$ K, the tendency of ordering is only very low, since only small areas of O atoms forming one of the ground state structures are found. A close inspection of the simulation box in figure 4.16 shows that of the 4800 available O atoms on the surface only half of them are in an ordered structure at this temperature. 46.7 % of the atoms order in a (2×1) structure, 0.8 % and 4.2 % of the atoms order in the neighboring ground states (2×2)(a) and (2×2)(b), respectively. The remaining atoms are counted as disordered, since they are not found to be in a certain ground state structure. At 940 K, which is slightly lower than T_c, O atoms form contiguous islands on one sublattice (either H3A or H3B) and the ordering within the islands is distinctively longer ranged than at $T = 1008$ K.

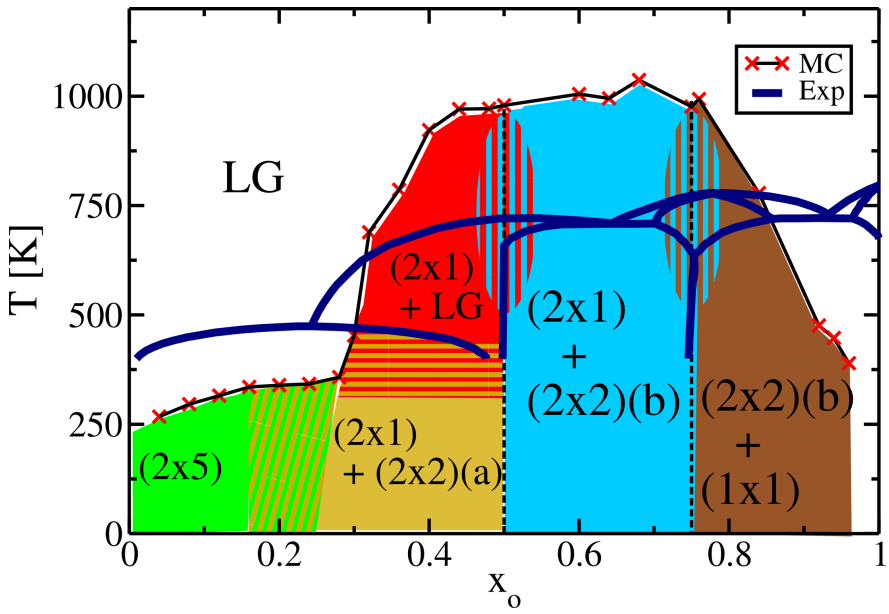

Figure 4.15: *Ab initio* phase diagram of *O* adsorption on *W(110)* derived from the Monte Carlo simulations as illustrated in figure 4.13. The actual calculated 25 points (red crosses) are connected by straight lines indicating the transition temperature T_c. Above T_c the system is in a disordered lattice-gas like state denoted by "LG". Below T_c the system orders in the structures as sketched in figure 4.9. In some areas of the phase diagram (striped areas) a clear resolution of phases is not possible, presumably because the transitions is of higher order. For more details, see text.

Now 81.1 % of the adatoms are found to order in the (2×1) structure (0.8% and 2.1% in the (2×2)(a) and (2×2)(b) structures), increasing the amount of ordered O adatoms nearly by a factor of 2. Decreasing the temperature in the simulation box in figure 4.16 further, will increase the amount of ordered O atoms.

The amount of ordered adatoms is analyzed in more detail in figure 4.17. For five temperatures (250, 500, 750, 1000 and 1250 K) the percentage of the adsorbed O atoms which order in a certain ground state structure is plotted versus the surface coverage x_O. For instance, inspecting the diagram for 250 K in figure 4.17 at $x_O = 0.16$ about 81 % of the adsorbed O atoms can be found in the (2×5) ground state. Additional 0.1 % of the O atoms are found to order in the (2×2)(a) structure. The remaining 19 % of the O atoms are in a disordered state. Next, the data at 250 K for all coverages is analyzed. Up to O coverages $x_O = 0.20$ the adatoms order predominantly in the (2×5) structure. For coverages up to $x_O = 0.50$ an increasing amount of atoms orders in the (2×1) ground state. Ordering of atoms in the (2×2)(a) structure is –due to the low thermodynamic stability of this structure– only of low importance. Not more than 7 % of the adatoms are found to order (2×2)(a)-like. At a coverage of $x_O = 0.50$ all adatoms order in the (2×1) structure. If the coverage is increased to $x_O = 0.75$, O atoms start to order in the (2×2)(b) structure in disfavor of (2×1) areas. At $x_O = 0.75$ now the ordering is completely (2×2)(b) like. For a further increase to $x_O = 1.00$ (1×1) ordering arises in disfavor of the (2×2)(b) ordering. For higher temperatures a similar behavior as for 250 K is observed but the amount of ordered adatoms is reduced in favor of the disordered phase. At $T = 500$ K the predominant (2×5) ordering at $x_O \approx 0.20$ has nearly vanished and more than 80 % of the O atoms are in a disordered state. This finding is in agreement with the order-disorder transition at around 350 K for low O coverages. At 750 K no adatoms order in the (2×5) structure any more and only small amounts of atoms order in the (2×2)(a) structure. The predominant ordering of the adatoms in the (2×1), (2×2)(b) and (1×1) structures at coverages $x_O = 0.50$, 0.75 and 1.00, respectively, is found up to temperatures of 750 K. At $T = 1000$ K, which is higher than most of the critical temperatures found in the present simulations, the maximum amount of ordered atoms in the (2×1) and the (2×2)(b) structures at $x_O = 0.50$ and 0.75 is decreasing, whereas the maximum amount of (1×1) ordered atoms at full coverage is unchanged. At $T = 1250$ K (2×1) ordering is found only for a maximum of 29 % of the adatoms at $x_O = 0.60$ (slightly larger than the ideal coverage of this ground state). Also not more than 50 % of the atoms at $x_O = 0.75$ are ordering in the (2×2)(b). At high coverages $x_O > 0.75$ the amount of atoms ordering in the (1×1) structure is found to increase at all temperatures. This is clear since in the CE the atoms are forced on the lattice and

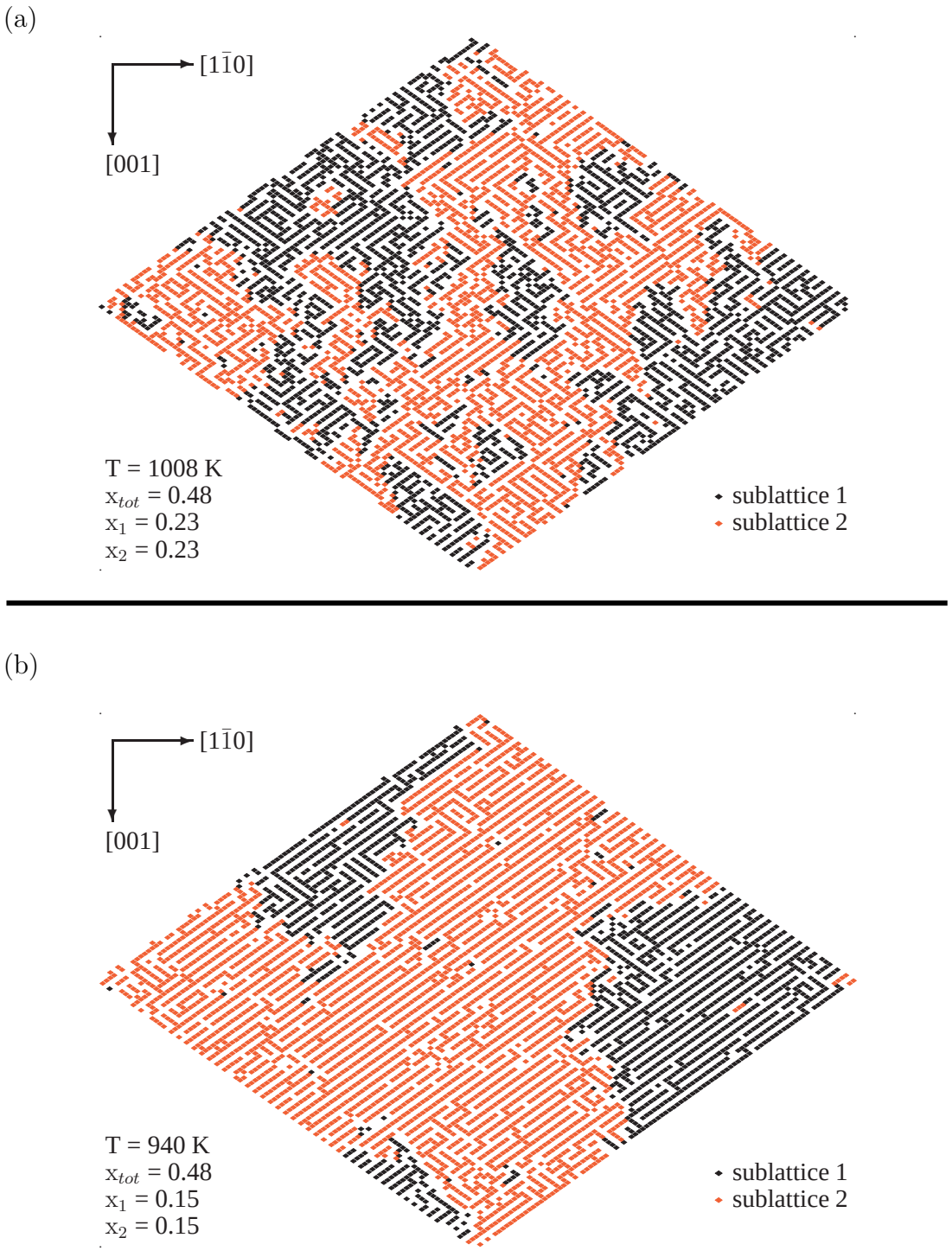

Figure 4.16: Distribution of O on 3-fold hollow adsorption sites of *W(110)* according to the Monte Carlo simulation as based on the cluster expansion. (coverage $x_O = 0.48$, critical temperature T_c=974 K). (a) for $T_c < T = 1008$ K, (b) for $T_c > T = 940$ K. Black: O atoms on sublattice sites H3A; red: O atoms on sites H3B; white: unoccupied sites.

nearly all principle adsorption sites are occupied. As a consequence the adatoms can only order in the (1×1) structure. Finally, the analysis of the change of the ordering behavior with respect to simulation temperature is in agreement with the transition temperatures found in section 4.8.

In addition to the explicit real space pictorial data as derived from the MC simulation also the ordering behavior can be analyzed, namely in terms of the short range order parameter α_{lmn}, defined in section 2.2.3. For convenience the notation lmn for a certain neighbor shell is replaced by simply an integer i indicating the number of the nearest neighbor distances as defined in the cluster expansion of figure 4.1. Figure 4.18 presents the short range order parameter α_i for the ideal ground state structures at $T = 0$ K and for the same temperatures as in figure 4.17. In the MC simulations it is found that the numerical values of α_i for some nearest neighbor distances is quite similar. That is why only a selection is printed, namely α_1, α_4, α_8 and α_{10}. From the diagram of the ideal α_i at $T = 0$ K for the ordered structures it is obvious, that a distinction between the different ground state structures can be made. For example α_{10} starts with $\alpha_{10} = 0.00$ at $x_O = 0.00$. At $x_O = 0.20$ and $x_O = 0.25$ it changes to $\alpha_{10} = -0.11$ and $\alpha_{10} = -0.14$, respectively. For coverages larger than 0.50 it turns positive, namely $\alpha_{10} = 0.33$ at $x_O = 0.50$ and $\alpha_{10} = 0.46$ at $x_O = 0.75$ and finally $\alpha_{10} = 1.00$ at $x_O = 1.00$. On the other hand, the parameter α_1 is found to be $\alpha_1 = -0.11$ at $x_O = 0.20$ decreasing to $\alpha_1 = -0.14$, -0.33, -0.60 and -1.00 at coverages $x_O = 0.25$, 0.50, 0.75, and 1.00, respectively. The parameter α_4 changes similar to α_{10} but it has $\alpha_4 = -0.33$ at a coverage of $x_O = 0.50$. Finally, the values of α_8 are nearly identical to those of α_1 except for $\alpha_8 = 0.44$ at $x_O = 0.20$ where $\alpha_1 = -0.11$ is found. Since for all coverages the ordering of the different ground state structures can be identified by the different features of α_i it is possible to analyze the amount of ordering in the MC simulation also by analyzing α_i.

At $T = 250$ K for coverages $x_O \geq 0.50$ good agreement with the ideal α_i at $T = 0$ K is found, indicating order predominantly in the ground state structures (2×1), (2×2)(b) and (1×1). For low coverages the peak of α_8 at $x_O = 0.20$ has disappeared and is replaced by a maximum of α_{10}. This can be explained by considering the short range order parameters of the (2×1) ground state, which has similar values for α_{10} and α_8 (at a coverage of $x_O = 0.50$). Already at coverages $x_O \leq 0.20$ the (2×1) ground state has some influence on the ordering behavior at 250 K. This observation agrees with the real space data of the MC simulation, since also small areas with the (2×1) ground state can be identified. At 500 K for $x_O \geq 0.50$ the parameter α_i remains in agreement with the ideal structures. For low coverages no distinctive feature of any of the ground state structures can be

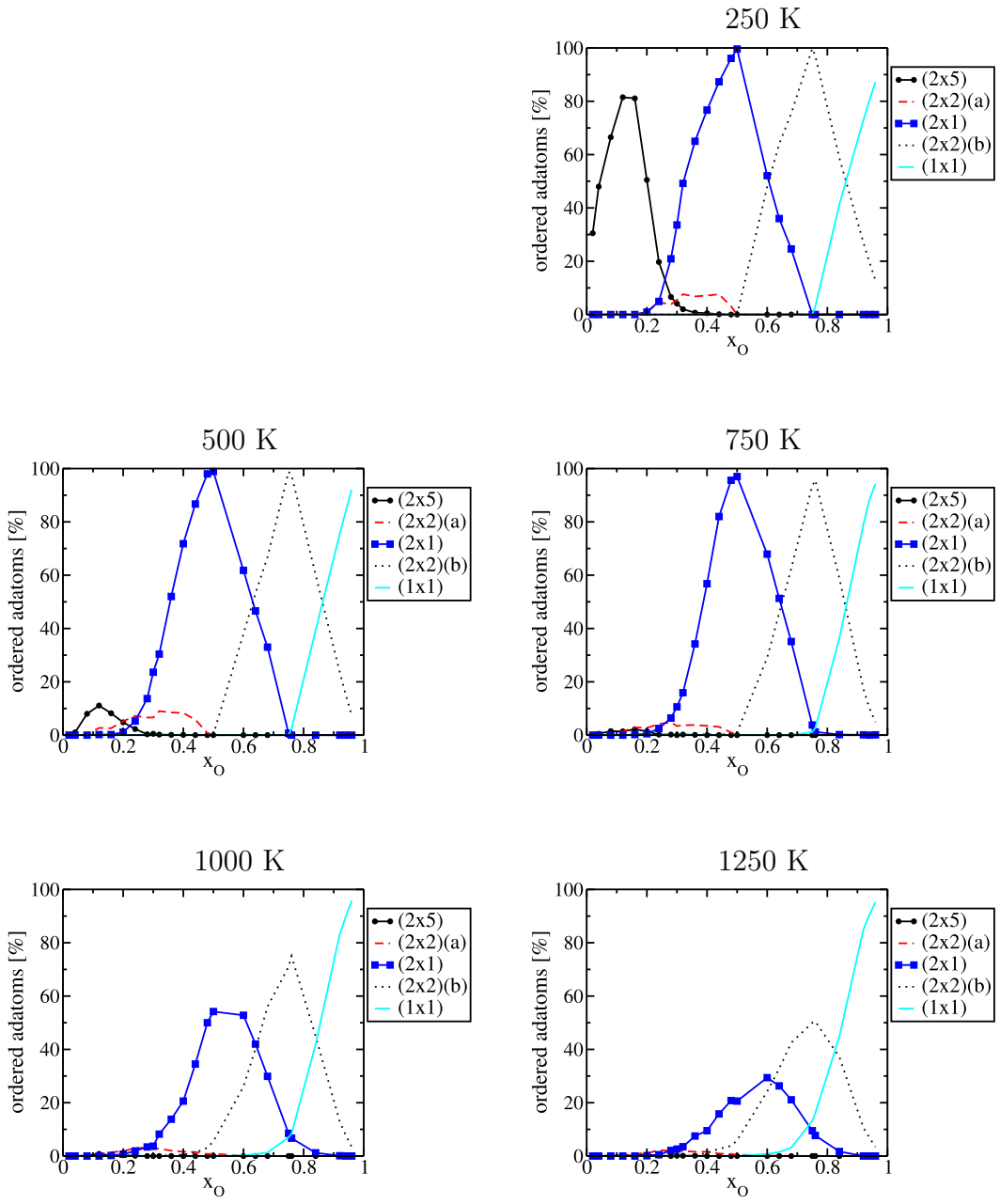

Figure 4.17: Amount of ordered *O* adatoms as derived from the Monte Carlo simulations for the *O* adsorption on *W(110)*. For different temperatures (250, 500, 750, 1000 and 1250 K) the diagrams show the percentage of *O* atoms that are found in one of the ground state structures versus the *O* coverage. The percentage of the *O* atoms is chosen with respect to the total number of available atoms, which is coverage dependent. For details see text.

Table 4.5: Surface vibrational energies of stretching (*str*) and wagging (*wag*) modes of adsorbed *O* for the four ground state structures of *O* on *W(110)*, as derived from a high energy electron loss spectroscopy (HEELS) experiment [28] and as calculated by DFT. For some modes a range of vibrational energies as indicated by ± is possible. Also shown are the calculated zero point vibration energies ZPE-DFT or $F_{vib}(T = 0)$, and the calculated temperature dependent free energy differences ΔF_{vib} with respect to the fully covered (1×1) surface. For the lowest coverage case DFT calculations are made for the (2×2)(a) structure, whereas the experimental values are assigned to a disordered lattice gas (LG). All values are given in meV.

	LG or (2×2)(a)	(2×1)	(2×2)(b)	(1×1)
str HEELS	66	72	79	82
str DFT	60	64 ± 1.3	65 ±2.0	68
wag HEELS	46	48	50	53
wag DFT [001]	47	48 ± 0.2	50 ±0.3	50
wag DFT [1$\bar{1}$0]	33	52 ± 1.4	56 ±2.9	58
ZPE-DFT	70	82	85	88
ΔF_{vib}(0 K)	-4.6	-3.3	-2.0	0
ΔF_{vib}(400 K)	-7.6	-4.8	-2.8	0
ΔF_{vib}(900 K)	-15.3	-9.2	-5.2	0

seen any more and the short range order parameters are close to $\alpha_i = 0$ indicating nearly disorder or only weak ordering behavior. This is in agreement with the findings of the order-disorder temperatures of section 4.8. At 750 K, the values of α_4 start to change significantly, since ordering in the (2×1) structure is starting to decrease. Increasing the temperature even more, all features which could be identified at low temperatures, are now lost and the curves of the α_i show no agreement with the ordering of any of the ground state structures, except for the (1×1) structure with $\alpha_i = \pm 1$ at $x_O = 1.00$.

4.10 Surface Phonons

Another possible source for the systematic deviation between calculated and experimental phase boundaries might be due to surface phonons. Elbe et al. [28] measured phonon energies for stretching and wagging modes for the disordered (LG) phase, and the (2×1), (2×2)(b) and (1×1) adsorption structures, as pre-

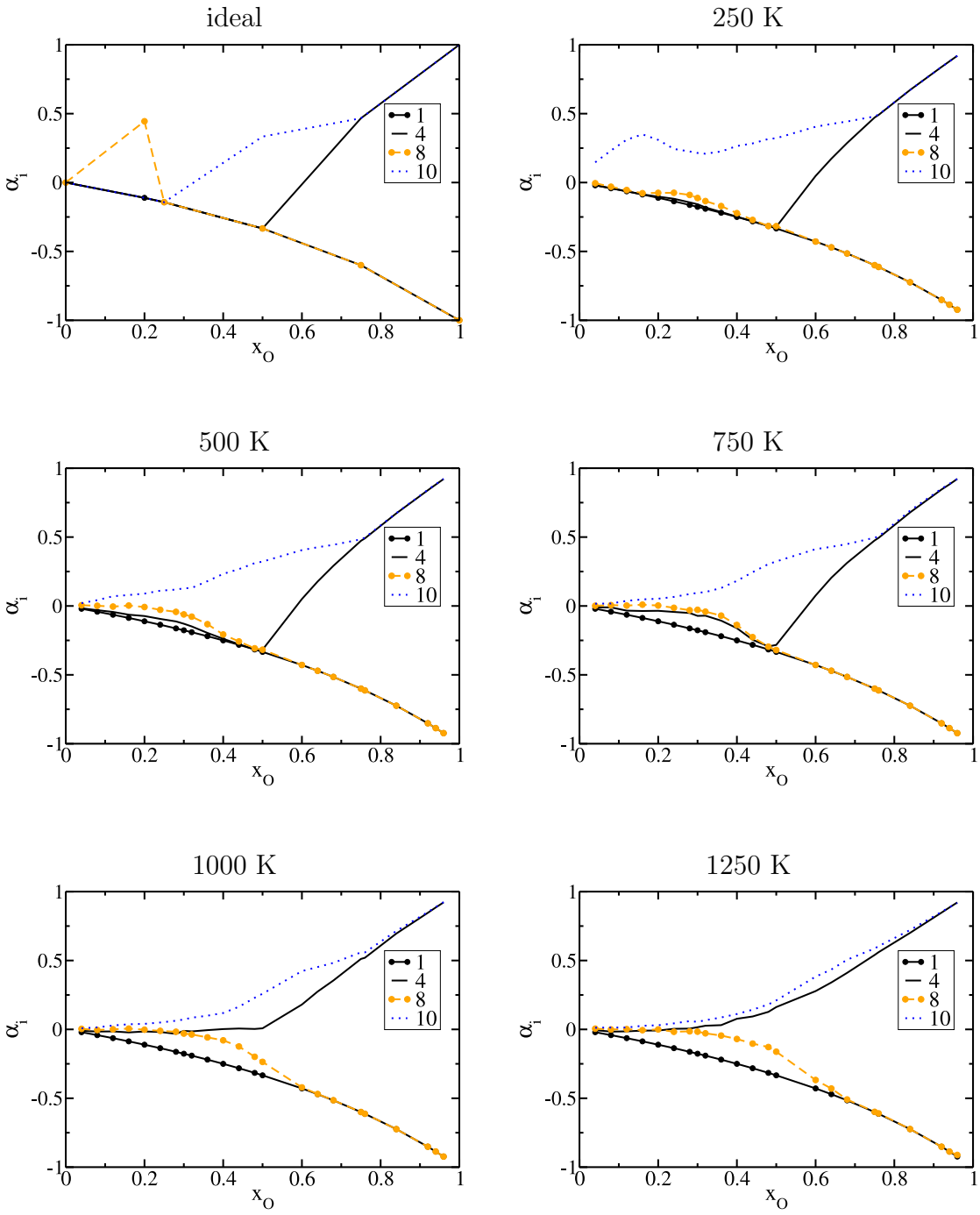

Figure 4.18: Selected short range order parameter α_i for the O adsorption on *W(110)*, with nearest neighbor distances $i = \{1, 4, 8, 10\}$ appropriate to the lattice used for the CE. The upper left diagram shows the parameters for the ideal ground states at $x_O = 0.20$, 0.25, 0.50 and 0.75 which are connected by lines. For finite temperatures the parameters are taken from the Monte Carlo simulations. For details see text.

sented in table 4.5 and figure 4.19. For the stretching mode the vibrational energy increases from 66 meV for the lattice gas up to 82 meV for the (1×1) structure. The wagging mode energy is in general lower by about 20 to 30 meV, and increases weakly from 46 meV to 53 meV. For estimating the influence of surface vibrations on the surface energy stretching and wagging modes of adsorbed *O* for the (2×2)(a),(2×1),(2×2)(b) and (1×1) structures are investigated by calculating the forces connected to suitable displacements. The corresponding results are given in table 4.5. For the principle idea of calculating the stretching modes see also section 3.3, which describes the procedure for the *O* molecule. For the stretching mode, the general experimental trend of increasing vibrational energies with increasing coverage is reproduced by the DFT calculations. The absolute DFT values, however, are lower, in general. Concerning the (2×2)(a) structure the DFT energy of 60 meV is lower by 10% whereas the difference increases with increasing coverage: for the (1×1) structure the DFT vibrational energy energy is smaller by 20% than the experimental value. The systematic underestimation of the calculated stretching energies might be due to the two-dimensional lattice parameter, which for the DFT calculation is 3.189 Å, being slightly larger than the experimental bulk lattice parameter of 3.165 Å. This difference can be attributed to the choice of a GGA exchange-correlation functional, which is known to overestimate the lattice parameters for 5d elements. On the other hand GGA had to be chosen for a correct description of the adsorption energetics.

Wagging modes are studied by displacing *O* atoms in [001] and $[1\bar{1}0]$ directions. In general, the agreement with experiment is very good with the exception of the $[1\bar{1}0]$ vibration for the (2×2)(a) structure, for which DFT yields a value of 33 meV being significantly lower than the experimental value of 46 meV assigned to the disordered LG phase (see table 4.5). It should however be noted, that in experiment no ordered low coverage (2×2)(a) phase could be identified.

In principle, temperature dependent vibrational free energies $F_{vib}(T)$ may also be derived from DFT calculations [78], which would involve a larger number of suitably large supercell calculations for deriving phonon dispersions and the phonon density of states, from which $F_{vib}(T)$ is directly determined. Considering the vibrational corrections to the surface formation energy E_{surf} of equation 2.53, free energy differences ΔF_{vib} are needed, for which F_{vib} for the fully covered (1×1) surface is the reference. The modification of the CE so that also phonon energies can be included is given in section 2.2.4.

Adopting a simple model for these corrections an Einstein-like model is assumed in which for each structure the phonon density of states is replaced by the three vibrational energies given table 4.5. Zero point energies in general (see also table 4.5) are positive values. However, the differences $\Delta F_{vib}(T = 0)$ are negative,

because the reference value of the (1×1) structure is the largest, and the lowering effect is larger the smaller the coverage is. For T > 0, vibrational entropy gains in influence and the described lowering effect is even more pronounced. Because of the lowering of the formation energies E_{surf} at all temperatures the ground state energies for all studied phases are also lowered, correspondingly. From these considerations, one can estimate the error for not including vibrational free energies, which is at least 10 meV for temperatures T > 400 K, resulting in an error of the transition temperature of about 100 K. In all ceases, the vibrational correction lowers E_{surf} and consequently favors the formation of ordered ground state structures at higher transition temperatures than without the corrections. Since the correction for lower coverages is larger, a larger increase of T_c would be expected than for the higher coverages. It should, however, be noted, that all arguments so far are based only on coverage dependent vibrational properties. In principle, temperature dependent vibrational free energies are needed for all input structures of the CE. From such an expensive approach, temperature dependent cluster interaction energies could be derived which would also enter the MC simulations (see section 2.2.4. Such a task is beyond the scope of this work. Anyhow an idea of the change in the ground state diagram can be given by figure 4.20. It shows the ground state line obtained by the CE and the phonon corrected energies of the (2×2)(a),(2×1) and (2×2)(b) ground states at 0, 400 and 900 K. Clearly the ground state line is lowered more for coverages up to $x_O = 0.50$ than at higher coverages. The previously discussed semi-empirical studies are based on fitting parameters to experimental data, and therefore they implicitly comprise the influence of surface phonons. However, as pointed out before, this is probably only valid for coverages for which the corresponding models are applied.

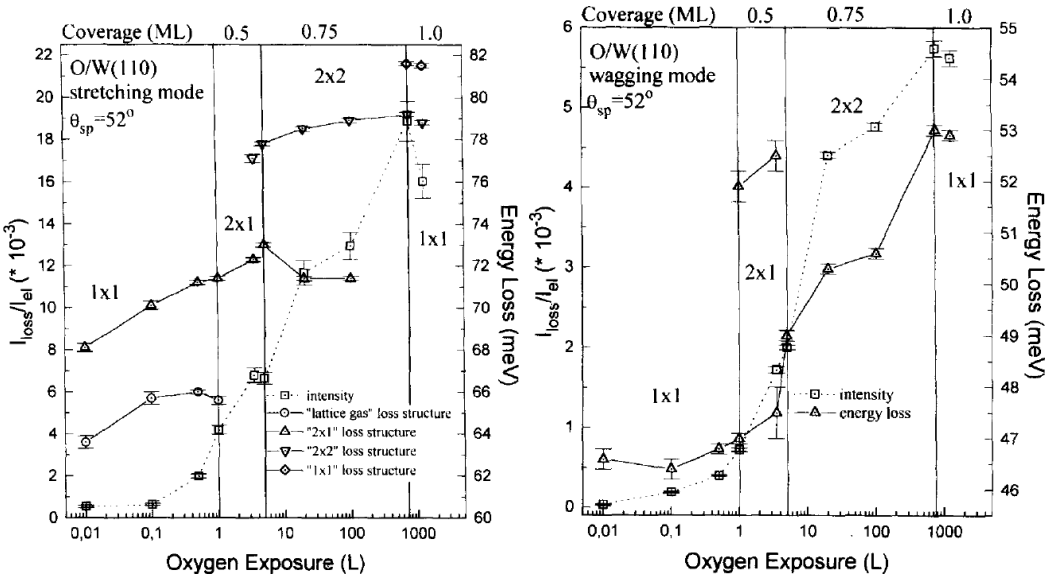

Figure 4.19: Experimental stretching and wagging modes taken from Elbe et al. [28]. The experiment shows distinctive phonon modes depending on the O surface coverage. For details see text.

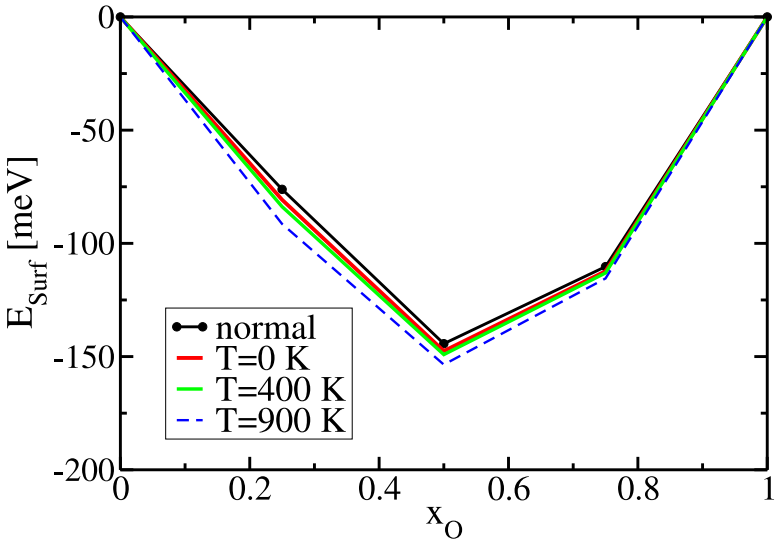

Figure 4.20: Temperature dependent surface ground state diagram. At finite temperatures the ground state line is deepened by the influence of surface phonons. For coverages up to $x_O = 0.50$ the phonon influence is greater than for higher coverages. For details see text.

5

Indium Adsorption on *W(110)*

In this chapter the adsorption of *In* on the *W(110)* surface is studied. Section 5.1 gives an overview of the system and the work that has been done by other authors. The experimental setup which has been used by the experimental colleagues at the university of Innsbruck and the computational details for the DFT calculations are presented in section 5.2. In section 5.3 the adsorption energies for *In* atoms on the different adsorption sites for single atoms and at high coverage is calculated. The observed *In* overstructures at different coverages are presented by a combination of DFT calculations and low energy electron diffraction measurements in section 5.4. Finally, the stability of the different overstructures is discussed in sections 5.5 - 5.8 by using DFT calculations in combination with molecular dynamics simulations.

5.1 Introduction

In and *W* are metals with very different physical properties. *W* has the highest melting point of all metals (3683 K) while *In* melts already at 430 K. *In* is very soft, while *W* is hard and brittle, in particular when carbon and oxygen impurities are present. Due to the softness of *In* one might expect, that *In* likes to grow on *W(110)* in a pseudomorphic manner with *In* atoms occupying the energetically most favorable single-atom adsorption sites, even if this requires some change of the *In-In* bond length as compared to bulk *In*. However, as will be shown in this chapter, this assumption does not hold due to the rather large lattice misfit: the nearest-neighbor *In-In* distance exceeds that of *W* by 19%. Furthermore, both materials adopt different crystallographic structures in their respective bulk phases as shown in sections 3.1 and 3.2. Similar to section 3.2 the fct notation to specify the crystallographic directions of *In* will always be used.

The growth of submonolayer *In* films on *W(110)* first was investigated with

low-energy electron diffraction (LEED) and work function measurements by Gorodetskii et al. [41] and Boiko [10]. In these investigations as well as in the more recent combined LEED and X-ray photoelectron spectroscopy (XPS) work of Bürgener et al. [12] several ordered structures were observed with increasing coverage upon room-temperature deposition : a (3×1) structure at low *In* coverages ($x_{In} \approx 0.20$ according to the XPS calibration of reference [12]), followed by (1×4) and (1×5) patterns at coverages of $x_{In} \approx 0.65$ and 0.80, respectively. (A coverage of $x_{In} = 1.00$ refers to the *W(110)* surface completely covered with one monolayer of *In* atoms in a (1×1) structure.) In a very recent LEED and scanning tunneling microscopy (STM) work it is reported that the (3×1) structure is only metastable [38]. Within 1 to 2 hours after deposition or upon annealing the (3×1) structure transforms irreversibly into islands with a higher coverage, rather corresponding to a (1×4) structure. This finding is in contrast to the paper of Boiko from 1990, in which the mentioned temperature-induced transition is also reported, however it is claimed that this transition is reversible. The (3×1) and (1×4) adsorption structures (denoted as γ- and α-structures) are also observed for the closely related *In/Mo(110)* adsorbate system [47].

In the investigations listed above various structure models were suggested. Whereas for the low-coverage (3×1) structure all studies agree, different models are proposed for the high-coverage (1×4) and (1×5) phases. Bürgener et al. [12, 13] suggest pseudomorphic long-bridge ("pseudo-4-fold") adsorption sites with intermittent empty rows, which are needed for the correct coverage. This empty space might be also convenient for reducing the compressive stress in the *In* overlayer due to the compact packing into pseudomorphic sites. However, Boiko [10] as well as Gabl et al. [38] favored a more uniform distribution of the *In* adatoms, which resembles a Moire-like structure of *In(111)* on *W(110)*. In all these studies, the proposed structure models are based on visual inspections of LEED patterns only, without any quantitative analysis of the diffraction intensities. The purpose of the present work is to study these structures in a more accurate way, experimentally by a LEED I/V analysis, which has been done by Martin Gabl and Norbert Memmel in the group of Erminald Bertel at the university of Innsbruck, as well as theoretically in terms of *ab-initio* density functional theory (DFT) calculations [91]. Furthermore, since DFT calculations also provide adsorption energies, it is also possible to address the stability or metastability of the various adsorbate structures for different coverages. Since this part of the work is done in close collaboration with an experimental group, all results in the following sections will be presented together with the experimental findings in order to demonstrate the good agreement between theory and experiment and the necessity of a close collaboration between theory and experiment.

5.2 Experimental Setup & Computational Details

The experiments where performed in an UHV chamber under a base pressure of $1{\cdot}10^{-10}$ mbar equipped with standard facilities for sample preparation and a Video-LEED system (ErLEED, Specs GmbH). The *W(110)* surface is cleaned by annealing in $5{\cdot}10^{-8}$ mbar of oxygen at 1550 K, followed by a flash to 2300 K. The temperature is monitored with an infrared pyrometer through a ZnSe window with an accuracy of about ±20 K. Surface cleanliness is verified by LEED and Auger-electron spectroscopy.

In is evaporated from a Knudsen cell with a resistively heated boron-nitride crucible using deposition rates and sample temperatures of $\Delta x_{In} \approx 0.2$/min and $\approx$ 330 K, respectively. Normal-incidence LEED patterns are recorded at sample temperatures below 200 K in the energy range 20-500 eV by means of a 12-bit digital camera [87]. The recorded I/V spectra are normalized to the primary beam intensity. To further improve the quality of the data, spectra of symmetrically equivalent beams are averaged and slightly smoothed. For pure *W(110)* a data set of eight beams with a total energy width of 2740 eV is evaluated. For the (3×1)-*In*/ *W(110)* structure the data set consists of 9 integral and 10 fractional order beams with integrated energy widths of 2915 eV and 3595 eV, respectively, while for the (1×4) and (1×5) structures sets of 8 integral/ 10 fractional (ΔE = 2740 + 4014 eV) and 9 integral/ 9 fractional (ΔE = 2880 + 3165 eV) order beams, respectively, are used.

LEED intensities are calculated using the TensErLEED program package [8]. In the Tensor-LEED approach first a full dynamical calculation is carried out for a certain reference structure and then intensity changes due to small deviations from this reference are calculated by a perturbation scheme [85, 83, 84]. A semi-automated structural search is made by a frustrated simulated annealing procedure [50], guided by the Pendry R-factor R_P [75] for the quantitative comparison of experimental and calculated spectra. Electron attenuation is described by an energy-dependent imaginary part of the inner potential according to $V_{0i} = 6 * (Energy/230eV)^{1/3} eV$. The real part of the inner potential (defined relative to the vacuum energy), V_{0r}, is also allowed to be energy dependent according to $V_{0r} = -max(-0.03 - 77.07/\sqrt{Energy/eV + 17.79}; -10.84)eV$. 17 relativistically calculated, spin averaged phase shifts are used for *W* and *In*, respectively, as provided by reference [66]. Special care is taken not to leave the validity range of the perturbation Ansatz. This is checked by a full dynamical recalculation of the intensities for the optimized geometry.

Statistical error limits for the varied parameters are estimated by the vari-

ance of the Pendry R-factor [75], $var(R_P) = R_{P,min}\sqrt{8V_{0iP}/\Delta E}$ with $R_{P,min}$ the minimum R-factor and $V_{0i} \approx 5eV$ the average imaginary part of the inner potential as also used for the calculation of R_P. All structures with R-factors below $(R_{P,min} + var(R_P))$ are supposed to be within the limits of error. Typically errors are in the range 0.02 - 0.05 Å.

For the DFT calculations the Vienna ab initio Simulation Package (VASP) [52, 51] with the projector augmented wave implementation [6, 53] is used. The exchange correlation functional is approximated within the generalized gradient approximation (GGA) as parametrized by Perdew, Burke and Ernzerhof (PBE; this abbreviation will be used further on to indicate the calculated results) [76]. A plane wave basis set with an energy cutoff of 350 eV is used. Suitable k-point grids are constructed according to reference [68]: a 13x13x13 mesh for the primitive bulk unit cell and a 13x13x1 mesh for the surface slabs are chosen. For larger unit cells the k-point grids are scaled down accordingly. For the Brillouin zone integration the smearing method of reference [64] with a width of 0.1 eV is applied. The *In*-4d and W-5p semicore states are treated as valence states. For the geometrical relaxation the Hellman-Feynman forces are minimized within a quasi-Newton algorithm and a convergence criterion of 0.01 eV/Å is applied. Symmetric slabs with 7, 9, 11, 13 layers of W and with different vacuum spacings have been tested in order to find the optimized number of layers for the larger-scale calculations. Finally, the chosen setup for the adsorption studies is a symmetric slab with seven W-layers with *In* coverages $x_{In} = 0.33$,0.75 and 0.80. A vacuum region equivalent to 5 *W(110)* bulk layers ($\approx$ 11 Å) is added.

5.3 Adsorption Energies of *In* Atoms

In this section the adsorption energies E_{ad} for *In* atoms after equation 3.16 are calculated. The exact location of the adsorption sites was presented in section 3.4.4. As pointed out there, the adsorption energies are calculated for a (4×4) unit cell containing one *In* atom (representing the single atom limit) and a (1×1) lateral unit cell for the full covered surface. For adsorbed single *In* atoms the most favorable adsorption site is the H4 one with $E_{ad} = -2.99$ eV/atom. The next favorable site is the H3 with $E_{ad} = -2.91$ which is only metastable. Full relaxation will drive the atom towards the H4 site. Thus only if the lateral relaxation is forbidden, the value for the H3 can be calculated. The adsorption energies for single ontop and bridge atoms are lower than the H3 and H4 sites namely -2.62 and -2.75 eV/atom. For the full coverage case the hierarchy of the adsorption sites changes. The most stable adsorption site is the H3 with $E_{ad} = -2.69$ eV/atom, followed by the bridge site with $E_{ad} = -2.65$ eV/atom.

The H4 is slightly less favorable with $E_{ad} = -2.64$ eV/atom. As for the low coverage case the adsorption energy of the ontop site is the least favorable one. This is already an implication that both H3 and H4 adsorption sites are important for the adsorption structure of *In* on *W(110)*. Details of theses structures will be given later in section 5.4. Since to our knowledge there is no other *ab initio* study for this adsorption system so far, no comparison to other data can be made. In equation 3.16 replacing the total energy of a free *In* atom E_{In}^{atom} by the total energy of *In* in the bulk phase (the calculated cohesive energy of the fct *In* phase is -2.40 eV/atom) -0.59 and -0.22 eV/atom for the 4-fold hollow and on-top adsorption sites are obtained, accordingly. These negative energies indicate that *In* submonolayers wet the *W(110)* surface rather than forming three-dimensional agglomerates, which is in agreement to experiment. The lowest energy path for an isolated *In* adatom from the 4-fold site to the next similar site includes the 2-fold (short) bridge position as a saddle point. From that the diffusion barrier may be estimated as the energy difference between the 2-fold bridge and 4-fold site, resulting in a diffusion barrier of ≈ 0.24 eV.

5.4 Structural Details of the Observed Indium Overstructures

As pointed out in section 5.1 three different adsorption structures were identified in previous experiments. In this section the structural details of the (3×1), (1×4) and (1×5) *In* overstructures are discussed. For each structure the atomic coordinates found by DFT and LEED analysis are given.

(3×1)

For low coverages, a (3×1) superstructure is observed by LEED (top of figure 5.1 (b)). The LEED pattern corresponds to a real-space unit cell with unit cell vectors along the $[1\bar{1}1]$ (long side) and the $[1\bar{1}0]$ (short side) directions of the *W(110)* lattice, as shown in the lower part of the figure. XPS-studies of Bürgener et al. [12] reveal a coverage of $x_{In} \approx 0.2$ for this structure. We assume adsorption of one *In* per unit cell, which corresponds to $x_{In} = 0.33$ for a surface completely covered with this phase. Each unit cell consists of three *W* surface atoms (large grey circles) and one *In* atom (small black circles). The minimum *In-In* distance for the (3×1) structure is 4.48 Å which is significantly larger than the next neighbor distance of 3.31 Å in bulk *In*. It should be noted, that the calculated adsorption energy of -3.03 eV per *In* atom for the (3×1) structure is very close to the single *In* energy of -2.99 eV for the most stable H4 site (see table

Table 5.1: Pendry R-factors for different adsorption sites, relaxation of atomic positions is only allowed along [110] direction normal to the surface.

	4-fold hollow	3-fold hollow	bridge	on-top
R_P [all]	0.36	0.42	0.49	0.47
R_P [int]	0.24	0.25	0.32	0.31
R_P [fract.]	0.58	0.72	0.75	0.75

4.1). Consequently, the preferred adsorption sites in the (3×1) structure are the H4 sites.

In order to determine the adsorption sites from experiment, TensErLEED [8] calculations are carried out with *In* atoms in the 4 principal adsorption sites. Only relaxations of *In* and *W* atoms along the surface normal are allowed at this stage. In agreement with the theoretical predictions it is found, that the 4-fold hollow site is favored with a Pendry R-factor of 0.36. For the 3-fold-hollow, the bridge and the on-top site the R-factor amounts to 0.42, 0.49 and 0.47 (see table 5.1. Since the variance of the Pendry factor is small ($var(R_P) = 0.019$) the latter three adsorption sites can clearly be excluded. The preference for the H4 site is particularly manifested if only the superstructure-induced fractional order spots are considered ($R_P = 0.58$ versus $R_P \geq 0.72$), although the R-factors of the fractional spots are quite large on an absolute scale. Once the the adsorption sites are determined the structure is further optimized by allowing also for lateral relaxations of surface *W* atoms and by considering sub-optimal coverage (i.e. free *W* patches on the surface) which reduces the minimum Pendry R-factor to 0.28 for the 4-fold hollow site. The detailed geometry parameters as obtained from both experiment and theory are listed in table 5.2. Examples of I(E) spectra as obtained by experiment and LEED simulations are shown in figure 5.2). Both, form the experiment as well as from the calculation it is found that *In* pushes *W* atoms next to it (labeled "A" and "C" in figure 5.1 (b) slightly sidewards by 0.03 Å and also downwards by 0.02 Å. This relaxation results in shorter distances of *In* to surface *W* atoms, and therefore increases the bonding strength to the substrate.

For symmetry-reasons the *W* atom labeled "B" in figure 5.1 (b) does not shift laterally, but only relaxes normal to the surface. LEED and PBE derive an outward displacement of 0.04 Å and 0.05 Å (see table 5.2) of atom "B" which slightly reduces the distance to the next *In* adatom. The distance between the *In* adlayer and the center of the buckled surface-layer of *W(110)* amounts to 2.33 Å (LEED) and 2.35 Å (PBE). This corresponds to a contraction of about 6% of the

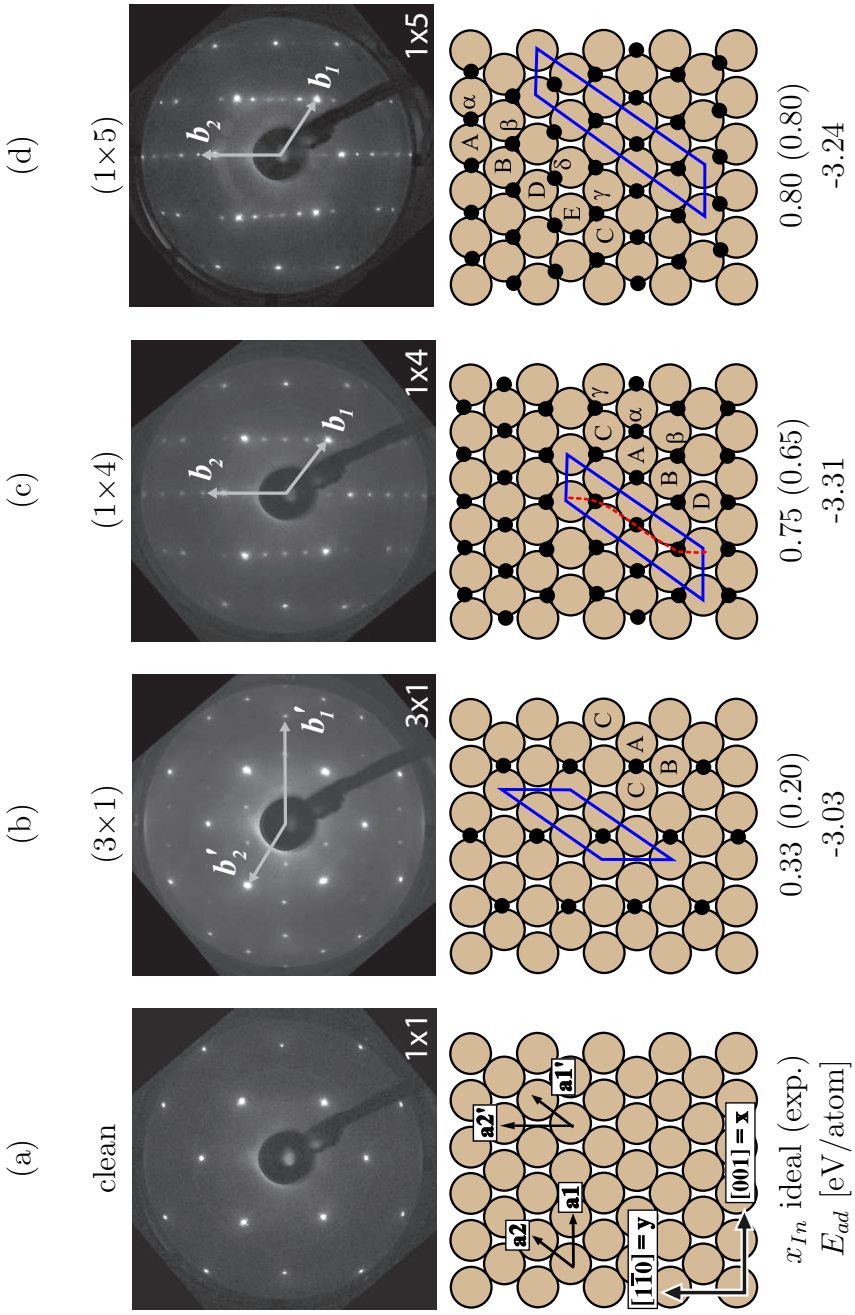

Figure 5.1: LEED patterns and top-view structural models for clean *W(110)*, (3×1), (1×4) and (1×5) *In* structures. Note, that the (3×1) supercell is specified relative to the basis-vectors a_1' and a_2' of *W(110)*, whereas the other structures are specified with respect to the basis vectors a_1 and a_2. Greek letters denote *In*, Latin letters denote *W*.

Table 5.2: LEED and PBE results for the (3×1)-*In*/*W(110)* structure. The atoms are labeled according to figure 5.1 (b). Displacements Δz in the direction normal to the surface are defined with respect to the center of the W surface layer. All values are given in Å.

	d_{In}	d_{12}	d_{23}	Δx_A	Δx_B	Δx_C	Δz_A	Δz_B	Δz_C
LEED	2.33	2.18	2.24	+0.03	0.00	-0.03	-0.02	+0.04	-0.02
PBE	2.35	2.20	2.25	+0.03	0.00	-0.03	-0.02	+0.05	-0.02

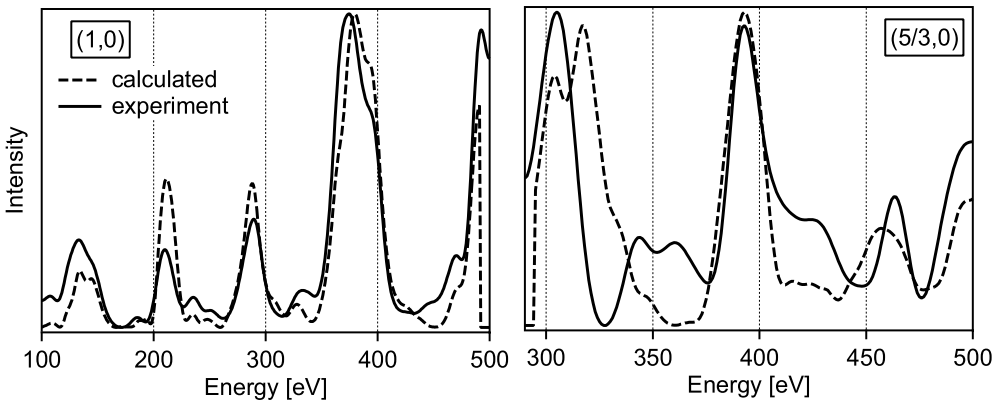

Figure 5.2: Comparison of experimental and simulated LEED intensities for the (1,0) and the (5/3,1) diffraction spots of the (3×1) overlayer.

nearest-neighbor *In*-*W* distance as compared with a hard-sphere model making use of the atomic sizes. Compared to clean *W(110)* the average interlayer distance d_{12} is slightly altered by *In* adsorption (LEED -3.1%, PBE -2.4%). Changes in deeper layers are within the error limits of the LEED analysis ($\approx 0.02 - 0.03$ Å).

1x4

At coverages of $x_{In} \approx 0.65$ a (1×4) diffraction pattern is observed by LEED [12], from which a unit cell with six *In* atoms and eight *W* atoms was derived. Figure 5.3 (a) shows the structural model proposed by Bürgener et al. [12, 13]. Within the unit cell all adatoms are located in H4 positions. The empty spaces within the unit cell are explained by assuming that they are needed for releasing stress acting on the *In* atoms. A simple consideration of the adsorption geometry shows that the stress within this model must be considerably since the *In*-*In* distances along the $[1\bar{1}1]$ direction as compared with the nearest neighbor bulk distance are strongly compressed by 18%. Using thus this model as initial positions for a DFT calculation the atoms relax quite substantially. Figure 5.3 (b) shows that the final positions show a totally different adsorption pattern. Another adsorption pattern considering the Nishiyama-Wassermann orientation for epitaxial growth was suggested by Gabl et al. [38] and is built by a unit cell containing 3 *In* atoms and 4 *W* atoms (corresponding to an ideal coverage of $x_{In} = 0.75$). In the adlayer *In* atoms are tightly packed with an atom density being even 2% larger than that of an *In(111)* bulk-like layer. The structural model as obtained from the PBE calculations is shown in figure 5.1 (c). It places one of the *In* atoms (labeled α) in the energetically most favorable H4 and the other two *In* atoms (labeled β and γ) into positions close to the H3 sites. In the calculation it turns out that the β and γ atoms are arranged symmetrically to the H4 site. As mentioned in section 5.3 at low coverages the H4 site is the most favourable site and the H3 site has an adsorption energy less by only ≈ 0.1 eV. For a full covered surface the H3 site is found to be the energetically most favourable site. Considering in addition the stress present in the structure shown in figure 5.3 (a) the (1×4) adsorption structure with *In* atoms in the H4 and close to the H3 sites provides a reasonable compromise between chemical adsorption and large stress within the *In* adlayer. Compared to the (3×1) structure the bonding is strengthened because the averaged adsorption energy per *In* atom in the (1×4) overlayer amounts to -3.31 eV/atom.

Guided by the theoretical results the LEED analysis was performed by M. Gabl and co-workers in the following way: In a first coarse grid search the position of *In* atom α is kept fixed in a H4 site, while the positions of the remaining two

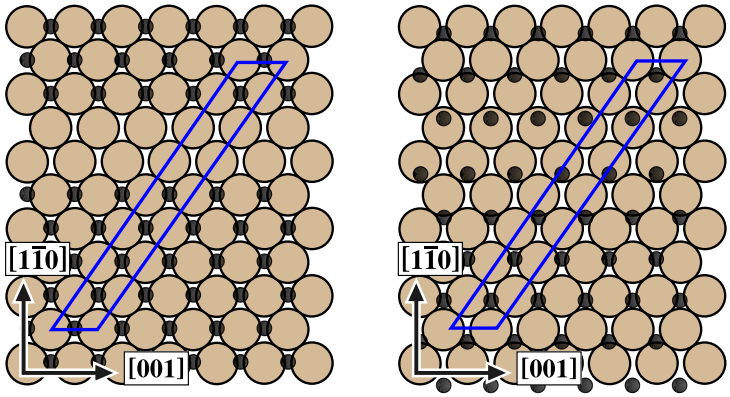

Figure 5.3: (a): Structural model for the (1×4) adsorption structure as proposed by Bürgener et al. [12, 13]. (b) shows the relaxed structure with initial positions chosen after (a). *W* atoms are shown in large brown circles, *In* atoms in small black circles.

Table 5.3: Interlayer distances and positions of *In* and *W* surface atoms as obtained by LEED and DFT (PBE) for (1×4)-*In*/*W(110)*. Atoms are labeled according to figure 5.1 (c). Displacements Δx and Δy (along [001] and along [1$\bar{1}$0], respectively) of the *In* atoms are given relative to the closest 4-fold adsorption site. Displacements Δz in the direction normal to the surface are defined with respect to the center of the *W* surface layer. All values are given in Å.

	d_{In}	d_{12}	d_{23}	Δz_A	Δz_B	Δz_C	Δz_D		
LEED	2.46	2.22	2.24	-0.02	-0.02	0.02	0.02		
PBE	2.52	2.22	2.25	-0.01	0.00	0.01	0.01		
	Δx_α	Δx_β	Δx_γ	Δy_α	Δy_β	Δy_γ	Δz_α	Δz_β	Δz_γ
LEED	0.00	0.00	0.00	0.00	-0.62	0.62	-0.04	0.02	0.02
PBE	0.00	0.01	0.02	0.00	-0.65	0.65	-0.03	0.02	0.02

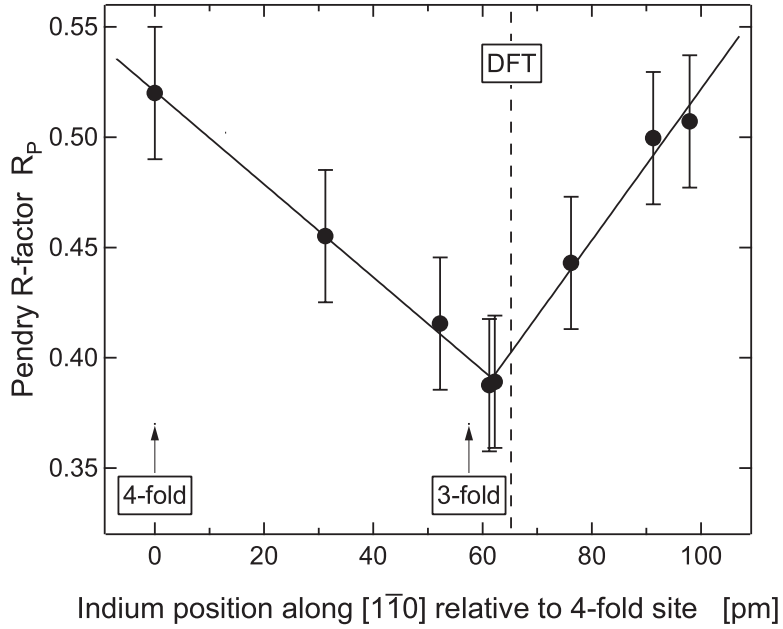

Figure 5.4: LEED-analysis of the (1×4)-structure. *In* atom α is fixed at the 4-fold site, while atoms β and γ are displaced symmetrically along a line moving away from the next 4-fold adsorption site along [1$\bar{1}$0]. The diagram shows the Pendry *R*-factor as a function of *In* positions along this line. The vertical dashed lines indicates the position favored by PBE.

In atoms β and γ are arranged symmetrically to the α atom along a line moving away from the next 4-fold site along $[1\bar{1}0]$. Then, in a second step close to the minimum of the grid search, positions are fine-tuned using the tensor-LEED approach. Figure 5.4 shows the variation of the R-factor as the position of the *In* atoms β and γ is changed in the first step of the evaluation. As can be seen, adsorption of all *In* atoms (α, β and γ) in pseudomorphic 4-fold sites - which is essentially the model suggested by Bürgener et al. [12] (figure 5.3 (a)) - clearly has to be excluded also from the LEED calculations. The optimum adsorption site, however, almost perfectly matches the ideal 3-fold position. It should be mentioned that in the LEED analysis the presence of clean *W* patches is also considered, since the (1×4)-structure exists over a rather large coverage range [38].

Final parameter optimization reveals the following details (see also table 5.3): the optimum positions of *In* atoms β and γ are on the high-symmetry line along $[1\bar{1}0]$ running through a 4-fold site, 0.62 Å (PBE: 0.65 Å) away from the 4-fold site, which is just slightly beyond the 3-fold coordinated position. They are located 2.48 Å (PBE: 2.54 Å) above the center of the *W* surface layer. In contrast, *In* atom α in the 4-fold site lies deeper, namely 2.42 Å (PBE: 2.49 Å) above the *W* top layer, resulting in buckling of 0.06 Å (PBE: 0.05 Å). Compared to the (3×1) structure the *In* atom in the H4 site is located 0.11 Å (PBE: 0.14 Å) higher above the top *W* layer, indicating that some *In*-*W* interlayer bonding strength is exchanged against intralayer *In*-*In* bonding. Due to the denser *In* overlayer in the (1×4) structure also the average *W* interlayer distance d_{12} is increased towards the bulk interlayer distance.

Drawing a line that indicates the alignment of the *In* adatoms (dotted line in figure 5.1 (c) it can be seen that within the unit cell this line is tilted away from the unit cell vector. As a consequence kinks in this interconnecting line appear from unit cell to unit cell with a period of 8.90 Å along $[1\bar{1}0]$. These kinks are also the reason for the striped structure observed by STM for (1×4) islands of *In*/*W(110)* [38]: the measured corrugation of these stripes is $\approx$ 0.08 Å, which compares well with the buckling period in the *In* overlayer (0.06 Å) as described above. The buckling of the *W* surface layer is quite small, close to the experimental and theoretical accuracy (LEED: 0.04 Å, PBE: 0.02 Å). Lateral displacements of *W* surface atoms as well as displacements of deeper-layer atoms out of their bulk positions are found to be insignificant (below 0.01 Å) for both, LEED and PBE.

Table 5.4: LEED and PBE results for the (1×5)-*In*/*W(110)* Structure. Atoms are labeled according to figure 5.1 (d). Displacements Δx and Δy (along [001] and along [1$\bar{1}$0], respectively) of the *In* atoms are given relative to the closest 4-fold adsorption site. Displacements Δz in the direction normal to the surface are defined with respect to the center of the *W* surface layer. All values are given in Å.

	d_{In}	d_{12}	d_{23}	Δz_A	Δz_B	Δz_C	Δz_D	Δz_E
LEED	2.47	2.21	2.24	-0.05	0.00	0.00	0.02	0.02
PBE	2.56	2.22	2.25	-0.02	0.00	0.00	0.01	0.01
	Δx_α	Δx_β	Δx_γ	Δx_δ	Δy_α	Δy_β	Δy_γ	Δy_δ
LEED	0.00	-0.11	0.11	0.79	0.00	-0.45	0.45	1.14
PBE	0.00	-0.08	0.08	0.80	0.00	-0.50	0.50	1.13
	Δz_α	Δz_β	Δz_γ	Δz_δ				
LEED	-0.08	-0.04	-0.04	0.15				
PBE	-0.06	-0.02	-0.02	0.11				

(1×5)

The unit cell of the (1×5) structure is similar to that of the (1×4) structure, but elongated by 25% along [1$\bar{1}$1]. For the analysis a unit cell with 4 In atoms and five *W* surface atoms is constructed, in perfect agreement with the experimentally determined coverage of $x_{In} = 0.80$ [12]. The calculated structure as shown in figure 5.1 (d) shows similarities to the (1×4) case but now the higher coverage of $x_{In} = 0.80$ of *In* atoms has to be accommodated. Similar to the (1×4) phase one *In* atom (α) sits in the 4-fold site and two *In* atoms (β, γ) close to the 3-fold coordinated site. For the fourth *In* atom in the unit cell (labeled δ), no such adsorption site is available and it has to adsorb at the short bridge site which is nearly as favourable as the H4 site at high coverages (cf. table 4.1).

Due to the occupation of this unfavorable adsorption site the average adsorption energy is slightly reduced to -3.24 eV/atom as compared to the (1×4) structure with -3.31 eV/atom. Furthermore, the buckling is increased from 0.06 to 0.23 Å (PBE 0.17 Å). Because of the buckling the compressive stress in the *In* adlayer is reduced: a coverage of $x_{In} = 0.80$ corresponds already to a *In* atom density which exceeds that of a densely-packed *In(111)* layer by 8%.

The rather complex (1×5) structure is verified experimentally by taking the theoretically calculated structure as a starting point for the analysis of the LEED-I/V data and searching for the optimum parameters in the vicinity of the the-

oretically predicted positions using the Tensor-LEED approach. This yields a minimum R-factor R_P=0.39, almost the same as obtained in the analysis of the (1×4) structure. Theoretically and experimentally determined geometric parameters are listed in table 5.4. In general, calculation and experiment agree well with each other. In particular, in both cases it is found that, when compared to the (1×4) structure, the *In* atoms β and γ in the pseudo 3-fold positions move ≈ 0.17 Å closer to the α atom as a consequence of forcing the *In* atom δ into the short-bridge site. Furthermore, the *In* atoms no longer reside on the high symmetry line running through a *W* surface atom along $[1\bar{1}0]$ (i.e. $|\Delta x| > 0$). Due to adsorption of *In* in the short-bridge site the buckling of the *W(110)* surface layer is approximately twice as much as for the (1×4) case (both in experiment and theory). However, the buckling is still quite small (LEED: 0.07 Å, PBE: 0.03 Å).

5.5 Comparison and Stability of Overstructures

The basic properties of the three *In* adlayer structures (interlayer distances d_{ij}, layer bucklings b_j and adsorption energies) as determined by LEED and PBE are summarized in table 5.5. In general, it can be stated that the agreement between experimental and theoretical data is very good. The *In* layer in the (3×1) structure is unbuckled, since all atoms reside in equivalent H4 adsorption sites. In the (1×4) phase the *In* atoms occupy two different adsorption sites resulting in a finite buckling of the *In* layer. However, the buckling is still small (0.06 Å) as also expected from a simple hard-sphere model. For the (1×5) overlayer the buckling is considerably increased due to occupation of the 2-fold short bridge site. Buckling of the *W* top layer is in the range 0.03-0.07 Å for all three structures.

For the (3×1) structure the distance between the centers of the *In* adlayer and the *W* surface layer exceeds the *W(110)* interlayer distance by $\approx 4\%$ due to the larger size of the *In* atoms as compared to *W*. For the (1×4) and (1×5) structures the layer distance is increased significantly to $\approx 11\%$ and $\approx 12\%$, respectively. Finally it is noted, that the surface relaxation of *W(110)* is reduced upon *In* deposition from $\approx 3\%$ to $\approx 1.5\%$ for the (1×4) and (1×5) superstructures.

Inspection of the calculated adsorption energies as listed in table 5.5 reveals, that the (1×4) structure is energetically the most stable one. The (1×5) structure is slightly less stable since it requires occupation of the less favored bridge site. The destabilization of the (3×1) structure is much stronger by 0.28 eV/atom although all *In* atoms occupy the most favorable 4-fold hollow site. Hence the destabilization of the (3×1) structure is a consequence of the large *In-In* separation and the associated loss of *In-In* bonding strength. Since the formulation of the adsorption energy, that has been used so far, is not dependent on the chemical

Table 5.5: Interlayer distances d_{ij} and layer bucklings b_j as well as adsorption energies for *In* adlayers on *W(110)*.

	(3×1)		(1×4)		(1×5)	
	LEED	PBE	LEED	PBE	LEED	PBE
	$\Delta d_{ij}/d_{bulk}$ [%]					
d_{In}	+4.9	+4.4	+9.9	+11.9	+10.0	+13.5
d_{12}	-3.1	-2.4	-0.9	-1.6	-1.1	-1.6
d_{23}	0.0	0.2	0.0	+0.0	0.0	+0.0
	b_j [Å]					
In	—	—	0.06	0.05	0.23	0.17
W_1	0.06	0.06	0.04	0.02	0.07	0.03
R_P	0.28		0.38		0.39	
E_{ad} [eV/atom]		-3.03		-3.31		-3.24
E'_{ad} [eV/atom]		-0.63		-0.91		-0.84

potential (or the surface coverage of a given overstructure), for a more general view of the stability a surface ground state diagram should be constructed after section 2.4.1. The ground state diagram for the *In/ W(110)* system is shown in figure 5.5. It is constructed by using the adsorption energies with respect to the *In* fct bulk phase E'_{ad} which can be calculated by adding the cohesive energy of 2.40 eV/atom for fct *In* to E_{ad}. Following the arguments in section 2.4.2 and equation 2.59 E'_{ad} is given as the intersection of the straight line representing the adsorbate structures with that of the clean surface. Since in figure 5.5 μ is given relative to the chemical potential of fct *In* the absolute values of the intersection points are identical with E'_{ad}. So the intersection points for the different surface energies are given at -0.91 / -0.84 / -0.63 eV for the (1×4) / (1×5) and (3×1) overstructures. The slope of the straight lines is given by the surface coverage: The higher the coverage the steeper the decline. The ground state line for the observed structures is then as follows: For $\mu < -0.91$ eV we find the clean surface to be the most stable structure. $-0.91 < \mu < 0.19$ eV the (1×4) structure is stable, changing to the (1×5) for $0.19 < \mu < 1.87$ eV. At chemical potentials greater than 1.87 eV only a full covered (1×1) surface structure can be found. From this point of view the (3×1) should not be stable, since at any chemical potential another stable structure can be found. Possible reasons why the observation in experiment is possible will be given in section 5.8.

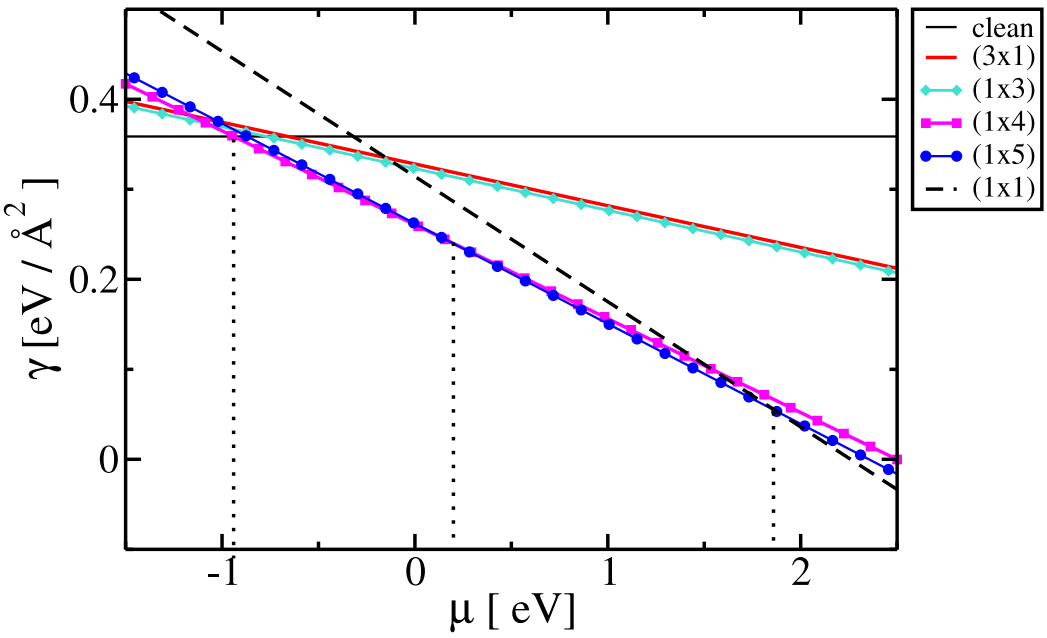

Figure 5.5: Ground state diagram for the *In/W(110)* system. From the experimentally observed overstructures only the (1×4) and (1×5) structures are ground states. The (3×1) is at any chemical potential μ unstable.

5.6 Freestanding Monolayers

In order to emphasize the importance of the *In-In* intralayer bonding also the binding energy of free-standing (3×1), (1×4), (1×5) and (1×1) *In* monolayers are calculated and compared to freestanding monolayers corresponding to the low-index surfaces of *In*. The binding energy is defined according to equation (3.16), taking again the total energy of a free *In* atom as reference energy. In figure 5.6 the calculated binding energies are plotted versus the atomic densities of the various monolayers. The data exhibit a parabolic relationship with a minimum at an areal atom density of 109% relative to that of an *In(111)* monolayer, which is close to the density of the (1×5) structure. The compression to a density beyond that of the densest *In* bulk layer obviously occurs in order to compensate for the missing bonds on both sides of the freestanding layer. Adsorption on *W(110)* partially relaxes this compression and the (1×4) – with an areal density still slightly larger than on *In(111)* – is favored over the (1×5) structure.

The scaling of binding energy with atomic density as the only important parameter is only possible, since all monolayers considered so far are relatively weakly anisotropic – even in the *In(110)* structure. For strongly anisotropic films the simple relationship does not hold. For example, the data point denoted

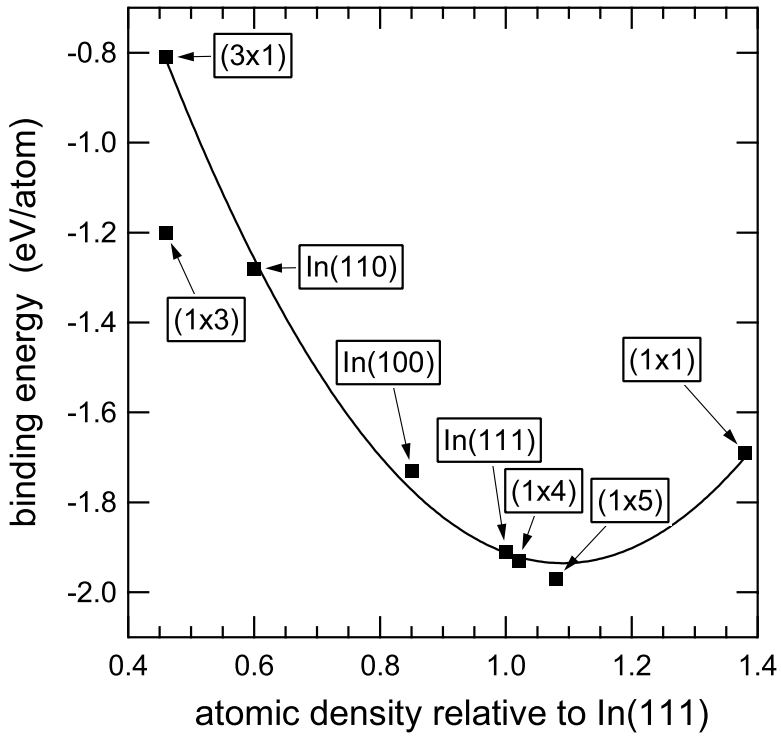

Figure 5.6: Binding energy vs. atom density for free-standing *In* monolayers in various geometries. Considering the adlayers of the observed overstructures and the low indexed surface planes of *In* only, a parabolic relation between the atomic density in the plane with respect to the binding energy can be found. If an anisotropic adlayer is studied, for example that one with label "(1×3)", this relation does not hold. For more details, see text.

"(1×3)" at a relative density of 0.46 lies well below the parabola spanned by all other data points. It is obtained for a structure, where *In* atoms are arranged in densely-packed rows along [001], which are separated from each other by two empty rows. This structure will be discussed in more detail in section 5.8.

5.7 Molecular Dynamics

Molecular dynamics (MD) simulations are a suitable method for finding the energetic minimum at a certain surface coverage. For confirmation of the different observed adsorption structures MD simulations at surface coverages of $x_{In} = 0.33$, 0.75 and 0.80 are done. For the simulation with $x_{In} = 0.33$ a (3×3) *W* substrate with three additional *In* atoms is used. As expected from the surface ground state diagram, for this coverage no stable structure could be identified. For the

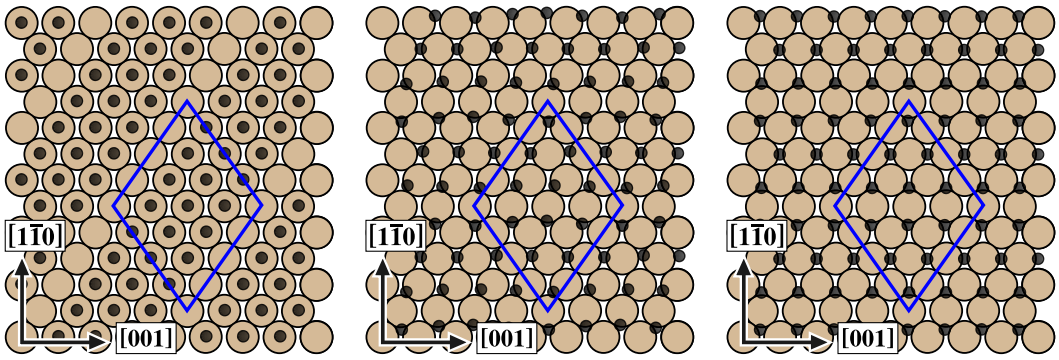

(a) (b) (c)

Figure 5.7: Molecular dynamics simulations at $x_{In} = 0.75$ of *In/ W(110)* with a (4×4) unit cell. (a) Starting configuration, (b) cooled system, (c) relaxed structure. *W* atoms (large brown circles), *In* atoms (small black circles).

coverage of $x_{In} = 0.80$ a *W* substrate with a (3×5) periodicity and 12 adatoms is chosen. Careful simulated annealing runs always ended up with one or several adatoms that are leaving the first mono layer. This is an indication that the (1×5) structure is only stable at low (or ambient) temperatures and will not be stable upon heating. It is also an indication that the most stable structure of the system can be found at a lower coverage of $x_{In} = 0.75$.

For the coverage of $x_{In} = 0.75$ a (4×4) unit cell with initial on-top positions for the *In* atoms is used, which certainly is an energetically very unfavorable configuration (figure 5.7 (a)). Equilibrating the system at T = 1000 K for 5 ps and cooling it down to 400 K for another 5 ps results in a configuration as illustrated in figure 5.7 (b). The distribution of *In* atoms is already very similar to the (1×4) structure (figure 5.1 (c)) as calculated before applying a static relaxation of atomic positions. Relaxing structure (b) further at T = 0 K finally leads to the configuration in figure 5.7 (c) which exactly is the (1×4) overstructure.

The preference of the (1×4) structure can also be understood from rather simple epitaxial considerations. The *W(110)* surface has a quasi-hexagonal symmetry. Therefore, the growth of *In* layers with a similar surface symmetry, i.e. with an *(111)* orientation is most likely, in particular since this is also the most densely packed *In* layer. Furthermore, in order to minimize the misfit between the *W(110)* and the *In(111)* planes at least along one direction, the orientation of *In*[1$\bar{1}$0] parallel to *W* [001] is advantageous, since the misfit along these directions is only 2% (see figure 5.8). This corresponds to the Nishiyama-Wassermann orientation for epitaxial growth. However, along *W* [1$\bar{1}$1] the misfit is considerable (≈23%). Nevertheless almost perfect coincidence can be achieved after four *W*

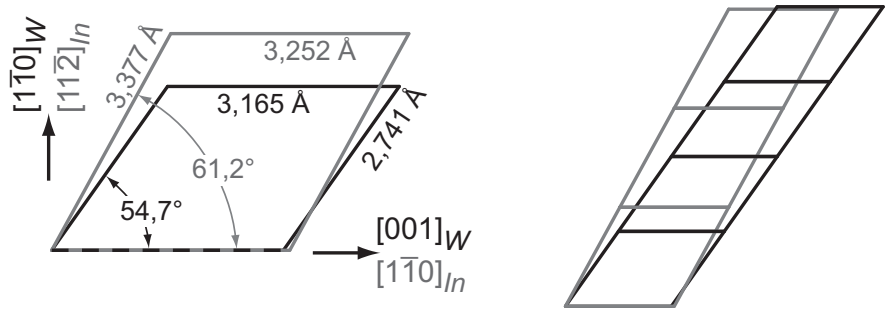

Figure 5.8: Relationship between the *W(110)* (black lines) and the *In(111)* unit cell (grey lines) in a Nishiyama-Wassermann orientation. The left panel shows both unit cells in direct comparison. The right panel demonstrates that supercells consisting of 4 *W* or 3 *In* unit cells, respectively, are close to coincidence.

unit cells –or three *In* unit cells, respectively– if the *In(111)* unit cell is slightly distorted by 6.5°, such that the cell angles of *W(110)* and the distorted *In(111)* layer are equal to each other. By such a construction, the (1×4) structure with three *In* atoms per unit is obtained.

5.8 Metastability of the (3×1) Structure

The higher stability of the high-coverage (1×4) phase as compared to the low-coverage (3×1) structure implies, that the (3×1) structure is only metastable, and that the energy of the *In/ W(110)* adsorption system can be minimized by forming islands with a local (1×4) structure. This conclusion is in line with previous LEED and STM experiments, showing that within several hours after deposition or upon annealing the (3×1) structure transforms into islands of (1×4) [38]. Obviously the (3×1) structure can only be observed due to kinetic restrictions.

However, in view of the calculated low diffusion barrier of 0.24 eV (c.f. section 5.3) this is somewhat surprising. Assuming a prefactor of $10^{13}s^{-1}$ this barrier is equivalent to an adatom hopping rate of 10^9 hops per second at room temperature, thus single *In* adatoms should be mobile enough to travel across the surface and to agglomerate into (1×4) islands.

Selected representative migration paths for other coverages are calculated as well by applying the the nudged elastic band method as implemented in VASP [67] within a two-dimensional supercell. Figure 5.9 shows the top view of two calculated migration paths. For the calculations a (3×3) unit cell as indicated in the sketches is used. These two examples might be possible steps to finally build up more stable structures like the (1×4) or other intermediate structures. In

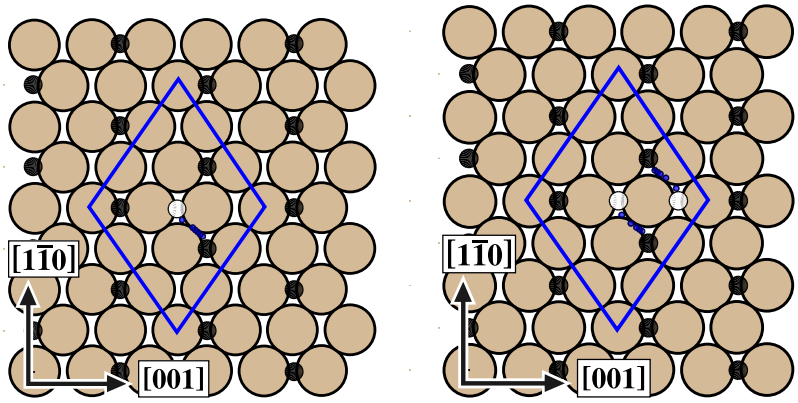

(a) (b)

Figure 5.9: Top view of the migration paths for selected start and end configurations, where a (3×3) unit cell for the DFT calculations was used. Starting from a (3×1) overstructure selected *In* atoms (drawn in black circles) are displaced to a neighboring H4 site. The intermediate positions are marked by small blue circles. The final positions are marked by a white circle. The energy barriers for the sketched transition paths is given in figure 5.10. In case of (a) one atom is moved towards to neighboring atoms. In (b) two atoms are displaced simultaneously in a symmetric way resulting in the (1×3) structure of figure 5.11. *W* atoms are shown in brown circles. For details see text.

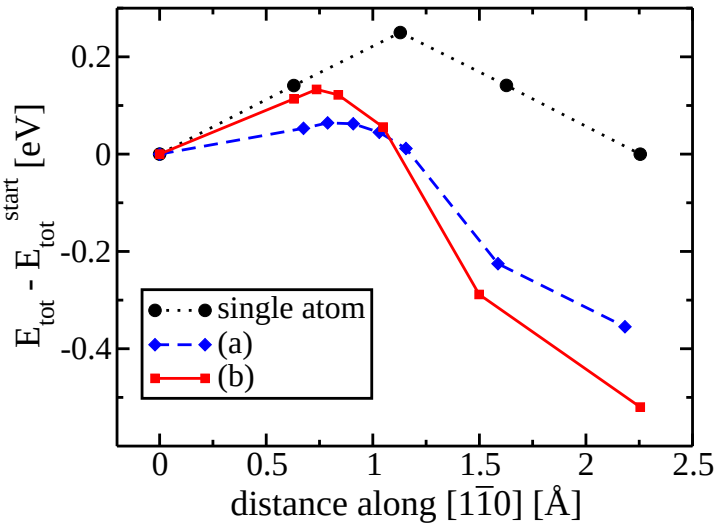

Figure 5.10: Energy barriers calculated by using the nudged elastic band method for the paths shown in figure 5.9 (a) and (b). For comparison also the energy barrier of a single atom displacement is given. The energy of an intermediate structure E_{tot} is always given with respect to the energy E_{tot}^{start} of the initial (3×1) overstructure. Energy barriers are strongly reduced from ≈ 0.24 eV for single atoms to ≈ 0.10 eV if other *In* atoms are present. In case of path (b) the barrier height has to be divided by a factor of 2, since in the path of figure 5.9 (b) two atoms are moved simultaneously. Since the energy difference for the final configurations is significantly negative the (3×1) is not found to be stable. For details see text.

figure 5.9 (a) the (3×1) overstructure is chosen as a starting point (*In* atoms of the start configuration are printed as black circles). Then one *In* atom is moved along the $[1\bar{1}\bar{1}]$ direction into the neighboring hollow site. The final position of the *In* atom is indicated by a white circle in figure 5.9 (a). The positions of the migration path found by the nudged elastic band method are indicated by small blue circles between the start and final position. It is noted, that for clarity only the migration path within the indicated unit cell is sketched. Due to the periodicity of the lattice the path should appear of course more often in the sketch. In figure 5.9 (b) a similar path to that of 5.9 (a) is shown with the difference, that now two atoms of an initial (3×1) structure are moved simultaneously so that a (1×3) structure (compare figure 5.11) is formed. The migration paths for both atoms are found to be symmetric, due to the symmetry of the mutual displacement. In figure 5.10 the corresponding energies of the intermediate positions for the migration paths are plotted. For a specific migration path the energy of a certain intermediate point E_{tot} is given relative to the energy of the starting configuration E_{tot}^{start}. For the position of the moved atom only the displacement along the $[1\bar{1}0]$ direction is given. The first curve in figure 5.10 gives the transition energy for the path of a single atom starting at a H4 site moving over a bridge site to a neighboring H4 site. In agreement to the energy barrier that is found for the energy difference between a H4 and bridge site for single site adsorption (see section 5.3), for the nudged elastic band calculations also a energy barrier of 0.24 eV is reproduced. The energy barrier corresponding to figure 5.9 (a) shows a significantly lower barrier of ≈ 0.06 eV. In case of the path chosen in 5.9 (b) the energy barrier is ≈ 0.12 eV. Accounting that in this case two atoms are displaced and only the total energy of the system is available through the DFT calculations, the effective barrier height in case of path (b) also is ≈ 0.06 eV. Different other starting setups, similar to the paths in figure 5.9, always resulted in energy barriers of not more than ≈ 0.1 eV. In comparison to the single atom case, barrier heights in general are strongly reduced, when *In* atoms move closer to other *In* atoms. From an energetic point of view these very small barrier heights indicate a very fast transition from (3×1) to other more stable structures. A possible explanation for this apparent puzzle is that small (1×4) islands are rather unstable and decay before further adatoms are attached. In terms of nucleation kinetics the latter scenario would be equivalent to a critical islands size substantially larger than one. Also the degeneracy of the different phases has to be taken into account. While the (3×1) structure can grow on three possible sublattices and the (1×4) on four, the transformation will be sluggish since the *In* sites in the (1×4) are all inequivalent whereas those for the (3×1) are not (see reference [27]).

Triggered by this instability of the (3×1) structure it is also searched for

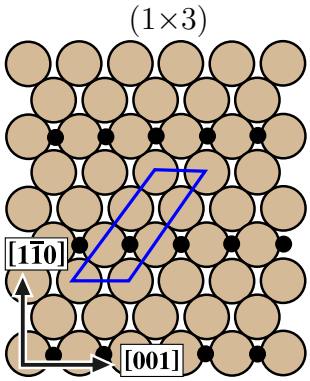

Figure 5.11: Theoretically postulated (1×3) *In* overstructure. This structure is similar to the (1×4) ground state structure since it has the same unit cell vector along the [001] and a 25 % reduced one into the [1$\bar{1}$1] direction. At an ideal coverage of $x_{In} = 0.33$ the adsorption energy $E_{ad} = -3.18$ eV/atom is found, being significantly lower than that of the experimentally observed (3×1) structure. *W* atoms are shown in large brown circles, *In* atoms in small black ones. For details see text.

alternative adsorption structures at $x_{In} = 0.33$. As it turned out, even if islanding is forbidden, the (3×1) structure is not the energetically most favorable structure at that coverage (see also the energy of the final states in figure 5.10 that are energetically more favorable structures than the (3×1), which was used as a starting point). Rather a (1×3) structure, consisting of single [001]-oriented rows of *In* atoms (located in 4-fold hollow sites) separated by two empty [001] rows is lower in energy (see figure 5.11). It has an adsorption energy of -3.18 eV/atom, which is in between the adsorption energies of the (3×1) and (1×4) structure. The reason for the higher stability of the atomic chains of the (1×3) structure as compared to the (3×1) structure is a strong gain in *In-In* interaction energy due to the closer packing of *In* atoms at least along one direction, which outweighs the loss of *In-In* interaction due to an increased distance in the perpendicular direction. However, since these atomic chains are already building blocks of the (1×4) structure, their formation may be hindered for the same reasons as the formation of (1×4) islands themselves. Furthermore, once the conditions (e.g. temperature) are such that the (1×3) structure can be formed, the system is probably also able to directly convert to the even more stable (1×4) phase, thus explaining why the (1×3) chain structure has never been observed in experiment. Considering the surface free energy γ of the (1×3) structure which is also plotted in figure 5.5, it becomes clear that the (1×3) is also not a ground state structure for the *In/ W(110)* system. Since it has the same coverage like the (3×1), the slope

of the straight line is identical. But the adsorption energy is still not favorable enough to make the (1×3) a ground state.

The arguments given before attribute the existence of the (3×1) structure to a kinetic stabilization relative to the (1×3) and (1×4) structures. Another possibility, which should be critically examined, is the influence of contaminants. Hence also the adsorption properties of hydrogen and oxygen on clean and *In*-covered *W(110)* are calculated. *H* is investigated as it is always present in the UHV rest gas, but difficult to detect, when adsorbed. *O* is investigated since it is used extensively in the preparation of clean *W(110)* and since a pronounced influence on the (3×1) → (1×4) transition in experiment is observed [38]. The adsorption of *O* and *H* on clean *W(110)* has been studied experimentally in a number of publications ([107, 94, 109] and [3, 1]). For both species the three fold coordinated adsorption site is found to be the energetically most favorable one. This favorite adsorption site is confirmed and the calculated adsorption energies of ≈-1.5 and ≈-4.2 eV/atom for single *H* and *O* atoms are found. One additional *H* atom within the (3×1) and (1×3) unit cells increases the difference in adsorption energies between these two structures, i.e. *H* contamination does not stabilize the (3×1) structure with respect to the (1×3).

Calculation of the adsorption energies for the (3×1) and (1×3) structures with one or two preadsorbed *O* atoms reveals that the relative stability of the (1×3) and (3×1) structures remains the same. *O* atoms stick to their favorite 3-fold hollow site, even in the presence of *In*. Since the *In*-*O* distance is small (≈ 1.5 Å) a repulsive interaction pushes the *In* atoms away from the 4-fold hollow site. Consequently, the adsorption energy of the *In* atoms is lowered with respect to the *O* free surface. For high coverages (in the calculations this corresponds to a concentration of 66 at% additional *O* atoms) the adsorption energy of *In* turns even lower than the cohesive energy of its bulk configuration, i.e. layer growth is hindered in this case and growth of 3-dimensional *In* islands has to be expected.

The total adsorption energy of *In* and *O* atoms for the (3×1)+*O* configurations is about 1 eV/atom less favorable than separated areas of pure *O* and pure *In* (1×4). This is substantially more than the 0.3 eV/atom difference between the (3×1) and (1×4) structure (see table 5.5). Hence *O* adsorption increases the driving force for the formation of the (1×4) structure, in accordance with experimental observation, that exposure to *O* triggers the transition from the (3×1) structure (with low local *In* coverage) into (1×4) islands with high local *In* coverage [38]. Thus the present PBE calculations are in perfect agreement with experimental findings not only with respect to the structural data, but also with respect to the energetics (metastability of (3×1)) and the driving forces for the (3×1) to (1×4) transition. However, there is a clear discrepancy of the present

data (both experimental and theoretical) to a previous study of Boiko [10], which reports that the (3×1) ⇔ (1×4) transition is reversible with respect to coverage and temperature. In the following two scenarios will be considered to explain this discrepancy.

The simplest explanation for the different experimental observations would be that in the experiments the sample has been cooled too fast (partially liquid nitrogen cooling has been used), thus freezing the high-temperature (1×4) phase and overlooking the reversibility of the transition. However, even in experiments without liquid nitrogen cooling the transition from (1×4) back to (3×1) is never observed. Furthermore, a transition from (1×4) to (3×1) upon lowering the temperature is in disagreement with the PBE results: The (1×4) is the energetically most favorable structure. Thus, according to the laws of thermodynamics, the (1×4) rather than the (3×1) structure should be formed upon temperature reduction - in contradiction to the results of Boiko.

The second scenario involves some unknown contamination which stabilizes the (3×1) structure. (However, as already discussed above, neither *H* nor *O* will do this). Upon heating the adsorbates desorb and the system transforms to the (1×4) phase. If subsequent cooling is done rapidly with low background pressure then the (1×4) structure still remains, while upon slow cooling with a bad background pressure the system might re-adsorb the contaminants and return to the (3×1) structure. A drawback of this scenario is its failure to explain why at room temperature the system transforms to the (1×4) structure with increasing time, although contamination increases rather than decreases with time.

None of these two scenarios gives a satisfactory and consistent explanation of all experimental and theoretical data. Thus, although this study is able to shed some light onto this problem, the (meta-) stability of the (3×1) *In/W(110)* phase is still an open problem.

A

Final Figure Set

In this part of the appendix the final effective cluster interaction energies are presented. The arrangement of the vertices in the *W(110)* surface is sketched in figures A.1 and A.2. In addition tables A.1 and A.2 present the corresponding sizes of the figures an the absolute value of the interaction energies. The labeling of the figures is arranged as follows: First the number of vertices is given, then a consecutive number within the corresponding figure class is added.

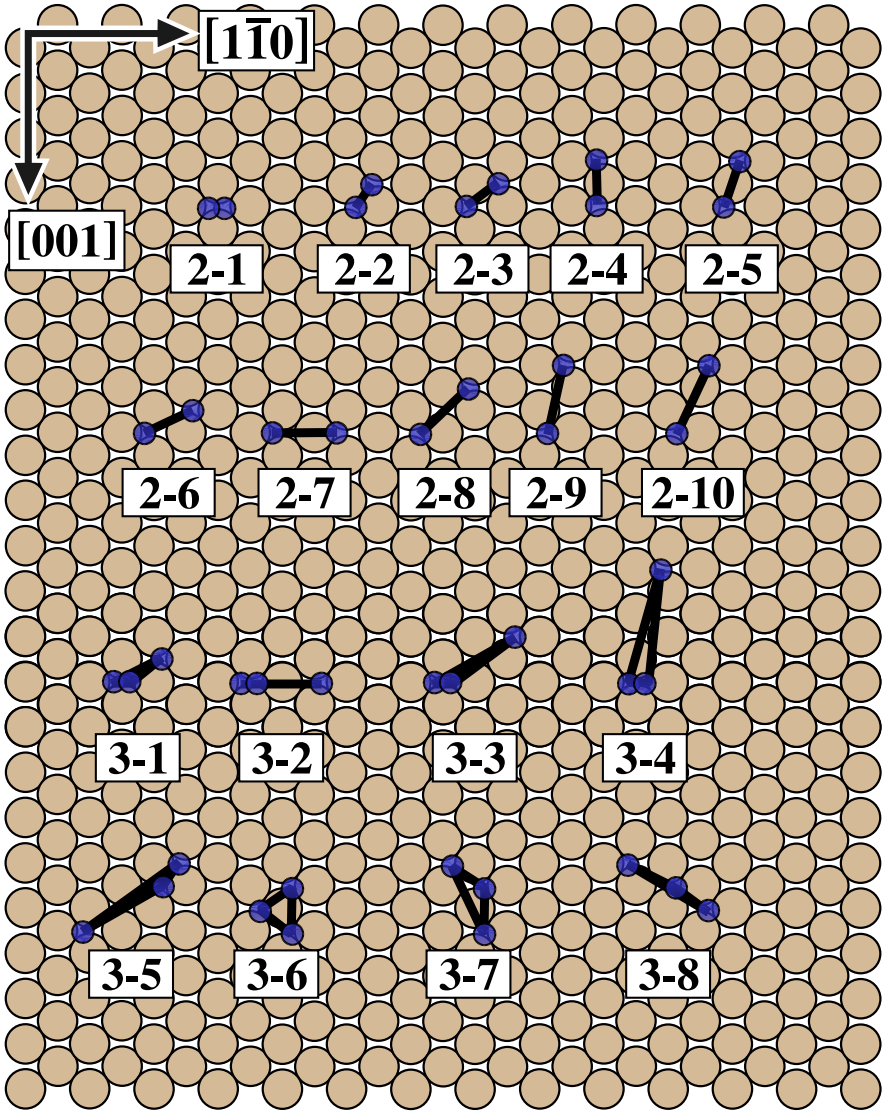

Figure A.1: First part of the final figure set of the CE of the *O / W(110)* system as determined by the genetic algorithm. It consists of 10 pairs, 19 Triples and 4 quadruples. The labels indicate the number of vertices and the number of the figure within the sub-class. For details see text.

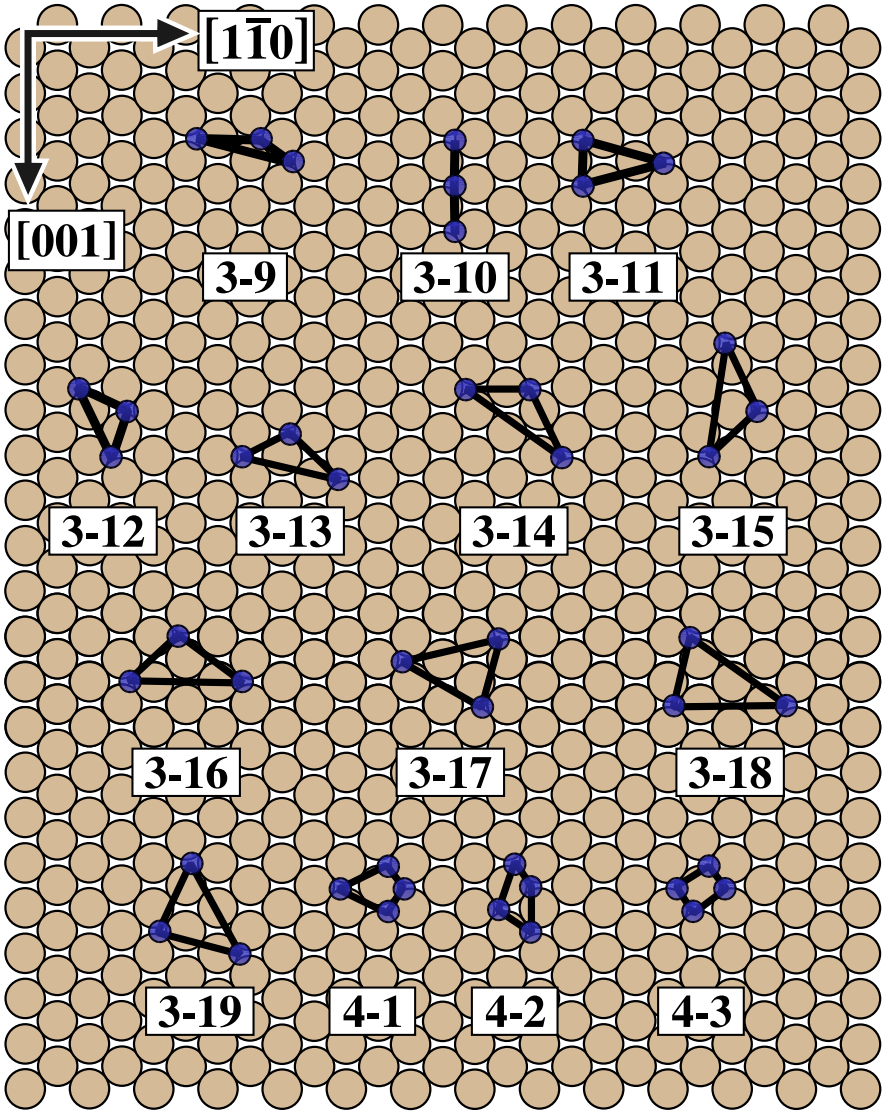

Figure A.2: Second part of the final figure set of the CE of the *O / W(110)* system as determined by the genetic algorithm. It consists of 10 pairs, 19 Triples and 4 quadruples. The labels indicate the number of vertices and the number of the figure within the sub-class. For details see text.

Table A.1: Final effective cluster interactions which were obtained according to the cluster expansion of section 4.4. The labels in the first column correspond to the geometric figures displayed in figure A.1. The second column shows the mean distances d which are found in the figure and the third column lists the effective cluster interactions ECI.

figure	d [Å]	ECI [meV]
constant	-	2106.05
onsite	-	4080.48
2- 1	1.13	1763.43
2- 2	1.95	2.02
2- 3	2.76	-43.93
2- 4	3.19	1.31
2- 5	3.38	21.21
2- 6	3.74	14.16
2- 7	4.51	-2.49
2- 8	4.65	2.15
2- 9	4.91	0.19
2-10	5.29	-10.05
3- 1	5.09	-53.02
3- 2	7.52	-36.99
3- 3	8.75	7.73
3- 4	11.64	-8.04
3- 5	11.14	-1.01
3- 6	5.81	15.28
3- 7	7.49	-0.94
3- 8	8.65	-12.25

Table A.2: Final effective cluster interactions which were obtained in the cluster expansion of section 4.4. The labels in the first column correspond to the geometric figures displayed in figure A.2. The second column shows the mean distances d which are found in the figure and the third column lists the effective cluster interactions ECI.

figure	d [Å]	ECI [meV]
3- 9	9.48	-0.74
3-10	8.50	-7.99
3-11	9.94	-3.00
3-12	8.27	-6.46
3-13	10.22	-7.82
3-14	12.05	1.45
3-15	11.99	5.18
3-16	12.04	6.79
3-17	12.23	3.13
3-18	14.06	3.25
3-19	12.24	-2.24
4- 1	9.54	8.67
4- 2	9.48	5.25
4- 3	8.10	-3.02

B

List of Calculated Structures

In this part of the appendix a number of calculated oxygen adsorption structures are presented and their adsorption energies are given. In order to display the most important calculated structures those which are lying close to the ground state line were selected. For each structure the concentration x_O, the unit cell size in multiples of the primitive vectors a_1 and a_2 of figure 3.7, the surface formation energy E_{surf} and the distance to the ground state line $\Delta E_{gstl} = E_{surf} - E_{groundStateLine}$ is given. E_{surf} and ΔE_{gstl} are given in units of meV/(1×1).

x_O = 0.167
unit cell = (2×6)
E_{surf} = -48.74
ΔE_{gstl} = -3.20

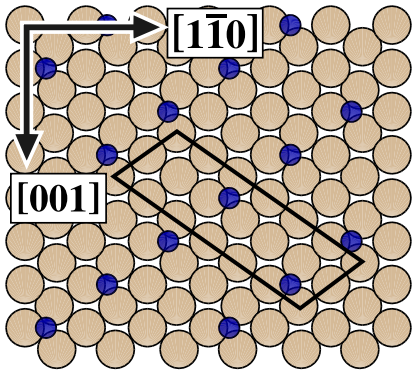

x_O = 0.167
unit cell = (2×6)
E_{surf} = -51.87
ΔE_{gstl} = 0.06

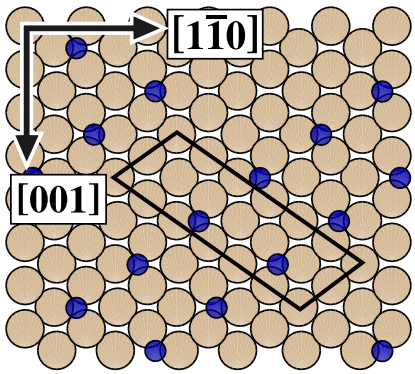

x_O = 0.200
unit cell = (2×5)
E_{surf} = -51.29
ΔE_{gstl} = 11.04

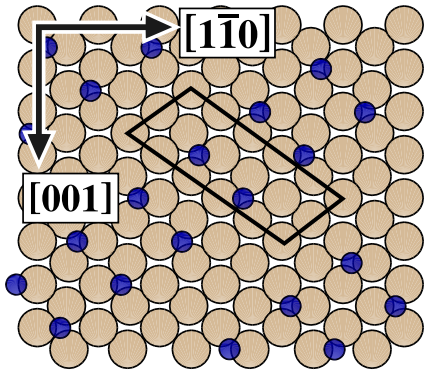

x_O = 0.250
unit cell = (2×4)
E_{surf} = -71.83
ΔE_{gstl} = 4.32

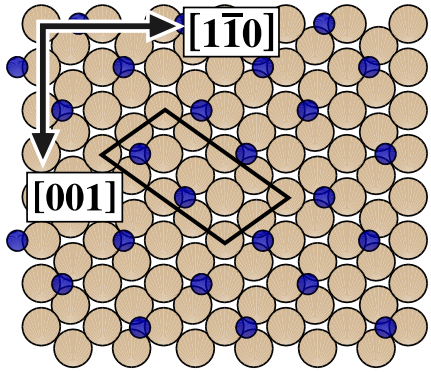

x_O = 0.333
unit cell = (2×6)
E_{surf} = -95.25
ΔE_{gstl} = 3.63

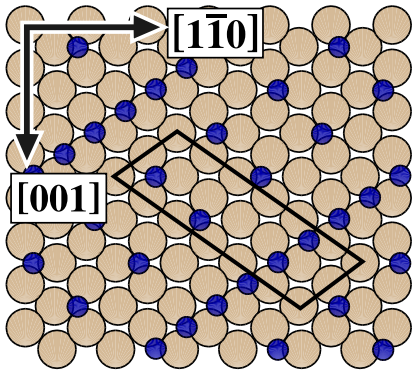

x_O = 0.333
unit cell = (2×3)
E_{surf} = -95.59
ΔE_{gstl} = 3.29

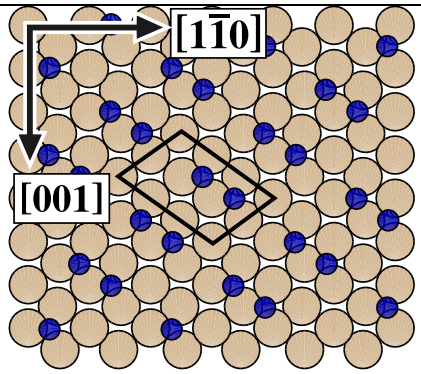

x_O = 0.333
unit cell = (2×6)
E_{surf} = -95.64
ΔE_{gstl} = 3.23

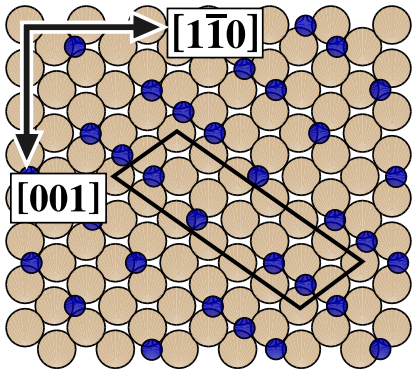

x_O = 0.333
unit cell = (2×6)
E_{surf} = -96.78
ΔE_{gstl} = 2.09

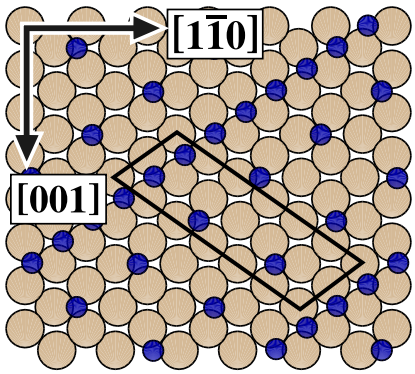

x_O = 0.400
unit cell = (1×5)
E_{surf} = -114.51
ΔE_{gstl} = 2.54

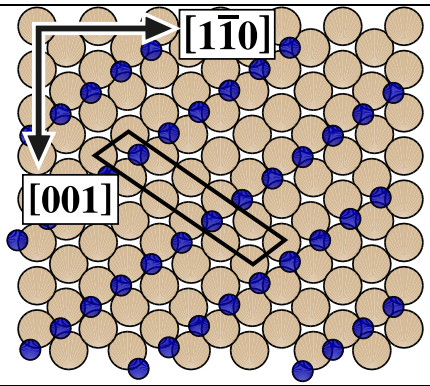

x_O = 0.429
unit cell = (1×7)
E_{surf} = -123.95
ΔE_{gstl} = 0.89

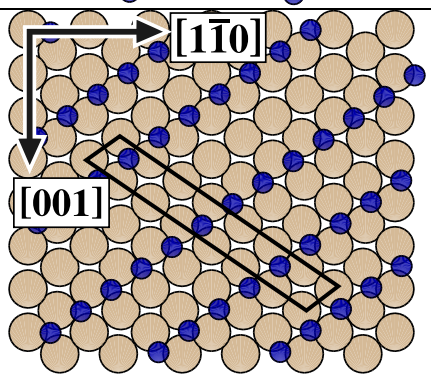

x_O = 0.454
unit cell = (1×11)
E_{surf} = -127.44
ΔE_{gstl} = 4.48

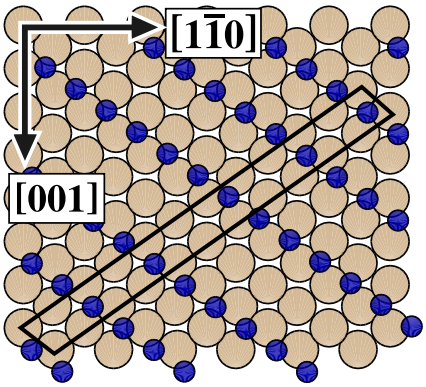

C

Real Space Monte Carlo Data

In addition to the real space Monte Carlo data shown in figure 4.16 in this part of the appendix a more extensive view of the Monte Carlo simulations is presented. As before, a (100×100) simulation cell with (2×100×100) lattices sites was used. Each of the figures C.1 to C.4 shows the Monte Carlo data at different O coverages for two temperatures, one snapshot above and one below the critical temperature T_c. O atoms on sublattice sites H3A are printed in black, O atoms on sites H3B in red and unoccupied sites are in white color.

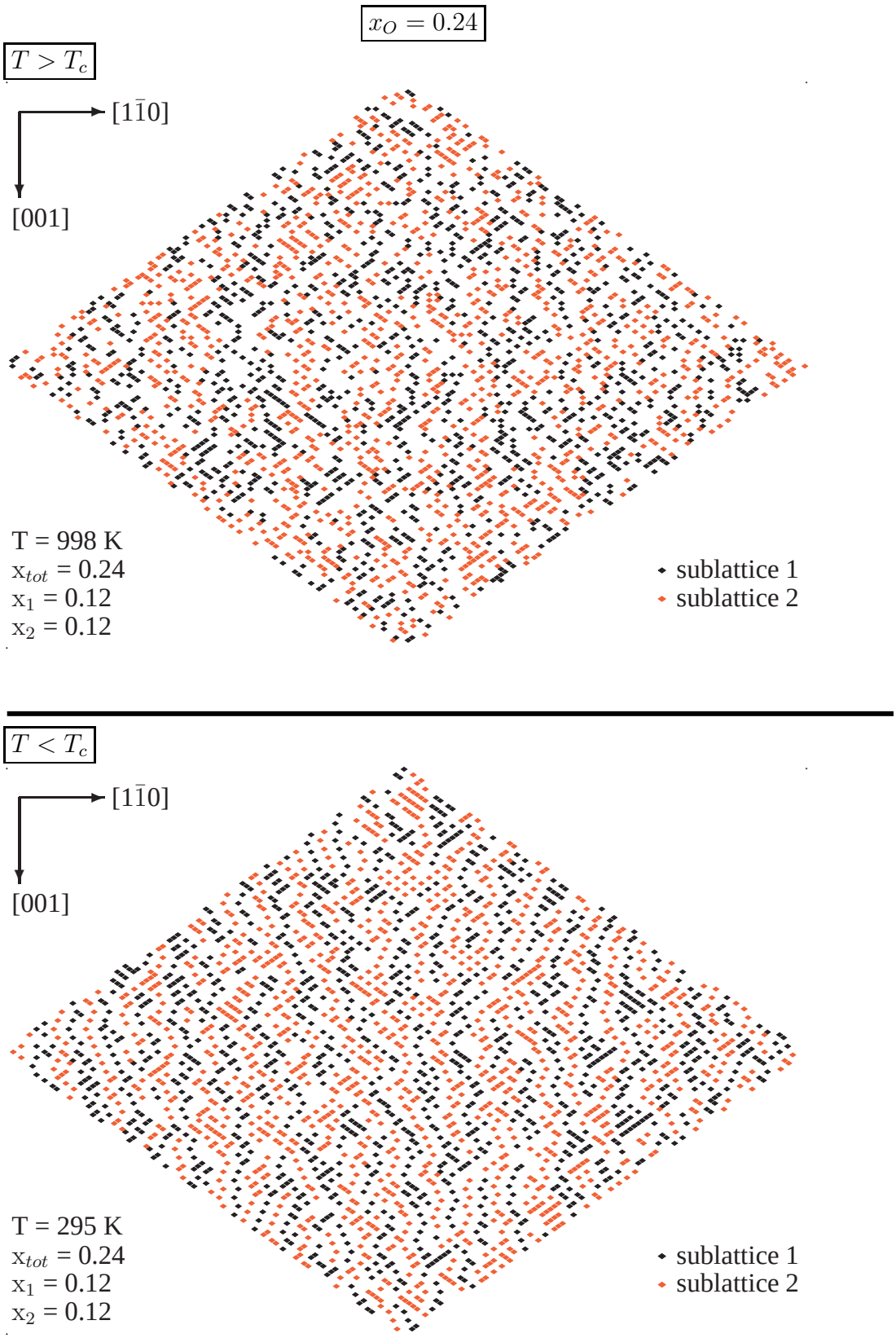

Figure C.1: Real space Monte Carlo data for the O adsorption on *W(110)* with an O coverage of $x_0 = 0.24$ for two different temperatures. The upper part of the figure shows an example for $T > T_c$ the lower part for $T < T_c$.

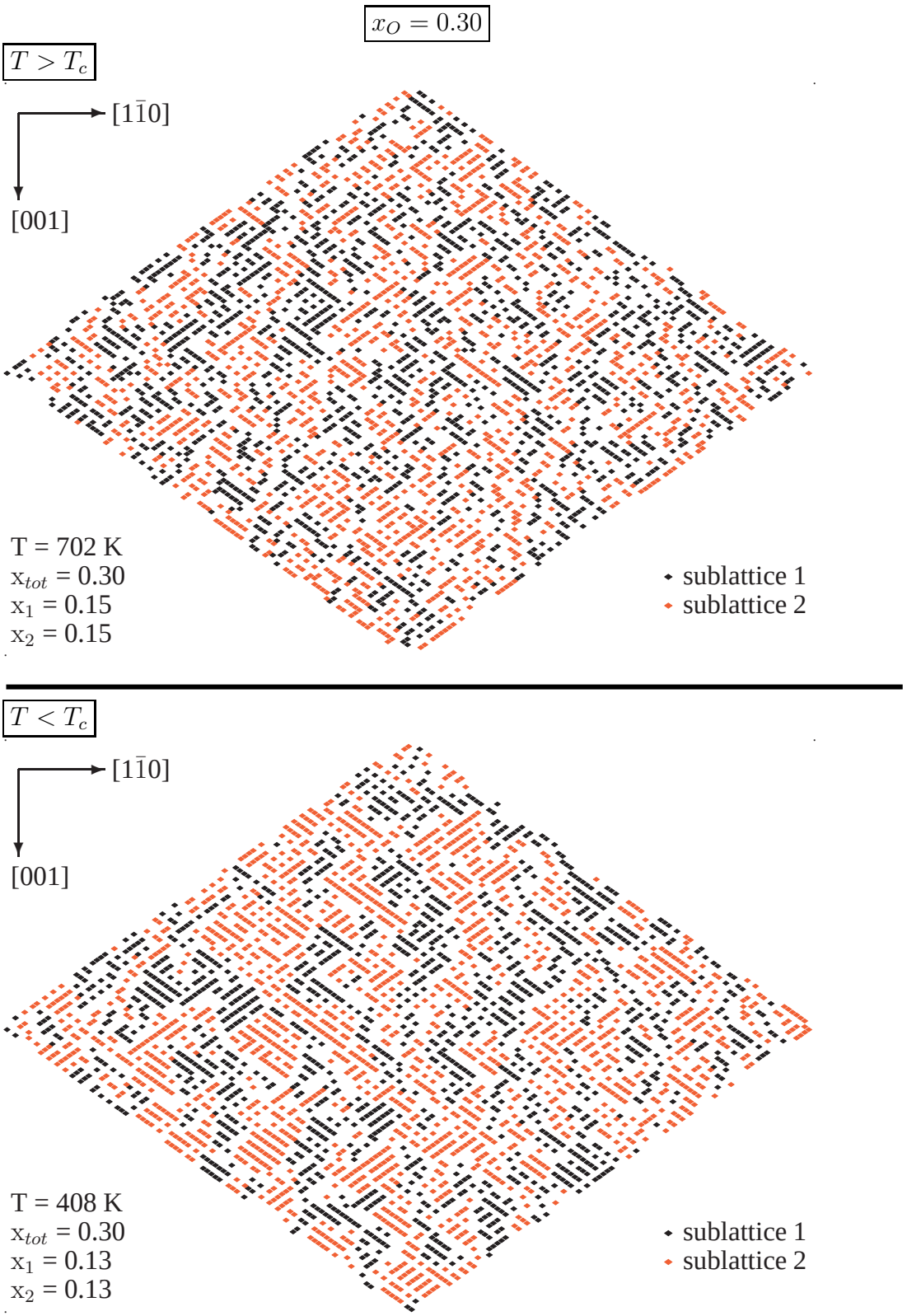

Figure C.2: Real space Monte Carlo data for the O adsorption on *W(110)* with an O coverage of $x_0 = 0.30$ for two different temperatures. The upper part of the figure shows an example for $T > T_c$ the lower part for $T < T_c$.

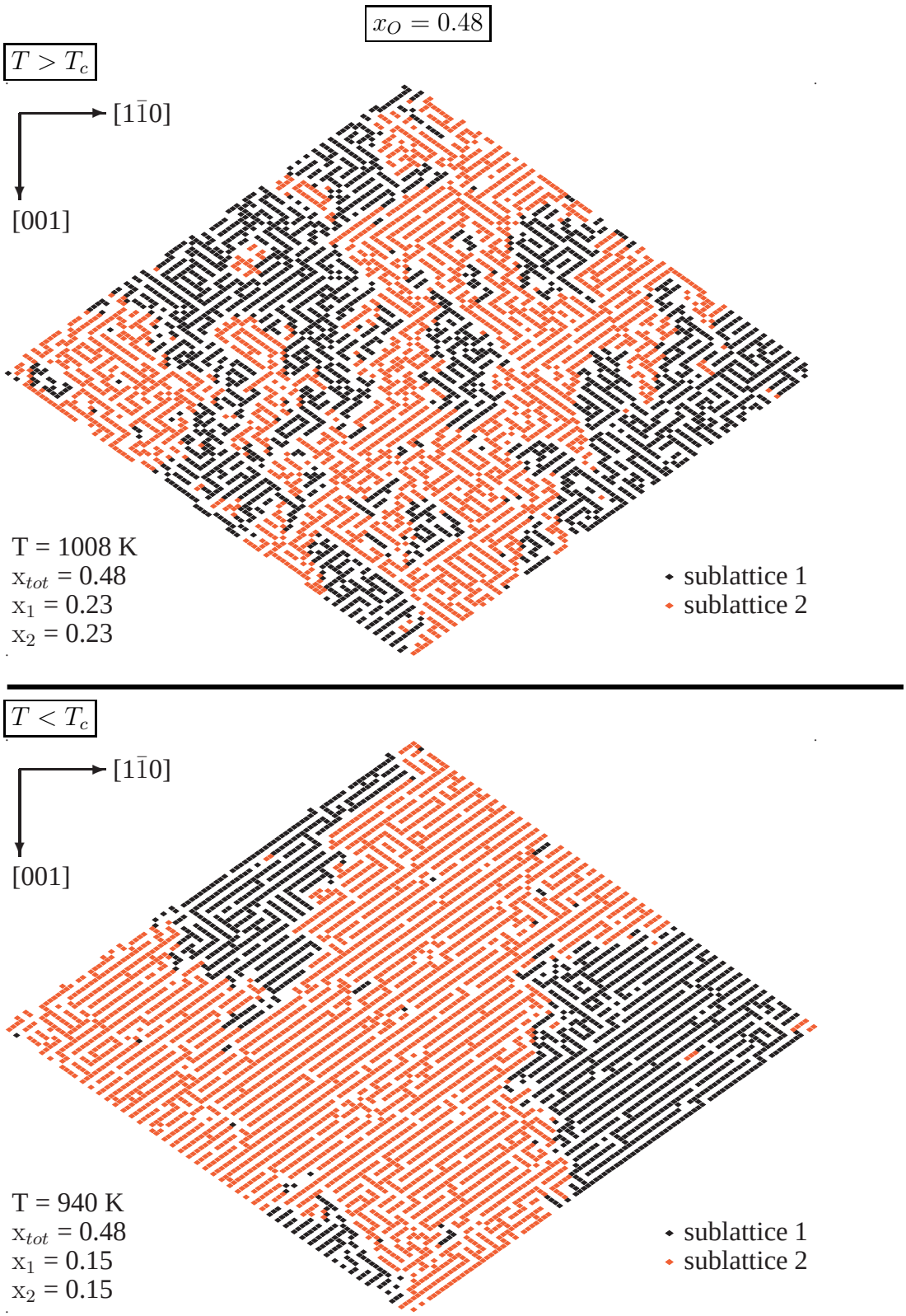

Figure C.3: Real space Monte Carlo data for the O adsorption on *W(110)* with an O coverage of $x_0 = 0.48$ for two different temperatures. The upper part of the figure shows an example for $T > T_c$ the lower part for $T < T_c$.

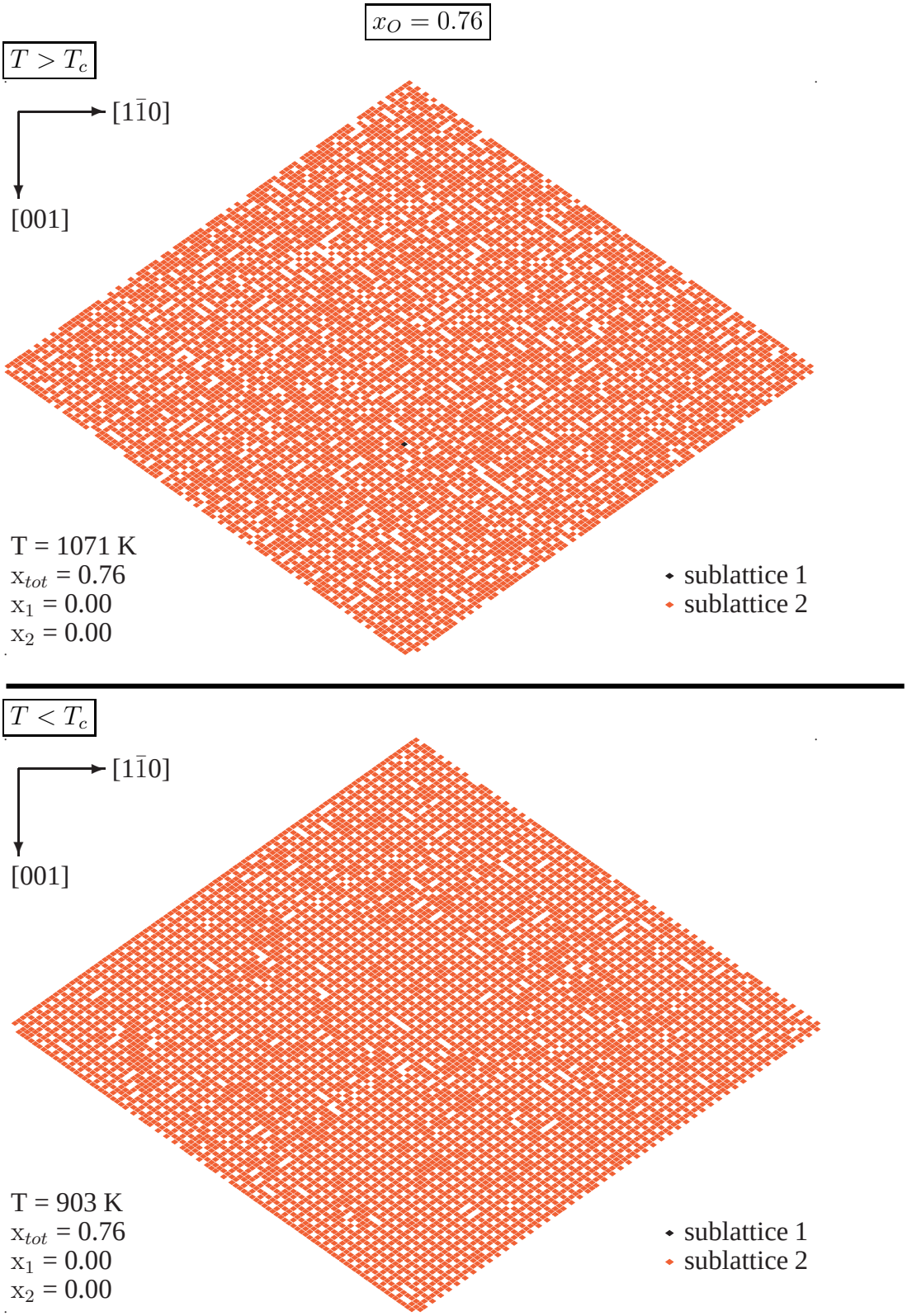

Figure C.4: Real space Monte Carlo data for the O adsorption on *W(110)* with an O coverage of $x_0 = 0.76$ for two different temperatures. The upper part of the figure shows an example for $T > T_c$ the lower part for $T < T_c$.

D

List of Publications

1. M. Stöhr,
   Das Segregationsverhalten der $Pt_{25}Rh_{75}$ (111) Oberfläche,
   Master thesis, Universität Erlangen 2005.

2. S. Müller, M. Stöhr, and O. Wieckhorst,
   Structure and stability of binary alloy surfaces: Segregation, relaxation, and ordering from first-principles calculations,
   Applied Physics A **82**, 415-419.

3. M. Stöhr, R. Podloucky, M. Gabl, N. Memmel, and E. Bertel,
   Combined ab-initio and LEED-I/V study of submonolayer adsorption of In on W(110),
   Phys. Rev. B **76** (2007), 195449.

4. M. Stöhr, R. Podloucky, and S. Müller,
   Ab initio phase diagram of oxygen adsorption on W(110),
   J. Phys.: Condens. Matter **21** (2009), 134017.

5. D. Reith, M. Stöhr, R, Podloucky, and S. Müller,
   Vibrational Properties and the Cluster Expansion: the Fe-Cu alloy system,
   in preparation.

6. M. Stöhr, C. Blaas-Schenner, M. Jahnatek, R. Podloucky, and J. Hafner,
   Structural competition of metastable phase studied by the Cluster expansion: the Ti-Nb alloy system,
   in preparation.

E

Talks and Conference Contributions

1. *First Principles based prediction of short range order at the* $\mathbf{Pt}_{25}\mathbf{Rh}_{75}$ *(111)-surface*,
   DPG Frühjahrstagung,
   Dresden, Germany,
   March, 26.-31.,2006.

2. *Ultrathin layers of In on W(110)*,
   JRP meeting "Nano structures on surfaces",
   Burg Schlaining, Austria, May, 30th, 2006.

3. *Ultrathin layers of In on W(110)*,
   Discussion of results within JRP "Nano structures on surfaces",
   Institute for Physical Chemistry, University of Innsbruck,
   Austria, September, 20th, 2006.

4. *Combined ab-initio and LEED-I/V study of submonolayer structures of In on W(110)*,
   CMS Seminar,
   University of Vienna, Vienna, Austria,
   March, 19th, 2007

5. *Ultrathin layers of In on W(110)*,
   Seminar: Defekte, Kinetik aktueller Legierungssysteme,
   University of Vienna, Vienna, Austria,
   June, 19th, 2007.

6. *Nanostructure formation on tungsten surfaces*,
   Evaluation of the science college WK04 by the austrian science fund FWF

November, 16th, 2007, Vienna, Austria.

7. *Cluster expansion studies of bulk alloys and alloy surfaces*,
   Workshop Intermetallics at the Erwin Schrödinger Institute,
   January, 10th, 2008.
   Vienna, Austria.

8. *Ab initio phase diagram of oxygen adsorption on W(110)*,
   March Meeting of the American Physical Society (APS),
   March, 13th, 2008,
   New Orleans, USA.

9. *Oxygen Adsorption on W(110): a Multiscale Modelling of the Phase Diagram*,
   COST Workshop on Multiscale Modelling,
   June, 25th, 2008,
   Brno, Czech Republic.

10. *Ab initio phase diagram of oxygen adsorption on W(110)*,
    Workshop: Nanostructures on Surfaces,
    November, 4th, 2008,
    Stadtschlaining, Austria.

11. *Ab initio phase diagram of oxygen adsorption on W(110)*,
    Evaluation of the "CMS Verein" at the Technical University of Vienna,
    November, 28th, 2008,
    Vienna, Austria.

12. *Ab initio phase diagram of oxygen adsorption on W(110)*,
    Seminar: Defekte, Kinetik und elektronische Struktur kondensierter Systeme,
    University of Vienna, Austria.

F

Curriculum Vitae

Personal Data

Name:	Stöhr Markus
Place of Birth:	Nördlingen, Germany
Date of Birth:	November, 2nd, 1979
Citizenship:	German

Education and Career

1986 - 1990	Leonhard-Fuchs-Elementary school Wemding (Germany)
1990 - 1999	Gymnasium Donauwörth (Grammer school)
1999 - 2000	Military service (medical service), Horb a. N. und Donauwörth (both Germany).
2000 - 2005	Study of physics (diploma) at the Friedrich-Alexander-University Erlangen-Nuremberg (Germany).
08/2002 - 01/2003	matriculation at the university Göteborg/Chalmers within the masters programme for astrophysics, Gothenborg (Sweden).
2003 - 2005	Work at different chairs of the faculty of physics. (Erlangen,Germany)
2003 - 2005	Supervision of the laboratory work of undergraduate physics students and other natural scientists (Erlangen, Germany)
09/2004 - 09/2005	Diploma thesis at the institute of condensed matter, chair of solid state physics under supervision of PD Stefan Müller (Erlangen, Germany).
02/2006 - 04/2009	PhD studies in the field of computational materials science / materials physics at the University of Vienna (Austria), Supervisor Prof. Dr. Raimund Podloucky.

G

Acknowledgments

At this point I would like to say "Thank you" to all people who supported me finishing this thesis.

- First of all many thanks to Prof. Raimund Podloucky who was a great supervisor. He always helped me when needed, but would also let me work freely and investigate things on my own. And I will always remember the nice evenings in different "Heurigen" or in Pameth.
- David Reith, who was a great co-worker, since we shared together not only the periods of frustration, but also those of success when things worked as they should.
- The rest of the group, Cesare Franchini, Petr Lazar, Robert Stadler, Jan Zabloudil, Claudia Blaas-Schenner and Ming-Xing Chen, who gave me a very pleasant working environment, and all other colleagues from the CMS, especially Doris Vogtenhuber and Martijn Marsman.
- Prof. Georg Kresse and Prof. Jürgen Hafner for providing the DFT-VASP package. Prof. Hafner did also a great job in managing the doctoral collage ("Wissenschaftskolleg").
- Prof. Josef Redinger for the motivation he gave me from time to time when visiting our group.
- Prof. Stefan Müller, for allowing the usage of his cluster expansion code UNCLE. Furthermore I would like to say thank you for the nice evenings we had in Vienna and elsewhere, and of course for the delivery of Franconian specialities to Vienna.
- Martin Gabl, Norbert Memmel, Erminald Bertel from Innsbruck for the good collaboration when writing the first paper.

- Financial support by the Austrian Science Fund (FWF) within the Joint Research Program S90 and the Science College W4 is gratefully acknowledged.

- I would like to thank my parents for the financial support especially during my time in Erlangen.

- Barbara Steininger who always motivated me in the last months before finishing this thesis.

- My basketball team WAT 3/3 Vienna Tigers, that gave me a great time on and off court.

Bibliography

[1] M. Altman, J. W. Chung, P. J. Estrup, J. M. Kosterlitz, J. Prybyla, D. Sahu, and S. C. Ying. Phase transformations of the H/W(110) and H/Mo(110) surfaces. *J. Vac. Sci. Technol., A*, 5:1045–1048, 1987.

[2] H. C. Andersen. Molecular dynamics simulations at constant pressure and/or temperature. *The Journal of Chemical Physics*, 72(4):2384–2393, 1980.

[3] M. Arnold, G. Hupfauer, P. Bayer, L. Hammer, K. Heinz, B. Kohler, and M. Scheffler. Hydrogen on W(110): an adsorption structure revisited. *Surf. Sci.*, 382:288, 1997.

[4] D. H. Baek, J. W. Chung, and W. K. Han. Critical behavior of the p(2x1)-O/W(110) system. *Phys. Rev. B*, 47(14):8461–8464, Apr 1993.

[5] K. Binder. Applications of Monte Carlo methods to statistical physics. *Reports on Progress in Physics*, 60(5):487–559, 1997.

[6] P. Blöchl. Porjector augmented-wave method. *Phys. Rev. B*, 50:17953–17979, 1994.

[7] V. Blum, G. L. W. Hart, M. J. Walorski, and A. Zunger. Using genetic algorithms to map first-principles results to model Hamiltonians: Application to the generalized Ising model for alloys. *Phys. Rev. B*, 72(16):165113, 2005.

[8] V. Blum and K. Heinz. Fast LEED intensity calculations for surface crystallography using Tensor LEED. *Comput. Phys. Commun.*, 134(3):392 – 425, 2001.

[9] V. Blum and A. Zunger. Mixed-basis cluster expansion for thermodynamics of bcc alloys. *Phys. Rev. B*, 70(15):155108, Oct 2004.

[10] B. Boiko. Phase Transitions in the W(110) - In Film System. *Phys. Chem. Mech. Surfaces*, 5(5):1054–1063, 1990.

[11] J. C. Buchholz and M. G. Lagally. Order-Disorder Transition and Adatom-Adatom Interactions in a Chemisorbed Overlayer: Oxygen on W(110). *Phys. Rev. Lett.*, 35(7):442–445, Aug 1975.

[12] M. Bürgener, A. Bukaluk, M. Cyrankiewicz, A. Goldmann, R. Siuda, and M. Trzcinski. Growth of ultrathin In layers on W(110) studied by high-resolution electron spectroscopies. *Surf. Sci.*, 529(3):490 – 502, 2003.

[13] M. Bürgener and A. Goldmann. Oxidation of ultrathin indium layers on W(1 1 0): a core-level photoemission study. *Surf. Sci.*, 540:89–96, 2003.

[14] B. S. Chandrasekhar and J. A. Rayne. Elastic Constants of Indium from 1.4 K to 300 K. *Phys. Rev.*, 124(4):1011–1014, Nov 1961.

[15] W. Y. Ching, D. L. Huber, M. G. Lagally, and G. C. Wang. Order-disorder transformations in chemisorbed layers: Oxygen on W(110). *Surf. Sci.*, 77(3):550–560, Nov. 1978.

[16] J. W. D. Connolly and A. R. Williams. Density-functional theory applied to phase transformations in transition-metal alloys. *Phys. Rev. B*, 27(8):5169–5172, Apr 1983.

[17] J. M. Cowley. X-Ray Measurement of Order in Single Crystals of Cu[sub 3]Au. *Journal of Applied Physics*, 21(1):24–30, 1950.

[18] C. J. Cramer, W. B. Tolman, K. H. Theopold, and A. L. Rheingold. Variable character of O?O and M?O bonding in side-on (?2) 1:1 metal complexes of O2. *Proceedings of the National Academy of Sciences of the United States of America*, 100(7):3635–3640, 2003.

[19] J. Czerniak. *Software 2.0 Extra!*, 1, 2004.

[20] H. Daimon, R. Ynzunza, J. Palomares, H. Takabi, and C. S. Fadley. Direct structure analysis of W(110)-(1x1)-O by full solid-angle X-ray photoelectron diffraction with chemical-state resolution. *Surf. Sci.*, 408(1-3):260–267, June 1998.

[21] D. de Fontaine. Configurational Thermodynamics of Solid Solutions. *Solid State Physics*, 34:73, 1979.

[22] S. Dennler and J. Hafner. First-principles study of ultrathin magnetic Mn films on W surfaces. *Phys. Rev. B*, 72(21):214413, 2005.

[23] R. Drautz. *Dissertation.* MPI für Metallforschung Stuttgart, 2003.

[24] R. Drautz and A. Díaz-Ortiz. Obtaining cluster expansion coefficients in ab initio thermodynamics of multicomponent lattice-gas systems. *Phys. Rev. B*, 73(22):224207, 2006.

[25] R. Drautz, H. Reichert, M. Fähnle, H. Dosch, and J. M. Sanchez. Spontaneous $L1_2$ Order at $Ni_{90}Al_{10}(110)$ Surfaces: An X-Ray and First-Principles-Calculation Study. *Phys. Rev. Lett.*, 87(23):236102, Nov 2001.

[26] R. Drautz, R. Singer, and M. Fähnle. Cluster expansion technique: An efficient tool to search for ground-state configurations of adatoms on plane surfaces. *Phys. Rev. B*, 67(3):035418, Jan 2003.

[27] ed. D. A. King and D. P. Woodruff. Phase Transitions and Adsorbate Restructuring of Metal Catalysts. 7, 1994.

[28] A. Elbe, G. Meister, and A. Goldmann. Vibrational modes of atomic oxygen on W(110). *Surf. Sci.*, 371(2-3):438–444, Feb. 1997.

[29] G. Ertl and D. Schillinger. Interactions between chemisorbed atoms: Oxygen on W(110). *J. Chem. Phys.*, 66(6):2569–2573, 1977.

[30] M. Fähnle, R. Drautz, F. Lechermann, R. Singer, A. Diaz-Ortiz, and H. Dosch. Thermodynamic properties from ab-initio calculations: New theoretical developments, and applications to various materials systems. *physica status solidi (b)*, 242(6):1159–1173, 2005.

[31] F. H. Featherston and J. R. Neighbours. Elastic Constants of Tantalum, Tungsten, and Molybdenum. *Phys. Rev.*, 130(4):1324–1333, May 1963.

[32] E. Fermi. *Z. Phys.*, 48:73–79, 1975.

[33] L. G. Ferreira, S.-H. Wei, and A. Zunger. First-principles calculation of alloy phase diagrams: The renormalized-interaction approach. *Phys. Rev. B*, 40(5):3197–3231, Aug 1989.

[34] L.-G. Ferreira, S.-H. Wei, and A. Zunger. Stability, electronic structure, and phase diagrams of novel intersemiconductor compounds. *International Journal of Supercomputer Applications*, 5:34–56, 1991.

[35] R. P. Feynman. Forces in Molecules. *Phys. Rev.*, 56(4):340–343, Aug 1939.

[36] C. Franchini, V. Bayer, R. Podloucky, G. Parteder, S. Surnev, and F. P. Netzer. Density functional study of the polar MnO(111) surface. *Phys. Rev. B*, 73(15):155402, 2006.

[37] D. Frenkel and B. Smit. *Understanding molecular simulation : from algorithms to applications*. Acad. Press, 1996.

[38] M. Gabl, M. Trzcinski, N. Memmel, A. Bukaluk, and E. Bertel. Metastable and stable overstructures of In on W(110). *Surf. Sci.*, 600(18):4390 – 4394, 2006. Berlin, Germany: 4-9 September 2005, Proceedings of the 23th European Conference on Surface Science.

[39] G. D. Garbulsky and G. Ceder. Linear-programming method for obtaining effective cluster interactions in alloys from total-energy calculations: Application to the fcc Pd-V system. *Phys. Rev. B*, 51(1):67–72, Jan 1995.

[40] D. Goldfarb and A. Idnani. A numerically stable dual method for solving strictly convex quadratic programs. *Mathematical Programming*, 27(1):1–33, Sept. 1983.

[41] D. Gorodetskii, A. Yas'ko, and Fung-Kho. *Izv. Akad. Nauk USSR, Ser. Fiz.*, (33):467, 1969.

[42] J. M. Haile and H. W. Graben. Molecular dynamics simulations extended to various ensembles. I. Equilibrium properties in the isoenthalpic–isobaric ensemble. *The Journal of Chemical Physics*, 73(5):2412–2419, 1980.

[43] H. Hellmann. *Einfuhrung in die Quantumchemie*. Deuticke, Leipzig, 1937.

[44] P. Hohenberg and W. Kohn. Inhomogeneous Electron Gas. *Phys. Rev.*, 136(3B):B864–B871, Nov 1964.

[45] E. Ising. Beitrag zur Theorie des Ferromagnetismus. *Zeitschrift für Physik A Hadrons and Nuclei*, 31(1):253–258, Feb. 1925.

[46] K. E. Johnson, R. J. Wilson, and S. Chiang. Effects of adsorption site and surface stress on ordered structures of oxygen adsorbed on W(110). *Phys. Rev. Lett.*, 71(7):1055–1058, Aug 1993.

[47] A. Katoh, H. Miwa, Y. Maehara, H. Kawanowa, and Y. Gotoh. Studies on surface structures and growth of In ultrathin films on Mo(110) surface. *Surface Science*, 566-568(Part 1):181 – 185, 2004. Proceedings of the 22nd European Conference on Surface Science.

[48] B. Kim, J. Chen, J. L. Erskine, W. N. Mei, and C. M. Wei. Surface and bulk photoelectron diffraction from W(110) 4f core levels. *Phys. Rev. B*, 48(7):4735–4740, Aug 1993.

[49] W. Kohn and L. Sham. *Phys. Rev.*, 140:A1133–A1138, 1965.

[50] M. Kottcke and K. Heinz. A new approach to automated structure optimization in LEED intensity analysis. *Surface Science*, 376(1-3):352 – 366, 1997.

[51] G. Kresse and J. Furthmüller. Efficient iterative schemes for ab initio total-energy calculations using a plane-wave basis set. *Phys. Rev. B*, 54(16):11169–11186, Oct 1996.

[52] G. Kresse and J. Hafner. Ab initio molecular dynamics for liquid metals. *Phys. Rev. B*, 47(1):558–561, Jan 1993.

[53] G. Kresse and D. Joubert. From ultrasoft pseudopotentials to the projector augmented-wave method. *Phys. Rev. B*, 59:1758–1775, 1999.

[54] M. Lagally, T.-M. Lu, and G.-C. Wang. *Ordering in Two Dimensions*. Elsevier, New York, 1980.

[55] M. G. Lagally, J. C. Buchholz, and G.-C. Wang. LEED intensity - averaging experiments for surface - layer structure determination. *Journal of Vacuum Science and Technology*, 12(1):213–221, 1975.

[56] D. B. Laks, L. G. Ferreira, S. Froyen, and A. Zunger. Efficient cluster expansion for substitutional systems. *Phys. Rev. B*, 46(19):12587–12605, Nov 1992.

[57] D. Lerch, O. Wieckhorst, L. Hammer, K. Heinz, and S. Müller. Adsorbate cluster expansion for an arbitrary number of inequivalent sites. *Phys. Rev. B*, 78(12):121405, 2008.

[58] D. Lerch, O. Wieckhorst, G. Hart, R. W. Forcade, and S. Müller. Constructing Cluster-Expansions for Arbitrary Lattices with Minimal User-Input. *Modelling Simul. Mater. Sci. Eng.*, submitted.

[59] A. Y. Lozovoi, A. Alavi, and M. W. Finnis. Surface energy and the early stages of oxidation of NiAl(110). *Comput. Phys. Commun.*, 137(1):174–194, June 2001.

[60] T. M. Lu, G. C. Wang, and M. G. Lagally. Island-Dissolution Phase Transition in a Chemisorbed Layer. *Phys. Rev. Lett.*, 39(7):411–414, Aug 1977.

[61] Z. W. Lu, S.-H. Wei, A. Zunger, S. Frota-Pessoa, and L. G. Ferreira. First-principles statistical mechanics of structural stability of intermetallic compounds. *Phys. Rev. B*, 44(2):512–544, Jul 1991.

[62] J. S. Luo and B. Legrand. Multilayer relaxation at surfaces of body-centered-cubic transition metals. *Phys. Rev. B*, 38(3):1728–1733, Jul 1988.

[63] D. H. M. Methfessel and M. Scheffler. Calculated Surface Energies of the 4d Transition Metals: A Study of Bond-Cutting Models. *Applied Physics A: Solids and Surfaces*, 55:442–448, 1992.

[64] M. Methfessel and A. T. Paxton. High-precision sampling for Brillouin-zone integration in metals. *Phys. Rev. B*, 40(6):3616–3621, Aug 1989.

[65] N. Metropolis, A. W. Rosenbluth, M. N. Rosenbluth, A. H. Teller, and E. Teller. Equation of State Calculations by Fast Computing Machines. *The Journal of Chemical Physics*, 21(6):1087–1092, 1953.

[66] W. Meyer. private communication.

[67] G. Mills, H. Jnsson, and G. K. Schenter. Reversible work transition state theory: application to dissociative adsorption of hydrogen. *Surface Science*, 324(2-3):305 – 337, 1995.

[68] H. J. Monkhorst and J. D. Pack. Special points for Brillouin-zone integrations. *Phys. Rev. B*, 13(12):5188–5192, Jun 1976.

[69] S. Müller. Bulk and surface ordering phenomena in binary metal alloys. *J. Phys.: Condens. Matter*, 15(34):R1429–R1500, 2003.

[70] S. Müller, M. Stöhr, and O. Wieckhorst. Structure and stability of binary alloy surfaces: Segregation, relaxation, and ordering from first-principles calculations. *Appl. Phys. A*, 82(3):415–419, Feb. 2006.

[71] F. D. Murnaghan. The Compressibility of Media under Extreme Pressures. *Proceedings of the National Academy of Sciences of the United States of America*, 30(9):244–247, 1944.

[72] S. Nosé. A unified formulation of the constant temperature molecular dynamics methods. *The Journal of Chemical Physics*, 81(1):511–519, 1984.

[73] J. F. Nye. *Physical Properties of Crystals*. Cleadon Press - Oxford, 1993.

[74] A. R. Oganov and C. W. Glass. Crystal structure prediction using ab initio evolutionary techniques: Principles and applications. *J. Chem. Phys.*, 124(24):244704, 2006.

[75] J. B. Pendry. Reliability factors for LEED calculations. *Journal of Physics C: Solid State Physics*, 13(5):937–944, 1980.

[76] J. P. Perdew, K. Burke, and M. Ernzerhof. Generalized Gradient Approximation Made Simple. *Phys. Rev. Lett.*, 77(18):3865–3868, Oct 1996.

[77] J. P. Perdew and A. Zunger. Self-interaction correction to density-functional approximations for many-electron systems. *Phys. Rev. B*, 23(10):5048–5079, May 1981.

[78] W. Pfeiler, editor. *Alloy Physics*. Wiley-VCH, 2007.

[79] K. Reuter and M. Scheffler. Composition, structure, and stability of $RuO_2(110)$ as a function of oxygen pressure. *Phys. Rev. B*, 65(3):035406, Dec 2001.

[80] N. Ridley. Densities of some indium solid solutions. *Journal of the Less Common Metals*, 8(5):354 – 357, 1965.

[81] P. A. Rikvold, K. Kaski, J. D. Gunton, and M. C. Yalabik. Finite-size scaling study of a lattice-gas model for oxygen chemisorbed on tungsten. *Phys. Rev. B*, 29(11):6285–6294, Jun 1984.

[82] A. M. Rodrguez, G. Bozzolo, and J. Ferrante. Multilayer relaxation and surface energies of fcc and bcc metals using equivalent crystal theory. *Surface Science*, 289(1-2):100–126, May 1993.

[83] P. Rous and J. Pendry. The theory of tensor LEED. *Surface Science*, 219(3):355 – 372, 1989.

[84] P. J. Rous. The tensor LEED approximation and surface crystallography by low-energy electron diffraction. *Progress in Surface Science*, 39(1):3 – 63, 1992.

[85] P. J. Rous, J. B. Pendry, D. K. Saldin, K. Heinz, K. Müller, and N. Bickel. Tensor LEED: A Technique for High-Speed Surface-Structure Determination. *Phys. Rev. Lett.*, 57(23):2951–2954, Dec 1986.

[86] J. M. Sanchez, F. Ducastelle, and D. Gratias. Generalized cluster description of multicomponent systems. *Physica A: Statistical and Theoretical Physics*, 128(1-2):334–350, Nov. 1984.

[87] Sensicam. PCO Computer Optics, Kelheim, Germany.

[88] M. H. F. Sluiter and Y. Kawazoe. Cluster expansion method for adsorption: Application to hydrogen chemisorption on graphene. *Phys. Rev. B*, 68(8):085410, Aug 2003.

[89] R. J. Smith, C. Hennessy, M. W. Kim, C. N. Whang, M. Worthington, and X. Mingde. High-energy ion-scattering studies of anisotropic surface-atom vibrations on W(110). *Phys. Rev. Lett.*, 58(7):702–705, Feb 1987.

[90] M. Stöhr. Das Segregationsverhalten der $\mathbf{Pt}_{25}\mathbf{Rh}_{75}$ (111)-Oberfläche. Master's thesis, Institut für Physik der Kondensierten Materie der Universität Erlangen-Nürnberg, Lehrstuhl für Festkörperphysik, 2005.

[91] M. Stöhr, R. Podloucky, M. Gabl, N. Memmel, and E. Bertel. Combined ab initio and LEED I/V study of submonolayer adsorption of In on W(110). *Phys. Rev. B*, 76(19):195449, 2007.

[92] G. Teeter, J. L. Erskine, F. Shi, and M. Van Hove. Surface roughness and LEED crystallography: Analysis of flat and vincinal W(110). *Phys. Rev. B*, 60(3):1975, 1999.

[93] L. Thomas. *Proc. Camb. Phil. Soc.*, 23:542–548, 1927.

[94] M. C. Tringides. Growth kinetics of O/W(110) at high coverage. *Phys. Rev. Lett.*, 65(11):1372–1375, Sep 1990.

[95] C. Uebing and R. Gomer. The diffusion of oxygen on W(110) The influence of the p(2 x 1) ordering. *Surf. Sci.*, 381(1):33–48, June 1997.

[96] J. van der Veen and M. Van Hove, editors. *The Structure of Surfaces II*. Springer, 1987.

[97] M. A. Van Hove and S. Y. Tong. Chemisorption Bond Length and Binding Location of Oxygen in a p(2x1) Overlayer on W(110) Using a Convergent, Perturbative, Low-Energy-Electron-Diffraction Calculation. *Phys. Rev. Lett.*, 35(16):1092–1095, Oct 1975.

[98] I. Vattulainen, J. Merikoski, T. Ala-Nissila, and S. C. Ying. Non-equilibrium surface diffusion in the O/W(110) system. *Surf. Sci.*, 366(2):L697–L702, Oct. 1996.

[99] I. Vattulainen, J. Merikoski, T. Ala-Nissila, and S. C. Ying. Adatom dynamics and diffusion in a model of O/W(110). *Phys. Rev. B*, 57(3):1896–1907, Jan 1998.

[100] I. Vattulainen, S. C. Ying, T. Ala-Nissila, and J. Merikoski. Memory effects and coverage dependence of surface diffusion in a model adsorption system. *Phys. Rev. B*, 59(11):7697–7707, Mar 1999.

[101] S. Vosko, L. Wilk, and M. Nusair. Accurate spin-dependent electron liquid correlation energies for local spin density calculations: a critical analysis. *Can. J. Phys.*, 58:1200, 1980.

[102] G.-C. Wang, T.-M. Lu, and M. G. Lagally. Phase transitions in the chemisorbed layer W(110) p (2 x 1) –O as a function of coverage. I. Experimental. *J. Chem. Phys.*, 69(1):479–489, 1978.

[103] E. D. Williams, S. L. Cunningham, and W. H. Weinberg. A determination of adatom–adatom interaction energies: Application to oxygen chemisorbed on the tungsten (110) surface. *J. Chem. Phys.*, 68(10):4688–4693, 1978.

[104] C. Wolverton and D. de Fontaine. Cluster expansions of alloy energetics in ternary intermetallics. *Phys. Rev. B*, 49(13):8627–8642, Apr 1994.

[105] C. Wolverton, V. Ozolins, and A. Zunger. Short-range-order types in binary alloys: a reflection of coherent phase stability. *Journal of Physics: Condensed Matter*, 12(12):2749–2768, 2000.

[106] P. K. Wu. PhD thesis, University of Wisconsin-Madison, 1987.

[107] P. K. Wu, M. C. Tringides, and M. G. Lagally. Ordering kinetics of a chemisorbed overlayer: O/W(110). *Phys. Rev. B*, 39(11):7595–7610, Apr 1989.

[108] W. Xu and J. B. Adams. Structure of seven W surfaces. *Surface Science*, 319(1-2):45–57, Nov. 1994.

[109] R. X. Ynzunza, R. Denecke, F. J. Palomares, J. Morais, E. D. Tober, Z. Wang, F. J. G. de Abajo, J. Liesegang, Z. Hussain, M. A. V. Hove, and C. Fadley. Kinetics and atomic structure of O adsorption on W(110)

from time- and state-resolved photoelectron spectroscopy and full-solid-angle photoelectron diffraction. *Surf. Sci.*, 459:69–92, 2000.

[110] R. X. Ynzunza, F. J. Palomares, E. D. Tober, Z. Wang, J. Morais, R. Denecke, H. Daimon, Y. Chen, Z. Hussain, M. A. Van Hove, and C. S. Fadley. Structure determination for saturated (1x1) oxygen on W(110) from full solid angle photoelectron diffraction with chemical-state resolution. *Surf. Sci.*, 442(1):27–35, Nov. 1999.

[111] M. A. Zaluska-Kotur, S. Krukowski, A. Lusakowski, and L. A. Turski. Domain growth in the interacting adsorbate: Nonsymmetric particle jump model. *Phys. Rev. B*, 75(11):115412, 2007.

[112] M. A. Załuska-Kotur, S. Krukowski, Z. Romanowski, and L. A. Turski. Twin spin model of surface phase transitions in O/W(110). *Phys. Rev. B*, 65(4):045404, Dec 2001.

[113] M. A. Załuska-Kotur, S. Krukowski, and L. A. Turski. Collective diffusion in a twin-spin model of $O/W(110)$. *Phys. Rev. B*, 67(15):155406, Apr 2003.

[114] M. A. Zaluska-Kotur, A. Lusakowski, S. Krukowski, and L. A. Turski. Collective diffusion of O/W(1 1 0) at high coverages: Monte Carlo simulations. *Surf. Sci.*, 566-568(Part 1):210–215, Sept. 2004.

[115] Y. Zhang, V. Blum, and K. Reuter. Accuracy of first-principles lateral interactions: Oxygen at Pd(100). *Phys. Rev. B*, 75(23):235406, 2007.